HYBRID OPTICAL-MAGNETIC TRAPS FOR STUDIES OF 2D QUANTUM TURBULENCE IN BOSE-EINSTEIN CONDENSATES

by

Jessica Ann Myers

A Dissertation Submitted to the Faculty of the

COLLEGE OF OPTICAL SCIENCES

In Partial Fulfillment of the Requirements
For the Degree of

DOCTOR OF PHILOSOPHY

In the Graduate College

THE UNIVERSITY OF ARIZONA

2017

THE UNIVERSITY OF ARIZONA
GRADUATE COLLEGE

As members of the Dissertation Committee, we certify that we have read the dissertation prepared by **Jessica Ann Myers** entitled **Hybrid Optical-Magnetic Traps for Studies of 2D Quantum Turbulence in Bose-Einstein Condensates** and recommend that it be accepted as fulfilling the dissertation requirement for the Degree of Doctor of Philosophy.

Date: 12 July 2017

Brian P. Anderson

Date: 12 July 2017

Ewan M. Wright

Date: 12 July 2017

R. Jason Jones

Date: 12 July 2017

Final approval and acceptance of this dissertation is contingent upon the candidate's submission of the final copies of the dissertation to the Graduate College.
I hereby certify that I have read this dissertation prepared under my direction and recommend that it be accepted as fulfilling the dissertation requirement.

Date: 12 July 2017

Dissertation Director: Brian P. Anderson

STATEMENT BY AUTHOR

This dissertation has been submitted in partial fulfillment of requirements for an advanced degree at the University of Arizona and is deposited in the University Library to be made available to borrowers under rules of the Library.

Brief quotations from this dissertation are allowable without special permission, provided that accurate acknowledgment of source is made. Requests for permission for extended quotation from or reproduction of this manuscript in whole or in part may be granted by the head of the major department or the Dean of the Graduate College when in his or her judgment the proposed use of the material is in the interests of scholarship. In all other instances, however, permission must be obtained from the author.

SIGNED: Jessica Ann Myers

ACKNOWLEDGEMENTS

First, I would like to thank my PhD advisor, Brian Anderson, for his guidance and input to my research over the past five years. Thank you for helping me pursue my passion for teaching while in graduate school. I would also like to thank Ewan Wright and Jason Jones for serving on my dissertation committee as well as providing guidance and feedback on my research.

I am extremely thankful for all my labmates, past and present, that have provided friendship and support and shared their knowledge of BEC physics with me. Thanks to Zach Newman for teaching me most of what I know about the lab, being a great mentor, and teaching me proper electronics and machining. Thanks to Andrew Schaffer for taking over the lab and helping me to collect data for this dissertation. Thanks to Sam Nerenberg, Joe Lowney, and Kali Wilson for providing a welcome break from the lab and always being willing to bounce ideas back and forth.

I am grateful to the National Science Foundation for a Graduate Research Fellowship that funded my last three years of graduate school and to the donors of the Willis E. Lamb Jr. Endowed Scholarship for making my first years at the University of Arizona possible.

Thanks to my friends that have helped me stay sane throughout graduate school. I am thankful for Kelsey Miller and Clarissa Wylde for our late night study sessions. I am so thankful for my church family at the Vineyard Christian Community. Thank you to all the couples in our Bible Study for your love, support, and prayers throughout this process.

Thanks to my wonderful family that has loved and supported me throughout this journey. I am thankful for my parents, Chris and Julie Doehrmann, for always challenging me to pursue excellence in all that I do and for sparking my initial interest in math and science. Thanks to my siblings for their friendship and encouragement.

I am so thankful for my loving and supportive husband, Phillip Myers, without whom I wouldn't have finished graduate school or this dissertation. Thank you for continually encouraging me to keep going even when it was hard, doing all the cooking and cleaning for the last couple of months to let me focus on writing and for your unceasing love.

All of this would not have been possible except by the grace of God. To Him be the glory.

DEDICATION

To my loving husband

TABLE OF CONTENTS

LIST OF FIGURES

LIST OF TABLES

ABSTRACT

Turbulence appears in most natural and man-made flows. However, the analysis of turbulence is particularly difficult. Links between microscopic fluid dynamics and statistical signatures of turbulence appear unobtainable from the postulates of fluid dynamics making turbulence one of the most important unsolved theoretical problems in physics. Two-dimensional quantum turbulence (2DQT), an emerging field of study, involves turbulence in two-dimensional (2D) flows in superfluids, such as Bose-Einstein condensates (BECs). In 2D superfluids, a turbulent state can be characterized by a disordered distribution of numerous vortex cores. The question of how to effectively and efficiently generate turbulent states in superfluids is a fundamental question in the field of quantum turbulence. Therefore, experimental studies of vortex nucleation and the onset of turbulence in a superfluid are important for achieving a deeper understanding of the overall problem of turbulence.

My PhD dissertation involves the study of vortex nucleation and the onset of turbulence in quasi-2D BECs. First, I discuss experimental apparatus advancements that now enable BECs to be created in a hybrid optical-magnetic trap, an atom trapping configuration conducive to 2DQT experiments. Next, I discuss the design and construction of a quantum vortex microscope and initial vortex detection tests. Finally, I present the first experiments aimed at studying 2DQT carried out in the updated apparatus. Thermal counterflow in superfluid helium, in which the normal and superfluid components flow in opposite directions, is known to create turbulence in the superfluid. However, this phenomenon has not been simulated or studied in dilute-gas BECs as a possible vortex nucleation method. In this dissertation, I present preliminary data from the first experiments aimed at understanding thermal counterflow turbulence in dilute-gas BECs.

CHAPTER 1

Introduction

1.1 The Problem of Turbulence

Turbulence is ubiquitous throughout nature: it appears in wakes of ships, smoke rising from a cigarette, and boiling water. Phenomenologically, turbulence can be characterized as a disordered flow with many vortices decaying to ever smaller ones, enabling rapid fluid mixing [1]. However, the analysis of turbulence is particularly difficult: while the energy density in turbulent flows can be estimated from dimensional analysis [2], measured [3], and simulated with Navier-Stokes equations [1], the links between microscopic fluid dynamics and statistical signatures of turbulence appear unobtainable from the postulates of fluid dynamics. Therefore turbulence is one of the most important theoretical problems in physics that remains unsolved [1].

Turbulence in two-dimensional (2D) flows is present throughout nature in soap films [4], atmospheric strata [5] and may be responsible for the continued existence of Jupiter's Great Red Spot [6, 7]. In 3D turbulence, a direct energy cascasde exists where energy flows from large to small length scales. However, due to the suppression of vortex stretching in 2D flows, small-length-scale forcing of energy and vorticity generates large-scale flows resulting in an *inverse energy cascade* [8, 5] that contrasts the direct energy cascade in 3D turbulence.

Two-dimensional quantum turbulence (2DQT), which is of particular interest to our research group, involves the study of 2D turbulence in quantum fluids, such as superfluid helium and dilute-gas atomic Bose-Einstein condensates (BECs). The developing field of 2DQT offers new avenues for understanding aspects of 2D turbulence, specifically crossovers between quantum and classical fluid dynamics and the universality of 2D turbulence. Additionally, a deeper understanding of quantized vortices, quantum turbulence [9] and superfluidity may be gained through studies in this field. We chose ^{87}Rb BECs as the quantum fluid in which 2DQT experiments are conducted in our lab for the following reasons: First, the lasers and magnetic fields needed for cooling and trapping provide flexible trapping configurations and control of the effective dimensionality of the system. 2D flows are easily achieved by the use of a tightly focused laser beam to confine a BEC to a plane, resulting in quasi-2D and oblate BECs. And secondly, the Gross-Pitaevskii equation (GPE), a nonlinear

Schrodinger equation for the BEC wavefunction, can be used to model and simulate the dynamics of the fluid, providing a theoretical framework for experiments.

Feynman characterized quantum turbulence in a superfluid as a tangle of quantized vortex lines that have well-defined core structure and quantized circulation [10]. In 2D superfluids, a turbulent state can be characterized by a disordered distribution of numerous vortex cores. The question of how to effectively and efficiently generate turbulent states in superfluids is a fundamental question in the field of quantum turbulence [11]. Therefore, studies of vortex nucleation and the onset of turbulence in a superfluid are important experimental approaches to achieving a deeper understanding of the overall problem of turbulence. Our lab has previously studied methods for nucleating vortices and generating 2DQT states in oblate BECs. Many of these methods are described in Reference [12]. Section 1.2 gives a brief overview of these vortex nucleation methods and proposes a possible new vortex nucleation method that is investigated in this dissertation.

1.2 Overview of Vortex Nucleation Methods in BECs

Vortices are easily created in oblate BECs by perturbing the trapping potential. For oblate BECs created in a combined optical-magnetic trap using a TOP trap and sheet trapping laser, this can be done by modifying the magnetic trapping potential. Weak symmetric modulation of the amplitude of the TOP trap results in disordered distributions of vortex cores. Vortices are created near the boundary and travel towards the center of the BEC. In the same way, a disordered distribution of vortices is created in a highly oblate annular trap by weakly modulating the trapping potential, as seen in Figure 1.1. Rotation of an elliptical magnetic trapping potential was found to be another vortex nucleation mechanism [12].

In addition to modulating the magnetic field, the trapping potential can be perturbed through the use of a blue-detuned laser that acts as a repulsive barrier. A short pulse of the blue-detuned laser beam focused axially through the condensate creates shock waves and consequently, vortices enter at the boundary of the condensate as the shock waves propagate. Alternatively, intensity modulation of a blue-detuned laser beam induces large numbers of vortex cores as well as large-scale breathing modes in the radial dimension in the BEC. Images of the vortex distributions and breathing modes of the BEC are shown in Figure 1.2.

One vortex nucleation method that creates a well-defined initial distribution of vortices is the swiping of a blue-detuned laser beam used as a repulsive optical barrier through a BEC. By forcing superfluid flow around the Gaussian barrier above some critical velocity, a vortex dipole, defined as a pair of vortices with opposite

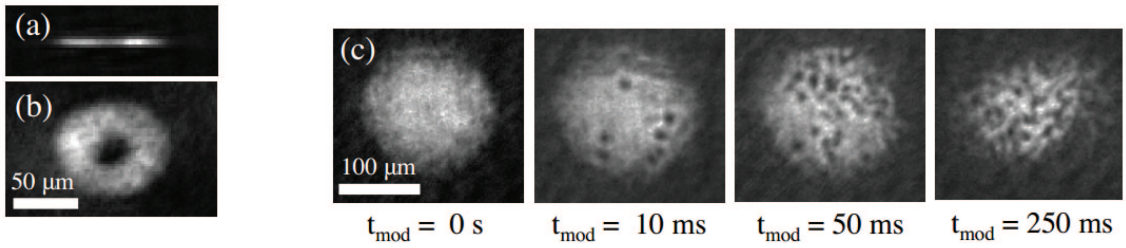

Figure 1.1: Modulating the radial trapping frequency for a BEC in an annular trapping geometry. (a) side view of an annular BEC imaged using in situ phase contrast imaging. (b) top-down view of an annular BEC imaged using absorption imaging immediately after turning off the trapping potential. For these two images, the blue-detuned beam provides a barrier of height well above the chemical potential, confining the atoms to an annular trap. The annular trap used for the sequence of images in (c) had a narrower, weaker central barrier. (c) images taken at increasing modulation times with no hold after modulation. The first image shows the expanded BEC for $t_{mod} = 0$ s to show that the hole created by the blue-detuned beam has completely filled between beam ramp down and imaging. For the annular trapping geometry vortices appear after much shorter modulation times than for the harmonic trapping case. Image and caption taken from Reference [12].

circulations, is formed in the wake of the optical barrier. [13] This vortex nucleation method is shown in Figure 1.3. Some interesting questions motivated by this experiment follow: *What would happen if the repulsive optical barrier was replaced with some other barrier, a high energy atom for example? What if a cloud of thermal atoms was used as the repulsive barrier? Would vortices be created?*

1.3 Thermal Counterflow in Superfluid Helium

In addition to studies of generating tubulent states in condensates, methods for inducing turbulence in superfluid helium have also been studied. Thermal counterflow is one such method. Superfluid helium is composed of a normal fluid component, which carries thermal energy and entropy, and a non-viscous superfluid component [14]. When heat is applied to a closed channel containing superfluid helium, the normal component of the fluid carries heat away from the heater and the superfluid moves towards heat source to eliminate net mass flow. Therefore the superfluid and normal components flow in opposite directions, referred to as thermal counterflow. Above a critical value of heat flux, which corresponds to a relative velocity between

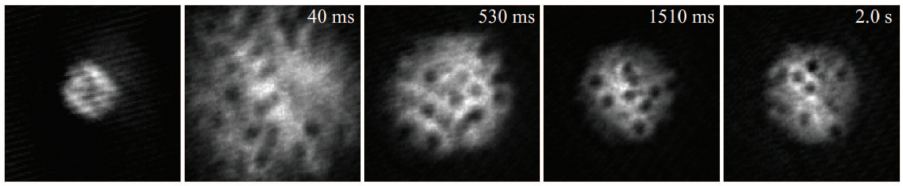

Figure 1.2: 250-μm-square absorption images acquired after the hold times indicated. The first image is an in situ image of the BEC in the harmonic trap with the blue-detuned beam partially penetrating the condensate; note that the optical potential strength is well below the BEC chemical potential. Image and caption taken from Reference [12].

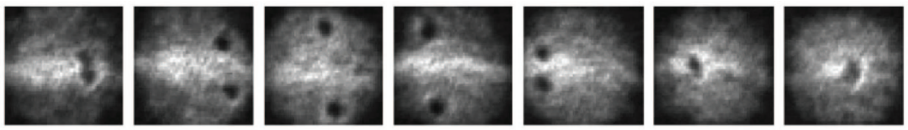

Figure 1.3: Images of oblate BECs in expansion showing dynamics of vortex dipole created by swiping repulsive optical barrier through condensate. Image taken from Reference [13].

the two fluid components, the superfluid becomes turbulent which is evidenced in a tangle of quantized vortex lines [15, 16]. To date, superfluid thermal counterflow turbulence has not been studied in dilute-gas BECs, provoking the following questions: *If a high energy thermal atom collides with a stationary condensate, resulting in a relative counterflow between the thermal and condensate atoms, would vortices be created? Is the onset of turbulence due to thermal counterflow unique to superfluid helium or will thermal counterflow create turbulence in dilute-gas BECs?*

1.4 Format of this Dissertation

Work presented in this dissertation, which involves construction of a BEC apparatus and the first 2DQT experiments done in the apparatus, is motivated by the research questions proposed in Sections 1.2 and 1.3. In order to investigate thermal counterflow and the nucleation of vortices in dilute gas BECs, construction of a BEC apparatus and microscope was necessary. Chapter 2 gives an overview of the first phase of apparatus construction, which is thoroughly described in Zach Newman's PhD dissertation [17], as well as debugging techniques and details useful for the operation of the apparatus. Chapter 3 describes the second phase of apparatus

construction, done in conjunction with Andrew Schaffer, which focuses on implementation of trapping lasers, evaporative cooling techniques, and the BEC creation process. Design, construction and implementation of the BEC microscope, including vortex imaging tests, is describe in Chapter 4. And finally, the thermal counterflow experimental procedure, data and conclusions are presented in Chapter 5.

CHAPTER 2

Construction of BEC Apparatus - Phase 1

A significant portion of my graduate research involved construction of a BEC apparatus for studies of 2D Quantum Turbulence (2DQT). Working with Zach Newman, the first phase of apparatus construction included setup and implementation of laser locking, laser cooling and trapping and magnetic trapping and transfer techniques used to create the first BECs in our lab. For a detailed description of the apparatus construction and a brief overview of the physics behind the techniques used in our lab to create BECs, refer to Zach Newman's dissertation [17]. This chapter focuses on additional information useful for operation of the apparatus, changes that have been made since Newman's dissertation was written, common problems experienced in the lab and their solutions, and debugging techniques related to the processes involved in the creation of BECs. Section 2.1 provides a brief explanation of the frequency stabilization, laser cooling and trapping, and magnetic trapping and transfer processes used in our lab. Section 2.2 gives a more detailed description of diode lasers and frequency stabilization. Section 2.3 discusses the Tapered Amplifiers used to amplify laser-locked diode lasers as well as the daily operation of the amplifiers and problems that we have encountered with them. Section 2.4 discusses the Rb dispensers used in the apparatus, daily operation and MOT loading rates. Section 2.5 explains the electronics used to control high currents through the transfer coils, and finally, Section 2.6 discusses ground loop problems in the apparatus and how they have been eliminated. In our group, we have found that previous dissertations are a useful resource for helping future students understand the operation of the apparatus and facilitate debugging any problems that occur. With that in mind, this chapter has been written with future students as the target audience and gives detailed information about the different components of the apparatus, their problems and debugging techniques.

2.1 Overview of Apparatus

A dilute-gas BEC is a collection of bosonic atoms that all occupy the same quantum state. When a dilute atomic gas is cooled below a density-dependent critical temperature T_C, a temperature-dependent fraction of atoms undergoes a quantum phase

transition to a BEC. Conceptually, the transition to BEC occurs when the temperature of the atomic gas is low enough that the mean spatial extent of the atoms given by the thermal deBroglie wavelength, λ_{dB}, is comparable to the inter-particle separation. Mathematically, this idea can be expressed by the phase space density ρ, which is defined as the number of particles contained within a volume equal to the cube of the thermal deBroglie wavelength [18]

$$\rho = n{\lambda_{dB}}^3 \tag{2.1}$$

where n is the number density and the deBroglie wavelength is given by the following equation:

$$\lambda_{dB} = \sqrt{\frac{2\pi\hbar^2}{mk_BT}}. \tag{2.2}$$

The quantum nature of a dilute-gas is relevant when $\rho \sim 1$; therefore, high densities and low temperatures are needed to reach condensation. Typical atomic densities in dilute-gas BECs are six orders of magnitude less than the density of air at room temperature. Therefore, BEC creation and experiments occur in a vacuum chamber. Our vacuum chamber, described in Section 2.1.1, is pumped down to pressures less than 10^{-10} Torr in the BEC cell, or region where BECs are created. Traditional laser cooling and trapping techniques, described in Sections 2.1.2 - 2.1.4, are used to provide the initial atom cooling stage. Atoms are then trapped in a purely magnetic trap and magnetically transferred to the BEC cell, as discussed in Sections 2.1.5 - 2.1.7, where the atoms are further cooled to condensation.

2.1.1 Vacuum Chamber

The vacuum chamber is composed of a 2D Magneto-Optical Trap (MOT) cell, a differential pumping tube, an ultra-high vacuum pump, and a 3D MOT/BEC cell, as shown in Figure 2.1. The 2D MOT cell has two arms attached to the main part of the cell that contain three Rb dispensers in one arm and three K dispensers in the other. When current runs through a filament connected to the Rb dispensers, heat is applied to the dispensers releasing, Rb into the vacuum chamber. Two pinholes and a differential pumping tube separate the 2D and 3D MOT cells in the vacuum chamber. This allows for high partial pressures of Rb in the 2D MOT cell, which are needed for the creation of 2D MOTs, while maintaining low enough pressures, below 10^{-10} Torr, in the 3D MOT/BEC cell for the creation of BECs. For more information regarding the vacuum chamber, see reference [17].

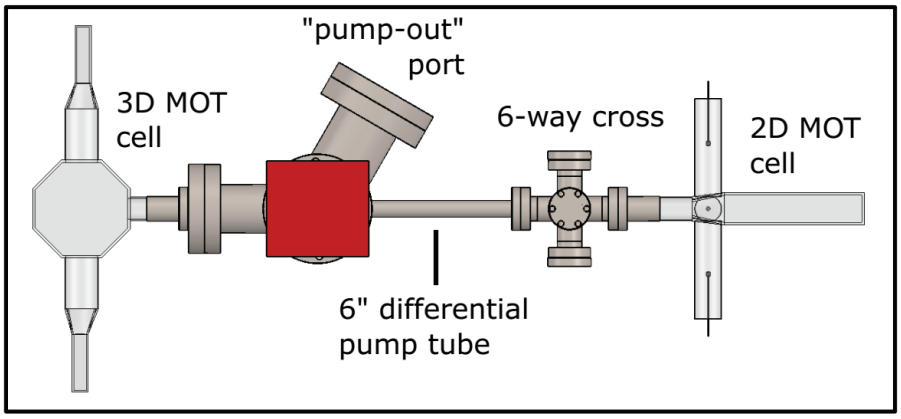

Figure 2.1: Overhead view of the vacuum chamber showing its four main components. Figure taken from reference [17].

2.1.2 2D MOT

The first cooling process in the apparatus involves laser cooling and trapping in 2 dimensions to create a cold beam source used to load our 3D MOT. Traditionally, MOTs use three sets of orthogonal, counter-propagating, and instersecting laser beams along with a spherical quadrupole magnetic field centered at the intersection of the laser beams. This creates a position-dependent radiation force and results in cooling and trapping of the atom cloud in three dimensions. For more information regarding MOT physics, see references [19, 20, 21].

The 2D MOT differs from the traditional 3D MOT described above in that confinement and laser cooling only occurs in two dimensions, allowing atoms to travel freely in the third dimension. Two sets of orthogonal, counter-propagating cylindrical beams that are circularly polarized and slightly diverging are used to provide a two-dimensional radiation force on the atoms. The 2D MOT beams are comprised of light -2Γ detuned from the ^{87}Rb $|5\ ^2S_{1/2}, F = 2\rangle \rightarrow |5\ ^2P_{3/2}, F' = 3\rangle$ transition, where $\Gamma = 2\pi\times6$ MHz is the natural linewidth, as the cooling beams, and light on resonance with the $|5\ ^2S_{1/2}, F = 1\rangle \rightarrow |5\ ^2P_{3/2}, F' = 2\rangle$ transition as the repump beams. Both cooling and repump transitions are shown in Figure 2.7. Repump light is necessary to pump atoms out of the $|F = 1\rangle$ ground state that is inaccessible by the cooling beams. As seen in Figure 2.2, the 2D MOT beams intersect in the center of the cell and create a cylinder-shaped overlapping region.

Two sets of rectangular magnetic field coils oriented in an anti-helmholtz configuration are used to create a magnetic field that has a gradient in two directions and is uniform in the direction in which there is no laser cooling. Figures 2.2 and

3.4 show the placement of the 2D MOT coils with respect to the 2D MOT cell and the 2D MOT beams. This 2D gradient in conjunction with two sets of intersecting cylindrical MOT beams creates a 2D MOT, where atoms are cooled and trapped in two dimensions, resulting in a pencil shaped atom cloud. The free direction of the 2D MOT, or direction in which atoms experience no confinement or cooling, is chosen to be along to the axis of the vacuum chamber. A 3 mm diameter pinhole separates the 2D MOT cell from the rest of the vacuum chamber, filtering out atoms with a significant velocity component in the horizontal or vertical directions. This results in a fairly collimated cold beam source for 3D MOT loading.

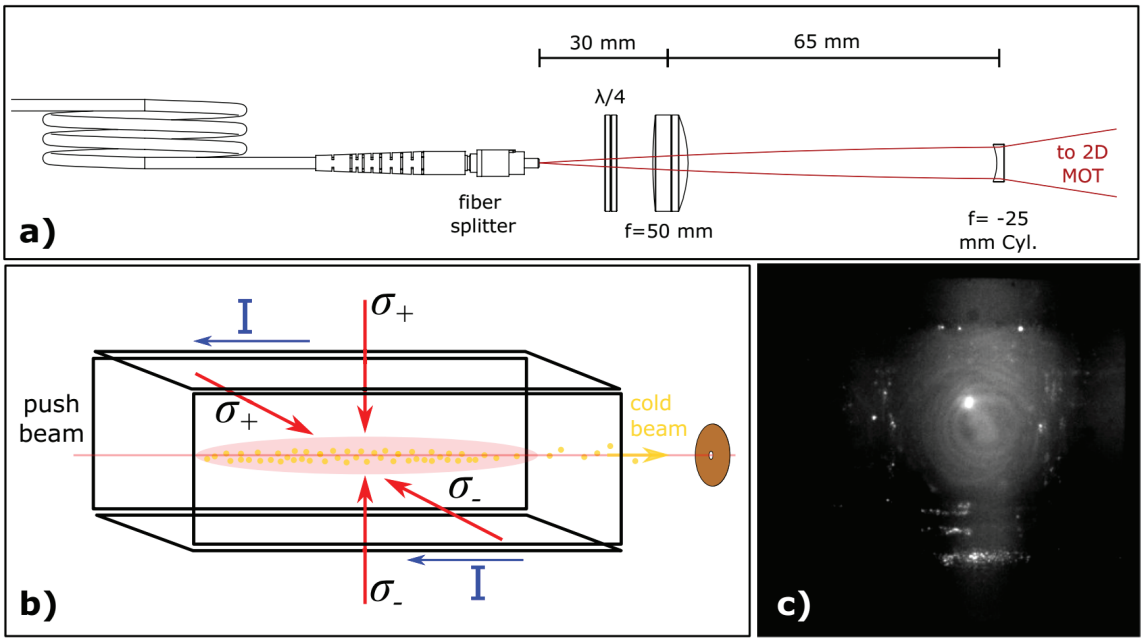

Figure 2.2: a) Optics for shaping 2D MOT beams. The 2D MOT beams come directly out of the 2x4 fiber splitter and expand to 1x4 in, circularly polarized beams at the center of the 2D MOT chamber. b) Diagram of a typical 2D MOT setup with a push beam propagating along the atom beam axis. The 2D MOT beams are shown as red arrows and the elongated quadrupole coils are represented by black rectangles. The atoms are located in the region of intersection of the 2D MOT beams, represented by the light red oval, and propagate towards the pinhole located at the end of the 2D MOT cell. c) An image of the 2D MOT fluorescence looking down the axis of the vacuum chamber. The 2D MOT is the bright dot in the center of the image. Fluorescence from the MOT beams surrounds the 2D MOT. Figure taken from reference [17].

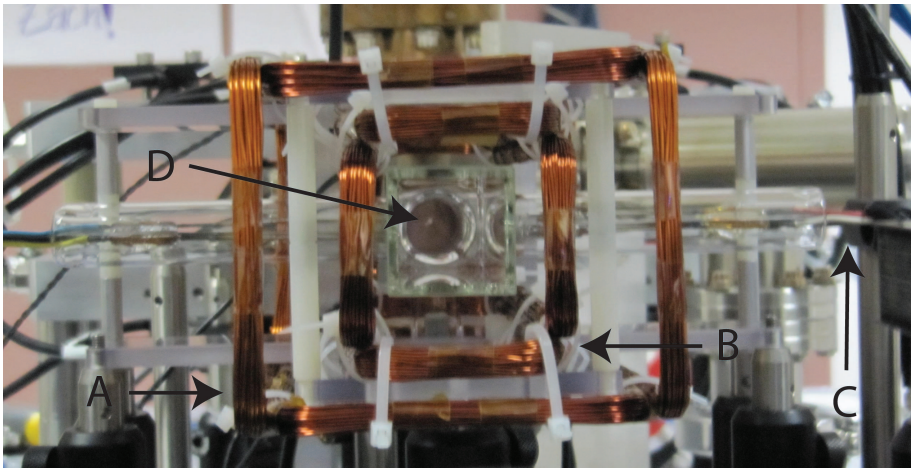

Figure 2.3: A) Bias coils for 2D MOT. Current flows the same direction through each coil in the pair creating a bias field that moves the axis of the elongated quadrupole field minimum. B) Rectangular 2D MOT coils oriented to give an elongated quadrupole field with 0 G field along the chamber axis. C) Leads to the Rb dispensers. D) Main 2D MOT cell.

2.1.3 3D MOT Loading

In order for the cold atom beam to effectively load the 3D MOT, it must be aligned along the vacuum chamber axis. Two sets of rectangular magnetic field coils in a bias field configuration are used to align the 2D MOT to the optimum position for 3D MOT loading. A collimated beam on resonance with the cooling transition, referred to in this dissertation as the push beam, is also aligned down the axis of the vacuum chamber, overlapping atoms in the 2D MOT. The push beam redirects atoms that are moving away from the 3D MOT cell back down the vacuum chamber towards the 3D MOT for optimum loading. Usually $\sim$600 μW of power in the push beam is sufficient.

2.1.4 3D MOT

In a secondary stage of cooling, atoms are further cooled down to tens of μK in the traditional 3D MOT configuration discussed in Section 2.1.2. The main difference between our 3D MOT setup and traditional MOTs is that we using diverging instead of collimated MOT beams. The use of diverging MOT beams eliminates instabilities due to standing waves and decreases the MOT number dependence on alignment of the MOT beams. Typically, we tweak MOT beam alignment only once or twice a

year. About 5×10^9 atoms are cooled and trapped in three dimensions in our 3D MOT, resulting in a cold, fluorescing ball of Rb atoms as seen in Figure 2.4. The atom flux from the push beam is so great that it creates a hole in the atoms trapped in the 3D MOT. Therefore, for optimum 3D MOT loading, the push beam is aligned to the side of the a 3D MOT instead of to the center. This results in a slightly aspherical atom cloud as seen in Figure 2.4.

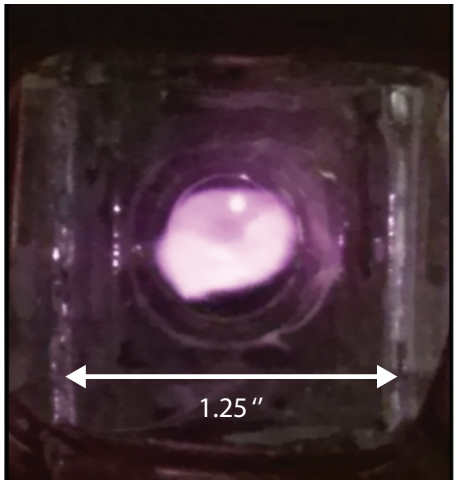

Figure 2.4: Image of 3D MOT fluorescence in 3D MOT cell. The bright dot seen in the upper edge of the MOT is the push beam. Image taken from reference [17].

2.1.5 CMOT and Pumping into F = 1

After this second stage of laser cooling and trapping, atoms are further cooled and compressed in a CMOT in preparation for transfer to a purely magnetic trap. During this CMOT stage, the detuning of the cooling beams is linearly ramped from -3Γ to -7Γ while power in the cooling beams is reduced from 26 mW/beam to 2.6 mW/beam. At the same time the repump power is snapped down to 7 μW/beam. The combination of increasing the detuning, decreasing the power in the cooling beams and significantly decreasing the repump power results in a colder and denser cloud, which is more efficiently transferred to the purely magnetic trap. Traditionally, the magnetic field gradient is also increased during the CMOT stage to further compress the cloud. In our apparatus, however, a magnetic field gradient that linearly decreases from 11 G/cm to 5 G/cm is optimum for maxiumum transfer efficiency to the purely magnetic trap. Out of all the parameters that change during the CMOT stage, the temperature of the atoms and transfer efficiency to the magnetic trap are

most sensitive to the repump power. After the CMOT stage, atoms are pumped into the $|F = 1\rangle$ ground state by shutting off the repump light and leaving the cooling light on for 0.5 ms. For more details on these specific time steps in the timing sequence, refer to Appendix A.

2.1.6 Magnetic Trapping

The interaction between magnetic dipole moments of neutral atoms and external magnetic fields results in the following potential energy

$$U_B = -\vec{\mu} \cdot \vec{B} \tag{2.3}$$

where $\vec{\mu}$ is the atom's magnetic dipole moment and $\vec{B}$ is the external magnetic field. In the case where the energy shift due to the external magnetic field is small relative to the ground state splitting, the potential energy can be written as

$$U = \mu_B m_F g_F |B| \tag{2.4}$$

where μ_B is the Bohr magneton, m_F is angular momentum magnetic quantum number and g_F is the Lande g-factor. The F = 1 ground state has 3 hyperfine splittings: $m_F = 1,\ 0,\ -1$, and the Langde g-factor is $g_F = 1/2$. The $|F = 1, m_F = -1\rangle$ state is a weak field seeking state because $U_B \geq 0$. Therefore for ^{87}Rb atoms in the $|F = 1, m_F = -1\rangle$ state, a magnetic field with a local minimum acts as a trap. We use a spherical quadrupole field created from a pair of coils in an anti-helmholtz configuration to provide the magnetic trap. After pumping atoms into $|F = 1\rangle$ and turning off all light and magnetic fields for 1 ms, the MOT coils are snapped to the catch value of 50 G/cm. Approximately one third of the atoms, most $|F = 1, m_F = -1\rangle$ atoms, are trapped in the purely magnetic trap.

2.1.7 Magnetic Transfer

Atoms are transferred from the 3D MOT cell to the BEC cell by smoothly translating the trap minimum by ramping on and off currents in overlapping pairs of magnetic field coils. In order to minimize heating of the atom coud during transfer, current ramps were calculated to maintain a constant gradient in the direction of transfer and minimize vertical magnetic field gradient fluctuations throughout the transfer. Following these current ramps, discussed in reference [17], the three sets of transfer coils (see Figure 2.5) are ramped on and off, transferring about 40% of the atoms in the initial magnetic trap to the BEC cell in 1 second. During transfer, the atoms

travel through a constriction where the vacuum chamber height tapers down to 5 mm at the location of the BEC cell. The atom cloud in the magnetic trap is initially larger than the height of the constriction, resulting in transfer of only 40% of the magnetically trapped atoms. This atom loss during transfer is beneficial for two reasons. 1) A greater percentage of highly energetic atoms than low energy atoms are lost during transfer because the more highly energetic atoms spend more time near the edge of the cloud, interacting with the cell walls. We suspect that the loss of the highly energetic atoms during transfer acts as an evaporative cooling process, resulting in a lower average temperature of the magnetically trapped atoms. 2) The number of atoms in the BEC is not highly sensitive to inital MOT number due to this loss. At the end of transfer, the transfer coils are linearly ramped down to 0 A as the BEC quadrupole coils, the main coils used for trapping atoms in the BEC cell, are ramped up to a gradient of 250 G/cm. The atoms then undergo two evaporative cooling stages, which are discussed in the Chapter 3, until condensation is reached.

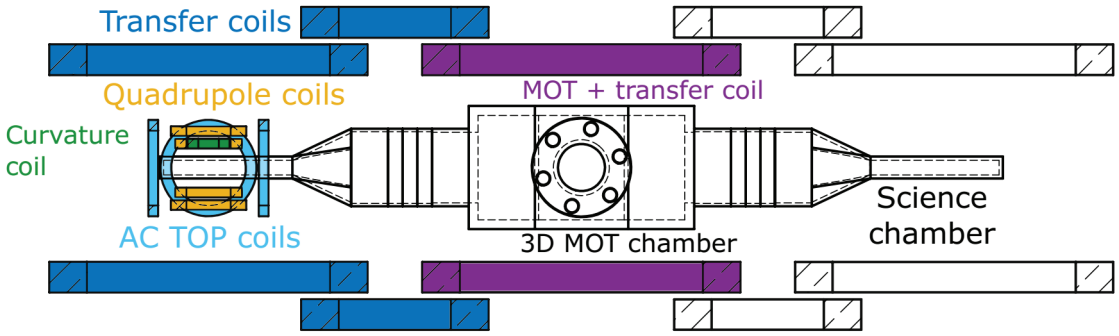

Figure 2.5: Diagram of the magnetic field coil system located around the 3D MOT/BEC cell. Purple and dark blue coils comprise the magnetic transfer system. The center coil pair serves both as transfer coils and MOT coils. The smaller yellow coils around the science cell are the magnetic field coils that make up the quadrupole trap for the BEC. The AC TOP bias coils (light blue) are simply used as bias fields to move the minimum of the quadrupole field. Figure taken from reference [17].

2.2 Diode Lasers and Frequency Stabilization

As discussed in Section 2.1.2, the MOT beams require light tuned to both the cooling $|F = 2 \rightarrow F' = 3\rangle$ and repump $|F = 1 \rightarrow F' = 2\rangle$ transitions. To provide cooling and repump light for both the 2D and 3D MOTs, four single-mode 780-nm diode lasers

that are frequency stabilized to ^{87}Rb transitions are used in conjunction with Tapered Amplifiers, discussed in Section 2.3. The master cooling and repump diode lasers have external cavities and are locked to ^{87}Rb transitions using saturated absorption and polarization spectroscopy techniques. The slave lasers have no external cavity and are injection locked to the frequency stabilized master lasers. See Section 2.2.3 for a more detailed description of how injection locking is used in the apparatus. In this way, 4 lasers are locked to atomic transitions while only two sets of electronics and optics are required for laser locking setups. For more information regarding diode lasers used in this apparatus, see reference [17].

2.2.1 Repump Lasers

A couple mW of the repump master light is picked off from the main path and sent to a saturated absorption spectroscopy setup for frequency stabilization to the $|F = 1\rangle \rightarrow |F' = 1 - 2\rangle$ crossover. The saturation absorption spectroscopy setup is shown in Figure 2.6. All active frequency stabilization requires a dispersive signal with a zero-crossing at the locking point. Frequency modulation and the lock-in amplifier detection method are used to electronicaly differentiate the saturated absorption spectroscopy signal, resulting in a dispersive locking signal with a zero-crossing at the atomic transition. We use the MOGLabs DLC252 Diode Laser Driver to both drive and lock the repump master laser. Along with a current source, the MOGLabs driver has a temperature controller, feedback servos, modulator driver, lock-in amplifier, piezo driver, and sweep ramp generator included. Locking the repump master laser requires no external lock box and is entirely done through the MOGLabs controller.

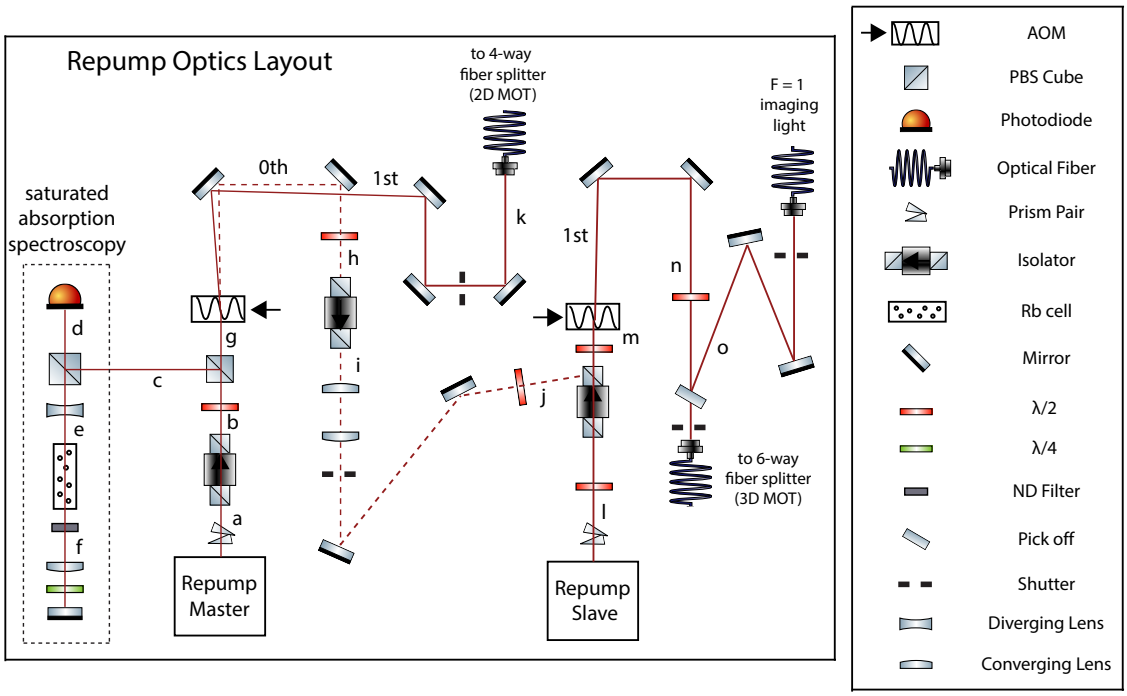

Figure 2.6: Optical layout for repump master and slave lasers. The repump master laser is frequency stabilized to a ^{87}Rb transition using saturated absorption spectroscopy signal that is integrated into an electronic feedback loop. The slave laser is injection locked to the master laser by aligning a small amount of master laser light into the slave laser diode cavity. The following powers can be used as a reference for alignment and trouble-shooting purposes: (a) 58.3 mW, (b) 46.7 mW, (c) 1.88 mW, (d) 0.204 mW, (e) 1.57 mW, (f) 0.78 mW, (g) 40.3 mW, (h) 6.47 mW, (i) 5.45 mW, (j) 4.95 mW, (k) 29.9 mW, (l) 68.5 mW, (m) 63.4 mW, (n) 47.9 mW, and (o) 4 mW.

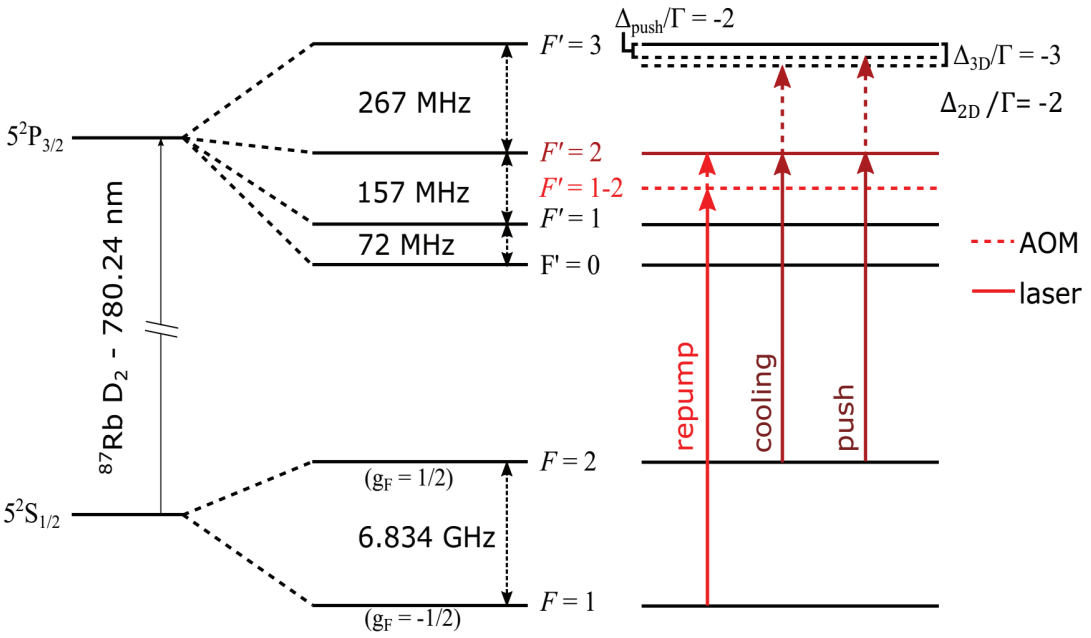

Figure 2.7: Diagram of frequencies used for MOT cooling and repump beams and the push beam. The repump lasers are locked to the $|F = 1\rangle \rightarrow |F' = 1 - 2\rangle$ crossover and frequency shifted by an AOM to be on resonance with the $|F = 1\rangle \rightarrow |F' = 2\rangle$ transition. The cooling lasers are locked to the $|F = 2\rangle \rightarrow |F' = 2\rangle$ transition and frequency shifted to -3Γ and -2Γ detuned from the $|F = 2\rangle \rightarrow |F' = 3\rangle$ transition for the 3D and 2D cooling beams respectively. Image taken from reference [17]

The majority of the repump master light passes through an 80 MHz AOM set to 77 MHz, which shifts the frequency of the 1^{st} order light so that it is on resonance with the $|F = 1\rangle \rightarrow |F' = 2\rangle$ transition. By using an AOM to shift the frequency instead of locking directly to the repump transition, the fast turn on/off properties of the AOM are utilized throughout the experiment to turn on and off the repump master light on the order of hundreds of nanoseconds. In our lab, single-pass AOMs are used to both shift the light to the desired frequency and shut off the light quickly. A physical shutter is also used in conjunction with a single-pass AOM to ensure that all the light is blocked by the shutter when needed throughout the BEC creation process. The 1^{st} order from the AOM is coupled into a 2 x 4 Evanescent Optics fiber splitter, providing repump light for the 2D MOT beams.

The 0^{th} order light, unshifted in frequency by the AOM, is aligned back into the repump slave diode laser, as shown in Figure 2.6. This light is used to injection lock the repump slave laser, causing the slave laser to lase at the $|F = 1\rangle \rightarrow |F' = 1 - 2\rangle$

crossover frequency as well. The output of the slave laser is also sent through a single–pass AOM at ∼78 MHz. The 1^{st} order beam, shifted on resonance with the repump transition is coupled into a 2 x 6 Evanescent Optics fiber splitter, providing repump light for the 3D MOT beams. A couple mW of the 1^{st} order beam is picked off and coupled into a separate fiber for BEC imaging.

2.2.1.1 MOGLabs Laser Diode Controller

In the past, we have struggled to operate our diode lasers in a mode-hop free range around the repump transition and successfully lock to transitions around the repump transition. Use of the MOGLabs controller for locking has increased the locking signal size and has allowed us to successfully lock the repump master laser to the $|F = 1\rangle \rightarrow |F' = 1 - 2\rangle$ crossover. However, if the laser does not stay locked throughout the day, use the following procedure to re-optimize the locking signal. After the above locking optimization procedure is completed, the repump lock should be very stable.

1. Make sure the probe beam power at the detector is ∼250 μW, which corresponds to 3 mW of light diverted from the main path to the lock. This power is easily changed by rotating the half waveplate before the polarizing beam splitter (PBS) cube as seen in Figure 2.6. Note that the detector saturates at 500 μW.

2. Turn up the feedback gain knob until the peak-to-peak voltage of the locking signal is ∼400 mV. The optimum locking signal amplitude is 250–500 mV_{pp}.

3. Turn the phase knob so that locking signal is dispersive and has negative slope.

4. Turn the fast lock on first to make sure that laser is locked to correct transition. Then turn on slow lock and decrease the gain as far as possible while keeping the laser locked.

After using the MOGLabs box for 5 years, we have only encountered one main issue with its electronics and ability to lock to the correct frequency. In August, 2016, the 250 kHz oscillator that is used to internally modulate the laser current and produce a dispersive line signal ceased. This problem was manifested in the absence of a dispersive locking signal. This signal was replaced with noise at the locations corresponding to the atomic transitions. According to MOGLabs, the oscillator relies on the nonlinear behavior of another electronic component in the circuit and can cease when the value of that component drifts over time. Simple adjustments to a couple

of the electronic components in the circuit were made to restore the oscillator. For a detailed description of how to fix this problem, refer to the troubleshooting section in the newest MOGLabs DLC Driver manual online.

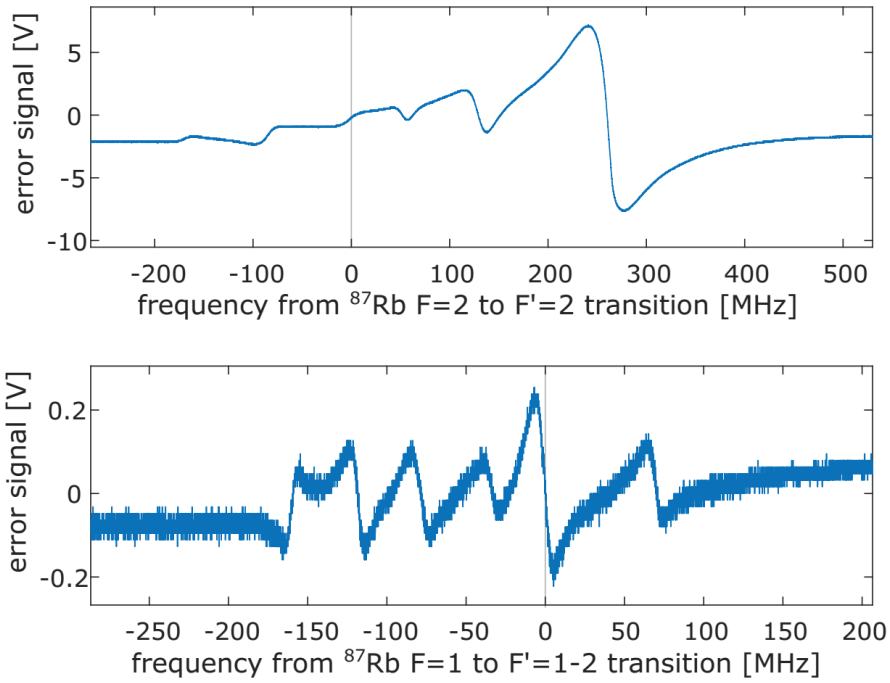

Figure 2.8: Representative scans of the error signal for the cooling (top) and repump (bottom) transitions in ^{87}Rb. The dispersive lineshape for the cooling lock comes directly from the optical setup using polarization spectroscopy while the error signal for the repump lock is generated electronically from a set of Doppler-free absorption dips. Light gray lines indicate the position in each scan where we lock the lasers. Image and caption taken from reference [17].

2.2.2 Cooling Lasers

The cooling master laser is locked to the $|F = 2 \rightarrow F' = 2\rangle$ transition using polarization spectroscopy methods [22, 23, 24]. Polarization spectroscopy utilizes the birefringence induced by a circularly polarized pump beam and results in a dispersive error signal with zero-crossings at the atomic transitions, as seen in Figure 2.8. A thick piece of glass reflects a couple of mW of cooling master light to the polarization spectroscopy lock for frequency stabilization, as shown in Figure 2.9. The dispersive error signal, measured by a photodiode, feeds back on the frequency of the laser

by changing position of the PZT within the External Cavity Diode Laser. We use a home-built lockbox to provide the necessary feedback to stabilize the laser frequency.

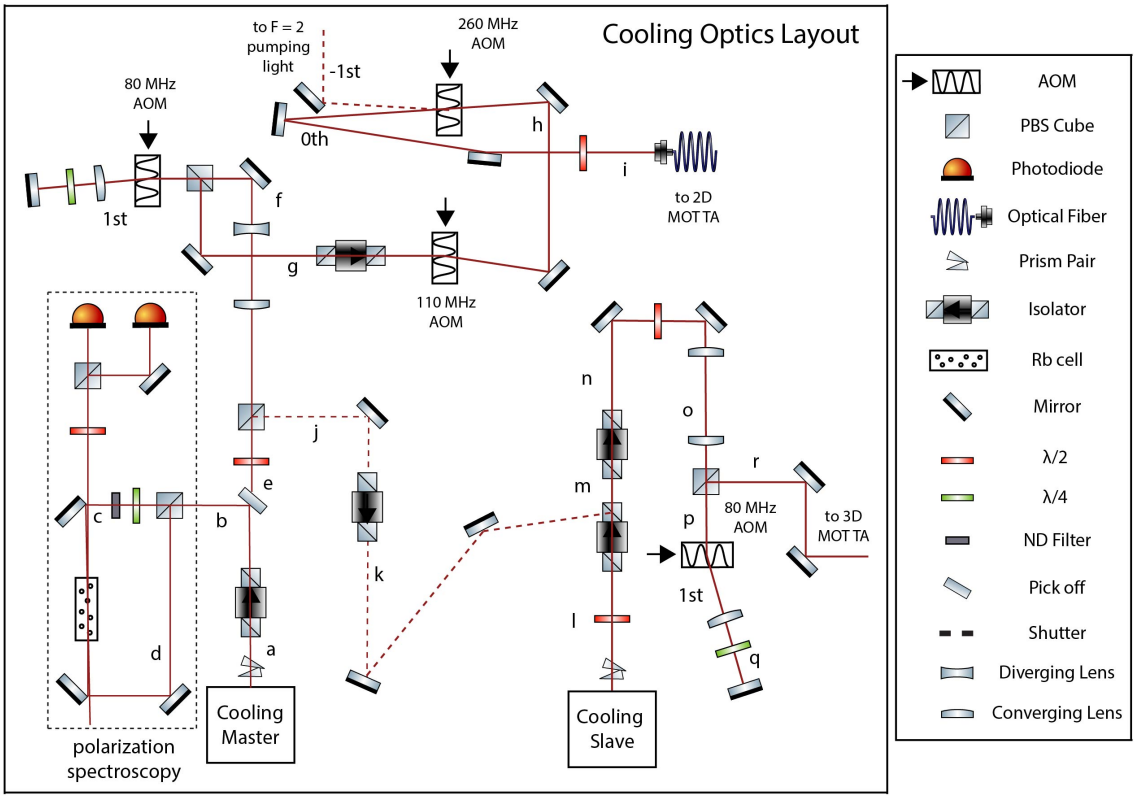

Figure 2.9: Optical layout for cooling master and slave lasers. The cooling master laser is frequency stabilized to a ^{87}Rb transition using a polarization spectroscopy signal that is integrated into an electronic feedback loop. The slave laser is injection locked to the master laser by aligning a small amount of master laser light into the slave laser diode cavity. The following powers can be used as a reference: (a) 76.2 mW, (b) 2.2 mW, (c) 0.229 mW, (d) 0.177 mW, (e) 51.6 mW, (f) 48.3 mW, (g) 30 mW (in all orders), (h) 15.4 mW, (i) 14.2 mW, (j)1.96 mW, (k) 1.5 mW, (l) 81.2 mW, (m) 63.2 mW, (n) 54.3 mW, (o) 48 mW, (p) 43.4 mW, (q) 28.9 mW, and (r) 19.7 mW.

A small amount of master cooling light, determined by a half wave plate and PBS cube, is aligned into the cooling slave diode laser for injection locking. With enough power and correct alignment of the seed light into the slave laser, the slave laser also lases at the $|F = 2 \rightarrow F' = 2\rangle$ transition. For both the master and slave cooling

lasers, the frequency of the light is shifted towards the cooling transition by a double pass through an 80 MHz AOM set at 73 MHz for the master laser and 76 MHz for the slave laser, and a single pass through a 110 MHz AOM set at 102 MHz. These frequency shifts for the master and slave lasers add up to 254.4 MHz and 248.7 MHz respectively. These frequency shifts correspond to master and slave cooling light that is -2Γ and -3Γ detuned, respectively, from the $|F = 2 \rightarrow F' = 3\rangle$ cooling transition.

2.2.2.1 Polarization Lock Problems

When locking the cooling master laser with the home-built lockbox, the desired transition should be centered horizontally and vertically on the oscilloscope using the frequency and signal offset lock box knobs respectively. When the laser frequency is stabilized, the oscilloscope measuring the locking signal will show a low noise horizontal line at 0 V. Occasionally, we have had problems with the lockbox where no amount of loop gain can successfully lock the cooling master laser. We haven't yet found the cause of this problem but suspect that it is related to a charging capacitor on the lockbox electronics board. However, we have experimentally developed the following procedure to restore the lockbox to normal operation.

1. Turn loop switch on while PZT ramp switch is still on. The locking signal should still be seen on the oscilloscope if lock box is not working correctly.

2. Turn down the loop gain until the laser comes fully out of lock. The normal locking signal with the laser scanning will be seen on the oscilloscope.

3. Switch the PZT ramp off and switch the PZT polarity to opposite sign.

4. Turn off the lock box for 30 s and then turn back on.

5. Switch the PZT polarity back to original sign and switch the PZT ramp on.

6. After finding locking transition, slightly turn up the loop gain and turn the loop switch back on. The signal on the oscilloscope should start to look more like a horizontal line.

7. Switch off the PZT ramp and increase the loop gain until the oscilloscope signal is low noise and stable. If the loop gain is too high, the noise on the locking signal will increase which corresponds to frequency noise on the laser.

Another problem that we have observed with locking the cooling master laser is that the overall voltage of the subtraction photodiode signal drifts in time. This corresponds to a change in the zero-crossing of the locking signal and consequently, the stabilization frequency. The cooling master laser is re-locked a couple times each day to re-center the locking signal and set the frequency of the cooling beams back to -3Γ detuned from the cooling transition. We suspect that the photodiode drift is related to polarization drifts of the probe beam. In order to minimize drift of the locking signal, use the following procedure.

1. Rotate the half waveplate before the PBS cube until $\sim 180\mu$W is measured in the polarization spectroscopy probe beam. We have found that the amount of drift is not proportional to the power in the probe beam. Therefore, the more power in the probe beam, the less significant the effect of the drifting lock signal is on the cooling laser frequency. However, it is important that there is not too much power in the probe beam so that power broadening causes the polarization spectroscopy peaks to be less defined.

2. Change the cooling master laser current until the light is no longer on resonance with any Rb atomic transitions and switch off the PZT ramp. Use the IR viewer to confirm that atoms in the Rb cell are not fluorescing at the new drive current.

3. Plug the photodiode voltage directly into the oscilloscope, bypassing the lockbox. Balance the powers in both probe beams, or set the subtraction photodiode signal to 0 V, by rotating the half waveplate before the photodiode. Equal powers in both beams incident on the photodiode minimizes drift of the subtraction photodiode voltage.

4. Connect the photodiode voltage back to the lockbox, switch on the PZT ramp, and change the current until the desired locking signal is seen on the oscilloscope. Use signal offset knob to center the locking signal at 0 V on the oscilloscope and re-lock the cooling master laser.

2.2.3 Injection Locking

The cooling and master slave lasers are injection locked to their respective master lasers when the seed light is well enough aligned into the slave diode laser that amplification is induced at the frequency of the injected light. Currently both injection locks are aligned such that 5 mW of repump seed light and 2 mW of cooling seed light successfully injection locks the slave lasers as long as the free-running wavelength of the slave laser is tuned closely to the wavelength of the master laser. This

corresponds to setting the current on the laser diode driver within a certain range of current values. Both 2x4 and 2x6 fiber splitters have a 1% tap for each input that is sent into a Thorlabs scanning Fabry-Perot cavity for frequency monitoring of the cooling and repump frequencies for both the 2D and 3D MOTs. Figure 2.10 shows a Fabry-Perot trace with all four frequencies present. When the repump and cooling slave lasers are injection locked, there are 4 peaks shown on the Fabry-Perot cavity trace. Two sets of almost overlapped peaks are separated by 5.4 ms which corresponds to the frequency difference between the cooling and repump transitions. The peaks corresponding to the slave lasers are slightly displaced from their corresponding master laser peaks due to differences in alignment into the cavity. Use the following procedure for day-to-day injection locking.

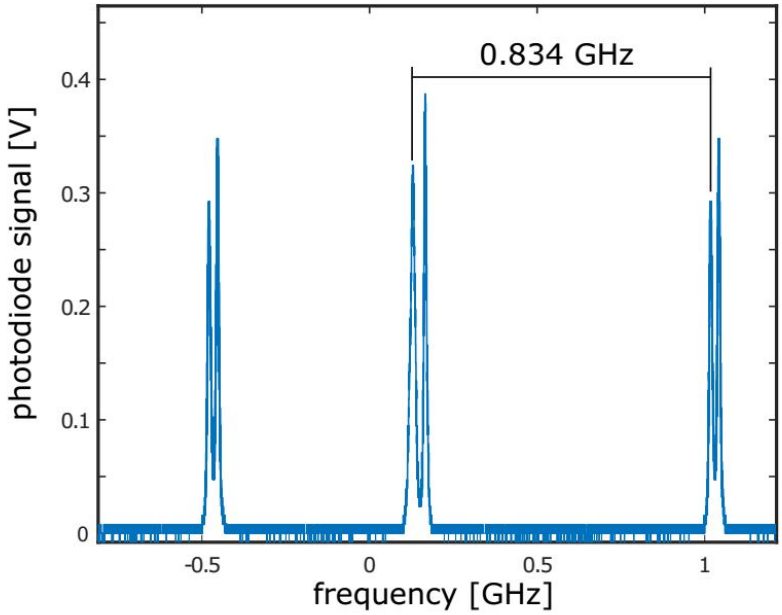

Figure 2.10: Scanning Fabry-Perot (FP) cavity trace of the repump and cooling lines. The free spectral range of the FP cavity is 1.5 GHz. The ground-state splitting in ^{87}Rb is 6.834 GHz, so the repump and cooling lines are separated by 6.834 GHz modulo 1.5 = 0.834 GHz. The master and slave lasers show up as separate peaks due to slight differences in alignment into the FP cavity. Image and caption taken from reference [17].

1. Set the master and slave lasers to the currents given in Table 2.1. The temperatures are also given for reference.

Table 2.1: Current and Temperature values for Diode Lasers

Laser	Driver Current (mA)	Set Temperature (°C)
Repump Master	117.38	17.79
Repump Slave	108.77	15.75
Cooling Master	126.45	18.5
Cooling Slave	123.89	18.0

2. After lasers have warmed up for 10–15 min, change the frequency on the master lock boxes to see the correct spectroscopy peaks shown in Figure 2.8.

3. Change the slave laser currents slightly until the slave lasers are injection locked. The slave laser peaks on the Fabry-Perot cavity signal will oscillate with their respective master laser peak when injection locked. Usually the repump slave current will not need to be changed from 108 mA for injection locking. After setting the cooling slave laser current to 123.89 mA, some of the slave laser power will lase at the frequency of the cooling master laser. In order to injection lock the full slave laser power, make small adjustments to the drive current until there is a single cooling slave laser peak observed on the Fabry-Perot oscillating with the cooling master peak.

4. Lock the master lasers and check on Fabry-Perot to make sure all lasers are single-mode and that the slave lasers remain injection locked.

2.2.3.1 Injection Locking Realignment Methods

If the seed light path is misaligned into the slave laser and no amount of changing the laser current will injection lock the laser, use the following alignment procedures. Use Injection Locking Alignment Method 1 when there is still some amount of seed light aligned back into the slave laser. Use the more involved Injection Locking Alignment Method 2 when the first method is not successful or when first setting up an injection lock.

Injection Locking Alignment Method 1:

1. Increase the power of the seed light to a couple of mW above the measured power.

2. Change the current on the diode laser driver 5–10 mA around the values given in Table 2.1 and use the Fabry-Perot trace to determine if any amount of slave laser power is injection locked.

3. If a small peak starts to oscillate with the master laser peak on the Fabry–Perot, use the last mirror in the injection locking path before the isolator to change the alignment into the slave laser and increase the height of the injection locked peak.

4. Once the slave laser is single-mode and fully injection locked, reduce the seed light power until the laser starts to come out of lock and then further optimize the seed light alignment until the laser is fully injection locked. Iteratively decrease seed light power and change alignment into slave laser until the slave laser is injection locked with the lowest amount of power. This means that the alignment of the seed light into the slave laser is optimized.

5. Increase the seed light power 0.5 mW above the minimum power needed for injection locking. This allows the laser to be easily injection locked within a range of drive currents.

Injection Locking Method 2:

1. Align a couple of mW of seed light into the slave laser by overlapping seed light with the slave laser light that is rejected from the isolator. Check that the seed light is well enough aligned into the slave that there is at least $\sim$1 mW measured at the front facet of the slave laser.

2. Try Method 1 again.

3. If Method 1 doesn't work, an Optical Spectrum Analyzer (OSA) is necessary to finish the alignment procedure. Replace the fiber that couples the slave laser light into the fiber splitter with a fiber that couples the light into the OSA.

4. When the slave laser is not injection locked but light from the master laser is aligned into the slave laser, the slave laser light on the OSA should show 2 peaks: one at the frequency of the master laser and one at the frequency of the slave laser. Temperature tune the wavelength of the slave laser as close to the injected light wavelength as possible.

5. Once the peaks are close and the temperature of the slave laser has been stabilized, change the drive current of the slave laser until the peaks overlap. When the laser is close to being injection locked, the peaks will be slightly overlapped but the

overall peak will look asymmetric. Change the current to further overlap the peaks until the slave laser is injection locked. The transition to injection locking is observed on the OSA as a wide "bumpy" peak that becomes a narrow and symmetric peak upon injection locking.

6. Replace the OSA fiber with the fiber splitter and use the Fabry-Perot trace to confirm that the laser is fully injection locked. When the injected light is blocked, 2 distinct peaks will be seen on the oscilloscope and when the injected light is unblocked, the 2 peaks will overlap and move together.

2.3 Tapered Amplifiers

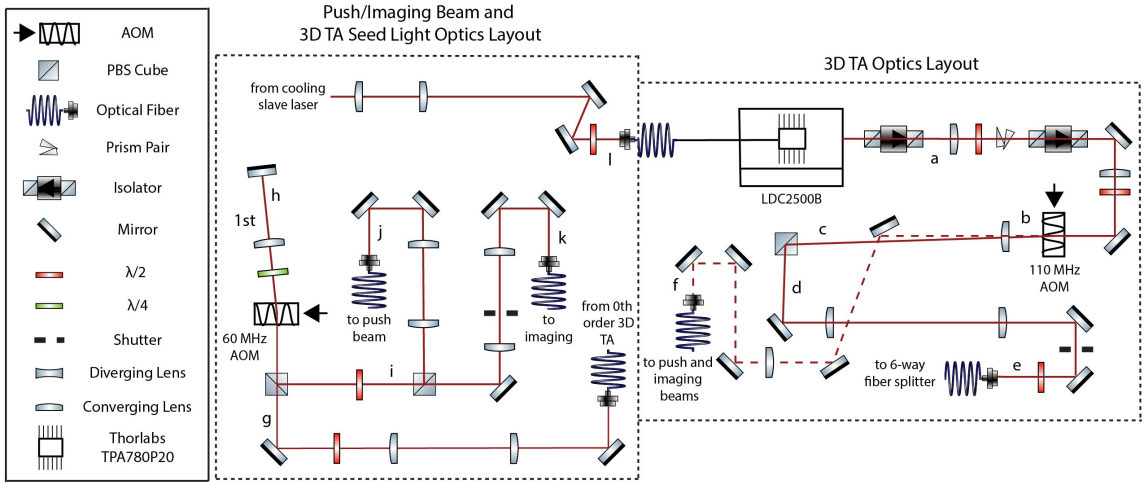

Figure 2.11: Optical Layout of 3D Tapered Amplifier and push and cooling beams. Use the following powers for alignment and debugging as needed. Powers (a) - (f) were measured at 900 mA drive current: (a) 195 mW, (b) 159 mW (in all orders), (c) 105.5 mW, (d) 91.4 mW (e) 84.3 mW, (f) 32.6 mW. Powers (g) - (k) were measured at 1900 mA drive current: (g) 11 mW, (h) 5.2 mW, (i) 2.35 mW (j) 1.15 mW, (k) 1.2 mW. Power (l) is the seed light power into the 3D MOT TA and it is constant at 18.5 mW.

In order to provide enough power at the cooling transition for both the 2D and 3D MOTs, the output of each cooling laser is sent to a Thorlabs TPA–780P20 Tapered Amplifier (TA). Each TPA–780P20 amplifier is driven by a Thorlabs LDC2500B current and temperature controller. With 10–15mW of seed light power, the amplifier

outputs up to 2 W at the maximum drive current of 2.5 A. Normally, we run our amplifiers at 1.9 A, which corresponds to about 1 W of output power. The amplifier output is sent through a series of optics used to shape the beam and fiber couple it into either 2x4 or 2x6 fiber splitters. The master cooling laser output seeds the 2D MOT amplifier, whose output provides cooling light to the 2D MOT through the 2x4 fiber splitter. Similarly, the slave cooling laser output seeds the 3D MOT TA, providing the cooling light to the 3D MOT through the 2x6 fiber splitter. The 3D MOT optical layout is shown in Figure 2.11. The 2D MOT TA optical layout is almost identical, with the exception that the 110 MHz AOM in a single-pass configuration is placed after the 3D MOT amplifier but before the 2D amplifier. The 110 MHz AOM is used to shut the 3D cooling light off quickly during the experiment and therefore must be located after the 3D MOT amplifier. It is not necessary to shut off the 2D cooling light quickly, so a physical shutter is sufficient for blocking the output of the 2D MOT amplifier during the experiment.

In general, the Thorlabs Tapered Amplifiers have performed well in providing sufficient cooling power to both of the MOTs in order to cool and trap $\sim 5\times10^9$ atoms in the 3D MOT. However, because these amplifiers are a relatively new product, there are still some problems that have been worked out in the last couple of years. Section 2.3.1 provides an overview of the problems that have been observed with the tapered amplifiers and drivers, how the problems affected the experiment and how they were resolved. I also discuss our daily alignment procedure for these amplifiers.

2.3.1 Tapered Amplifier Problems

2.3.1.1 Problems with Input Coupling to Amplifier

One problem we have observed with the Thorlabs Tapered Amplifiers is degradation of the seed light input coupling to the amplifier. We first observed this problem as a steady decrease in the 2D MOT TA output power over the course of a week. Decreased cooling power in the 2D MOT beams resulted in smaller 2D MOTs and longer 3D MOT loading times. After measuring 12 mW of input seed light and optimizing the input coupling efficiency, there was no increase in amplifier output power. Our contacts at Thorlabs Quantum Electronics Division informed us that degredation of the input coupling to the amplifiers was a problem with some of their early devices. An epoxy used to bond the input fiber to the amplifier had been thermally activated due to hours of continuous use with low power input seed light. This created a film over the amplifier front facet reducing input light coupling capability. After re-installing the repaired device into the setup, the measured power out of the 2D MOT TA was back to the normal value.

After a couple of years of normal performance, the same amplifier chip starting exhibiting uncharacteristic behavior. This behavior manifested itself in slightly lower amplifier output powers and a component of the power with an unstable frequency, observed in the Fabry–Perot cavity trace as a small peak that moved and changed shape even when all lasers were locked. We suspect that this moving peak on the Fabry-Perot trace corresponded to spontaneous emission instead of stimulated emission output. At first, this behavior went away after re-optimizing the seed light coupling into the amplifier. However, after about a week, there was a clear deterioration in output power and an increased percentage of spontaneous emission in the amplifier output. In order to determine whether this behavior was due to natural deterioration over the amplifier's lifetime or another problem with input coupling to the amplifier, the Amplifier Spontaneous Emission (ASE) output power was measured at different drive currents for both the 2D and 3D MOT amplifiers. These measurements were done while blocking the input seed light to ensure that only ASE and not spontaneous emission output power was measured. The measured data are shown in Figure 2.12. After comparing the ASE vs. drive current curves of each amplifier to each other and the initial curves given in the amplifier datasheets, we determined that the problem was not due to natural degradation of the chip. The ASE emerging from the front of the amplifier in the direction of the seed light was also measured at drive currents of 800 mA and 1 A. According to Thorlabs Quantum Electronics Division, $\sim$2 mW should be measured at 1 A drive current. The measured power was 51 μW at 800 mA and 200 μW at 1 A for the 2D MOT TA. For the 3D MOT TA, 1.9 mW was measured at 1 A. This indicated that there was another issue with the input coupling to the chip. The chip has since been repaired and we have had no further issues with the input coupling. The ASE power out the front of the 2D MOT TA is now measured to be 3.8 mW.

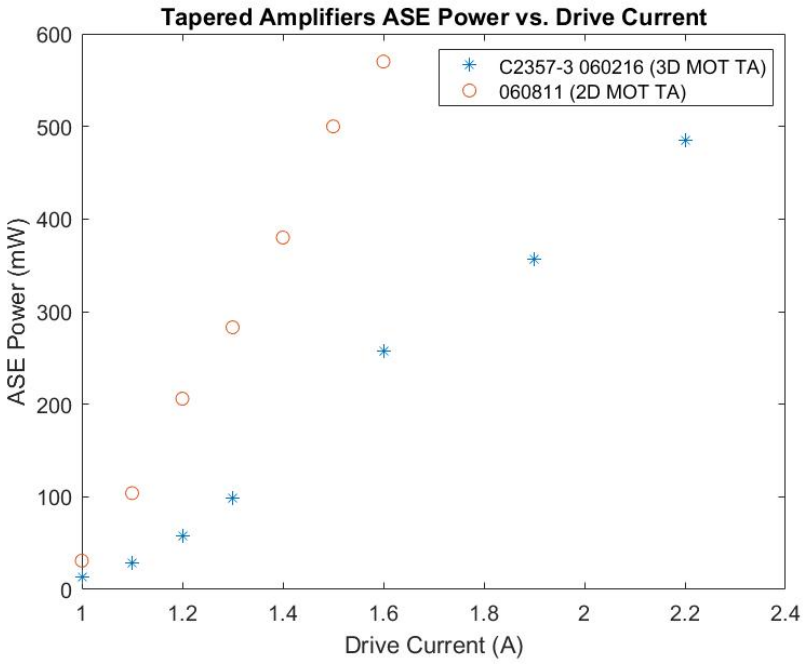

Figure 2.12: Amplified Spontaneous Emission curves for both 2D and 3D MOT Tapered Amplifiers. These curves give more information at low drive currents than the Tapered Amplifier datasheets. For debugging TA problems, measure the ASE curves to see if the problem is due to natural degradation over the chip's lifetime (ASE powers measured will be lower than the powers in this graph) or if another problem is responsible for the observed behavior. The ASE out of the amplifiers was measured by blocking the seed light into the amplifier and measuring the output power.

2.3.1.2 Output Power Fluctuations

One issue that we have observed with the 3D cooling amplifier is that occasionally the output power instantly drops to 90% of the overall output power and after 6 s, jumps back to initial value Figure 2.13 shows how the changing 3D cooling power affects the overall 3D MOT number. We measured the input seed light power to be constant in time, confirming that the seed light was not causing the output power fluctuations. Eventually both the seed light input coupling and the amplifier output coupling into the 2x6 fiber splitter was re-optimized and the output power was stable to 1%. We suspect that the fluctuating output power was possibly due to back reflections in the optical setup causing power instabilities in the amplifier.

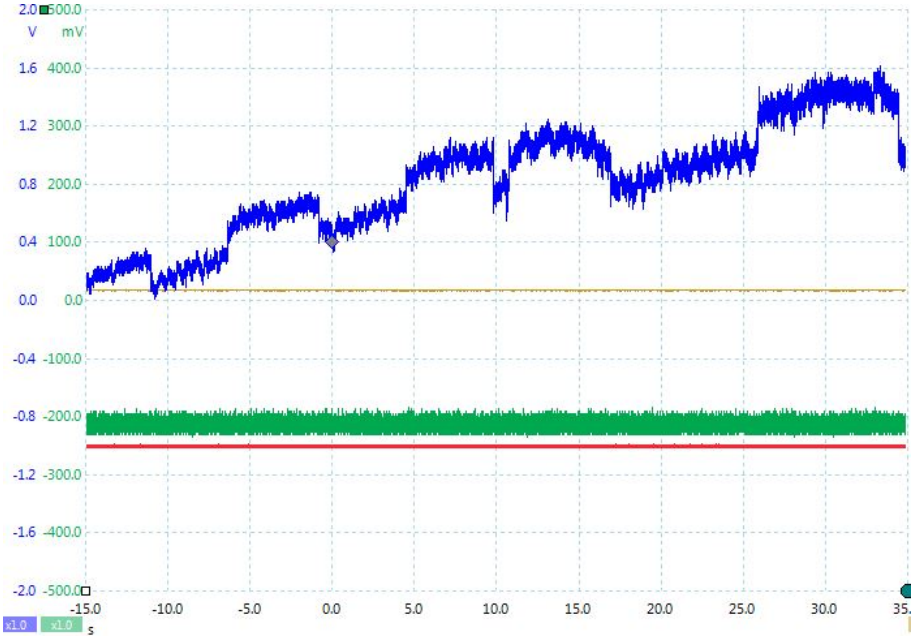

Figure 2.13: Picoscope trace of the MOT fluorescence level which is proportional to the number of atoms in the MOT. The unstable MOT number is completely due to power fluctuations out of the 3D MOT TA. The power fluctuation level is 10 % and the period of the oscillations is 6 s.

2.3.1.3 Current Instability in Thorlabs LDC2500B Driver

The LDC2500B driver that drives the Tapered Amplifiers is externally controlled by the user through a LabView program that interfaces wth the driver. The LabView program graphs the amplifier driver current, the chip temperature and the package temperature as measured by thermistors in the temperature control feedback loop. Instabilities in the amplifier drive current have been observed on the LabView drive current graphs. Initially, the graph indicated that the was the drive current was oscillating between 1600 mA and 0 mA. However, we measured no change in the amplifier output power. Eventually, the graph indicated that the current spiked down to 0 mA and remained at 0 mA drive current for 10-15 s before spiking back up to 1600 mA. Again no change in amplifier output power was measured. We found that at drive currents of 1550 mA or less, diver current instabilities were no longer a problem. After six months of normal operation at 1550 mA drive current, the current instabilities returned. At this time, the current graph indicated that the drive current spiked down to 0 mA and remained at that current for a minute at a

Table 2.2: MOT beam powers

	Seed Light Power (mW)	Fiber Splitter Output Power (mW)
2D MOT TA	14.2	63 (in fiber #4)
3D MOT TA	18.5	28 (in fiber #5)

time. At the same time, the LabView program Laser On/Off indicator turned off and the amplifier output power was measured to be 0 mW. At first, the driver only shut off the amplifier once every couple of days. However, after about a month, this started to happen multiple times a day. After receiving a new driver from Thorlabs, we have not seen any of the same behavior.

2.3.2 Daily Use of Tapered Amplifiers

Because the outputs of both tapered amplifiers are coupled into fiber splitters that provide the cooling light for both 2D and 3D MOTs, it is important that the coupling efficiency into the fiber is relatively constant throughout the day. This corresponds to constant cooling power in the MOT beams and a total MOT loading number that does not drift throughout the day. The alignment of the amplifier output into the fiber splitters is dependent on the temperature of the air inside the TA box. Because the TAs dissipate a lot of heat at high drive currents, it is important to allow the system to re-thermalize after turning the amplifier up to high drive currents. After waiting for $\sim$30 minutes, peak up the coupling efficiency in both fiber splitters by measuring the output power of one 2D and one 3D MOT fiber and slightly changing the vertical alignment of the amplifier output beam into the fiber splitters. The horizontal alignment is not sensitive to temperature drifts and rarely needs to be changed. Once this quick alignment is done with the amplifiers, the cooling power in the MOT beams is stable to 15% throughout the course of the day. Reference Table 2.2 for nominal input seed light powers and fiber splitter output powers at 1900 mA drive current for both amplifiers. For a more detailed description of power loss in the TA optical layout, refer to Figure 2.11. These powers should serve as a reference to help diagnose future problems and alignment issues with the tapered amplifiers.

2.3.3 Push Beam/Cooling Imaging Optics

Both the push beam and cooling imaging light are derived from the discarded 0^{th} order beam from the 110 MHz AOM inside of the 3D MOT TA box. As seen in Figure 2.11, the 0^{th} order beam is picked off and coupled into a fiber inside of the 3D MOT TA box. Because the AOM alignment is optimized for power in the 1^{st} order, the 0^{th} order beam has a messy profile with a set of vertical dark lines through the center of the beam. We use the fiber as a spatial filter to clean up the transverse mode of the beam. As seen in Figure 2.11, the output of the fiber is sent to a 60 MHz AOM in a double-pass configuration whose output is coupled into both the push and cooling imaging beam fibers. During the MOT loading stage, the AOM operates at 59 MHz, corresponding to $-1/3\Gamma$ detuned from the $|F = 2\rangle \rightarrow |F' = 3\rangle$ cooling transition. During this stage, the push beam shutter is open while the imaging shutter is closed and light on resonance with the cooling transition is sent axially down the vacuum chamber to increase the 3D MOT loading rate. The imaging shutter is opened immediately before the imaging pulse and the AOM frequency is changed so that the imaging light is detuned anywhere between -5Γ and $+5\Gamma$ from the cooling transition. The specific detuning used during imaging will be discussed in more detail in Chapter 4.

2.4 Rb Dispenser/MOT Loading

As explained in Section 2.1.1, Rb is evaporated into the vacuum chamber through a chemical reaction that occurs when the dispenser is heated up. Running 3.15 A through the filament connected to one of the Rb dispensers evaporated enough Rb into the 2D MOT cell to load approximately 3×10^9 atoms in the 3D MOT with a loading time of $\sim$45 s. Figure 2.14 shows a MOT loading curve recorded for the loading conditions discussed above.

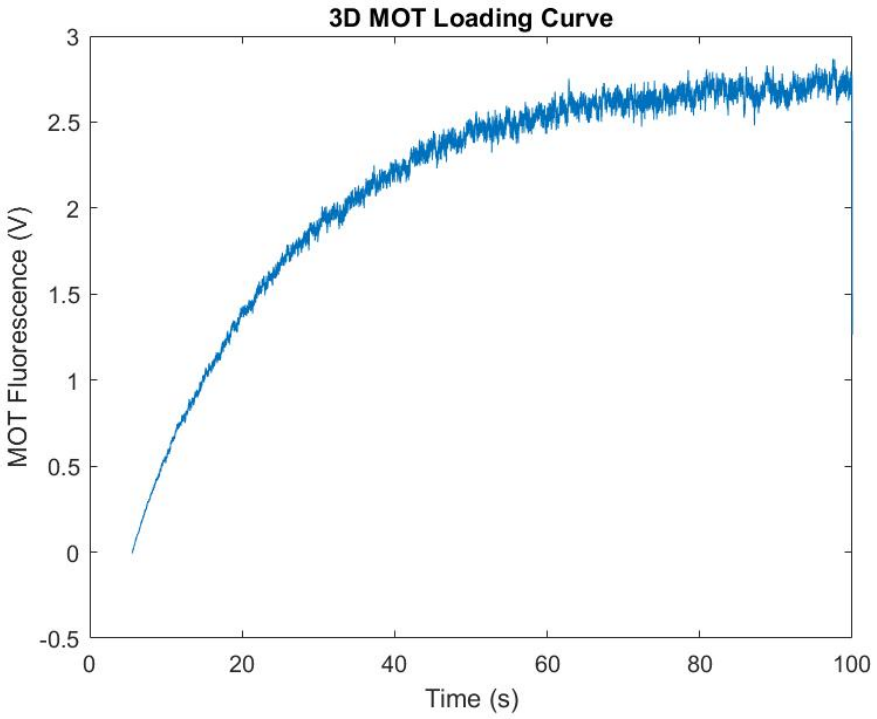

Figure 2.14: 3D MOT loading curve with 3.15 A on Rb dispenser power supply. After failure of Rb dispenser power supply. The dispenser evaporates enough Rb into the 2D MOT cell to load the 3D MOT to $\sim 3 \times 10^9$ atoms in about 45 s.

On April 5th, 2017, the power supply that supplies current to the filament connected to the Rb dispenser failed. This failure was manifested in a loud clicking noise from the power supply, the smell of burning plastic, and an unknown amount of current flowing through the filament for a couple of minutes. The Tenma 32 V, 5 A power supply supplied enough current to the filament during failure that the filament physically became disconnected from the lead. Fortunately, the ground wire that is used for all 3 Rb dispensers was still intact, which allows the other 2 Rb dispensers to be used in the future. As the power supply drove high currents through the dispenser filament, the filament heated up the dispenser enough to flood the chamber with Rb, resulting in a pressure spike in the vacuum chamber. However, vacuum remained intact during the power supply failure and the vacuum chamber was pumped down to less than 10^{-10} Torr by the next day. Refer to Table 2.3 for more information regarding pressures during the power supply failure.

Table 2.3: Vacuum Chamber pressure gauge reading for variable times after power supply failure.

	10 min	30 min	90 min
Pressure Reading (nA)	76	10	2

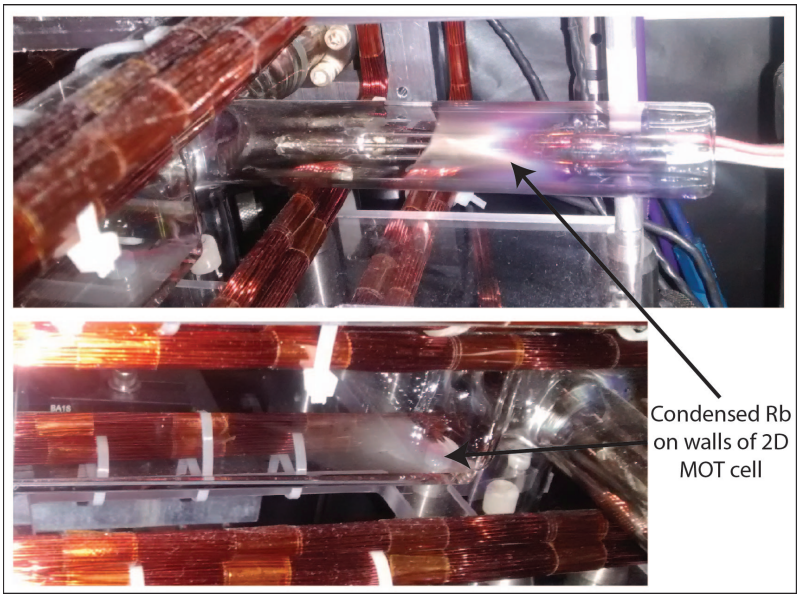

Figure 2.15: Pictures of the 2D MOT cell after failure of the Rb dispenser power supply. Condensed Rb can be seen on the walls of the main 2D MOT cell and in the adjacent arm that contains the Rb dispensers.

After the Rb flooded the vacuum chamber, it condensed on the sides of the 2D MOT cell, as seen in Figure 2.15. Due to the power supply failure, there is now enough Rb in the 2D MOT cell to load the 3D MOT in about 3 s without actively evaporating Rb into the chamber with either of the two remaining Rb dispensers. A typical MOT loading curve taken after the power supply failure is shown in Figure 2.16. The apparatus repetition rate has greatly increased as a result of this power supply failure.

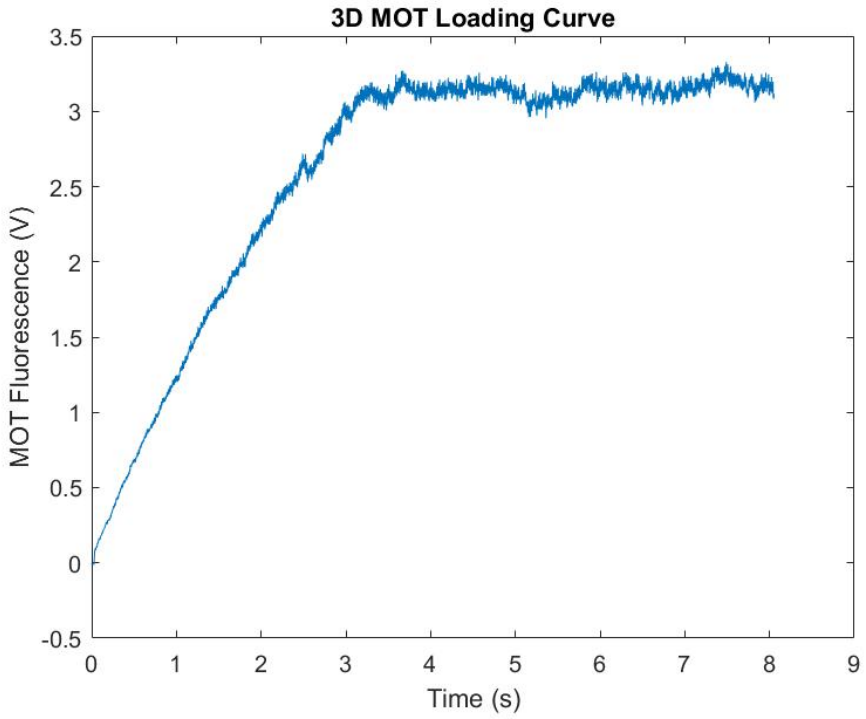

Figure 2.16: 3D MOT loading curve after failure of Rb dispenser power supply. The abundance of Rb in the 2D MOT cell has increased the partial pressure of Rb enough to create 2D MOTs that load about 5×10^9 atoms in the 3D MOT in $\sim$3 s.

2.5 Controlling the Transfer Current

The transfer current control circuit is composed of 5 components: TDK power supply, the transfer coil pairs, Flyback diodes, high powered MOSFETs and Hall Probes/Feedback circuit. These components work together to precisely control the current through the transfer coil pairs following analog outputs from the timing program. A TDK Lambda Genesys 50–200 10 kW power supply is used to drive up to 200 A through the transfer coils during the transfer sequence. The positive terminal on the power supply is directly connected to the positive lead on each transfer coil pair, as seen in Figure 2.17. The negative terminal of each coil pair is connected to the Drain terminal on a pair of high powered IXFN180N10 MOSFETs used to control the amount of current through each coil pair. The Gate voltage for each MOSFET is controlled by the timing computer. The Source terminals on the high powered MOSFETs are all connected to a water cooled aluminum plate, which is

used to facilitate power dissipation in the MOSFETs, and are then connected to the negative terminal on the TDK power supply through three 3 AWG cables. FW Bell CLSM 200-LA Closed-Loop Hall effect sensors are used to monitor the current through the transfer coils. They are used in the feedback loop to stabilize the current and in the interlock circuit to protect the coils from too large of currents. The last component of the transfer current control circuit is a Flyback Diode which is placed in parallel with each coil pair to protect the MOSFETs from large induced voltages when the current is turned off quickly.

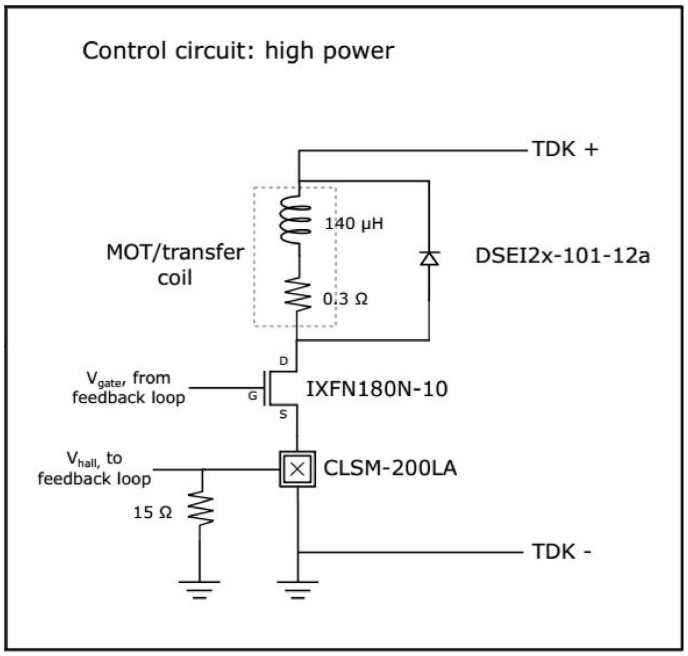

Figure 2.17: Electronics diagram of transfer current control circuit. Figure taken from [17].

2.5.1 Flaw in Transfer Circuit Design

When the transfer current control circuit was originally constructed, a single cable was used to connect the positive terminal on the TDK power supply to the transfer coil pairs and to connect the aluminum plate, which is connected to the Source terminal on all of the MOSFETs, to the negative terminal on the power supply. We used 3 AWG wire, which has a very small non–zero resistance, to make these connections. However, during transfer, up to 200 A flows through the transfer coils, and consequently through the 3 AWG cable that connects the MOSFETs to the power

supply. A 10 ft 3 AWG wire has a resistance of $\sim$0.002 Ω which corresponds to a 0.4 V drop across the cable when 200 A runs through it. Because the negative terminal on the power supply is connected to the lab ground, the 0.4 V drop across the wire would cause the MOSFET Source voltage to be 0.4 V instead of lab ground. Because the voltage drop across the 3 AWG cable is proportional to the total current out of the TDK power supply, the Source voltage relative to the lab ground depends on the total current out of the TDK power supply. The current through each MOSFET depends on the the Gate voltage relative to the Source voltage, which results in MOSFET current that is greatly affected by the changing Source voltage.

This problem was originally observed in our lab during the first magnetic transfer attempts. After debugging the apparatus and the transfer current control circuit to determine the cause of low transfer efficiency, we found that the individual coils had pickup proportional to the total current out of the TDK power supply. Eventually, we also measured the changing source voltage due to the voltage drop across the 3 AWG single cable that connects the MOSFETs to the TDK power supply. In hindsight, if the original design had been modified so that each MOSFET source had an individual connection to the TDK power supply, the changing source voltage would be proportional to current flowing through one MOSFET instead of the total TDK output current. Instead of completely re-constructing the transfer current control circuit, we modified the feedback circuit to add the source voltage measured at all times to the gate voltage output from the feedback circuit. When the source voltage is actively added to each gate voltage, the changing source voltage is accounted for and the current through each individual MOSFET is no longer dependent on the total current through the transfer coils. After modifying the feedback circuit in this way, the current measured through each of the coils showed that the current through the coils was following the current ramps originally programmed in the MATlab transfer current code.

2.6 Ground Loop Problems

Ground loops occur when the equipment and electrical wiring configuration allow more than one path for electricity to flow to ground. This can result in stray signals, noise, and interference. In our apparatus, ground loops have manifested themselves in stray signals on many different electronic devices in the lab. This effect was first observed in the cooling laser coming unlocked when running around 200 A through the transfer coils. After much debugging, we eventually measured a voltage proportional to the current through the transfer coils on the cooling master laser locking signal. This caused the laser to unlock every time high currents were sent through

the transfer coils. This signal also showed up on the output voltage of the Fabry-Perot, the piezo driver and even the output of a laser current driver. To eliminate this signal on the cooling lock box and all other electronic equipment in the lab, we implemented the "star grounding method" described in Reference [25] for all our homebuilt electronic devices. We also changed our procedure for connecting commercial electronic equipment to the lab ground. To eliminate multiple paths to ground, each electronics box is connected to a central ground (star ground) separately. To implement the star grounding method in homebuilt electronics, use the following steps:

1. Put each circuit in a separate box.

2. Provide a separate connection to the star ground for each cases that houses a circuit.

3. The optics table is used as the star ground in our lab and every homebuilt electronics box is connected to the table through ground lugs and grounding cables.

4. Never attach case grounds to circuit boards directly. The ground for the circuit comes directly from the power supply that is powering the circuit.

5. Signal lines are shielded at one end. The convention chosen in our lab is to ground the sending side of the signal to the case by using non-isolated BNC connectors on the outputs of the circuit. The receiving side of the signal is not grounded and is connected to the circuit through isolated BNC connectors.

This star grounding method has significantly helped reduce problems arising from ground loops in the lab. We have also organized how commerical electronic equipment is grounded to the lab ground by connecting every piece of equipment in a given system to a single power strip. We define a system as a group of devices that is connected through signal carrying BNCs. The following list groups devices into systems that are plugged into a single power strip.

- Power strip 1: Laser current drivers, temperature controllers, repump master lock box, repump oscilloscope.

- Power strip 2: AOM drivers, frequency counters, AOM digital input power supply.

- Power strip 3: Coil power supply, MOSFET box power supply, vacuum pump.

- Power strip 4: all 3 laptop supplies, Fabry-Perot driver, and Fabry-Perot oscilloscope.
- Power strip 5: ± 15 V supply for cooling lock box, cooling oscilloscope, function generator, piezo driver. Power strip 5 contains all the electronic equipment related to the cooling laser lock system. This is the most important system to keep isolated because any noise on laser locks can result in the laser becoming unlocked.

The electronic systems listed above have not been updated since they were originally organized to reduce ground loop problems. However, the list serves as a reference for debugging and as a grounding-scheme model for the organization of future devices integrated into the lab.

CHAPTER 3

Construction of BEC Apparatus - Phase 2

BEC was first achieved in our lab in December, 2015. Since then, updates have been made to the apparatus, with the help of Andrew Schaffer, to decrease the overall BEC creation time, increase the BEC atom number, and implement a trapping laser for BEC creation in a flexible hybrid optical-magnetic trap for 2DQT experiments. This chapter focuses on these updates, the implementation of new equipment and a description of the modified BEC creation process. Section 3.1 describes the implementation of a 532-nm laser used to create a plugged quadrupole trap. Section 3.2 describes the first stage of evaporative cooling: RF evaporation in the plugged quadrupole trap. Section 3.3 introduces the newly implemented Optical Dipole Trap. Sections 3.4 and 3.5 discuss transfer to a hybrid optical-magnetic trap and optical evaporation to BEC.

3.1 Plugged Quadrupole Trap

As discussed in Chapter 2, a spherical quadrupole field with a local minimum acts as a trap for weak field seeking states, such as ^{87}Rb $|F = 1, m_F = -1\rangle$. After atoms are transferred from the 3D MOT cell to the BEC cell, the transfer coils are ramped off while the BEC quadrupole coils are ramped up to a vertical gradient of 250 G/cm. The BEC quadrupole coils are oriented in an anti-helmholtz configuration creating a magnetic field with local minimum at the center of the coil pair. The magnetic field magnitude linearly increases away from the center of the coil pair. Modifications to the quadrupole trapping geometry are necessary to avoid Majorana losses, which are discussed in Section 3.1.1. A repulsive optical barrier is aligned to the center of the quadrupole trap, creating a plugged quadrupole trap that provides a nearly linear conservative trap for efficient RF evaporative cooling.

3.1.1 Majorana Losses

As atoms approach the $|\vec{B}| = 0$ point of the quadrupole field, the magnetic field direction rapidly changes and atoms undergo nonadiabatic spin flip transitions to untrappable states. This mechanism is referred to as Majorana losses and results in atoms loss and heating. For high temperature atom clouds, atoms do not spend

much time near the center of the trap and consequently are not lost. This is the case for the atom cloud in our apparatus immediately after transfer to the BEC cell. However, as atoms are further cooled, they spend more time near the center of the trap and can be lost. Current methods for minimizing Majorana losses include the Time-averaged Orbiting Potential (TOP) trap [26], the Ioffe-Pritchard trap [27, 28], the quadrupole-Ioffe-configuration (QUIC) trap [29], and the plugged quadrupole trap [30]. A TOP trap was initially implemented in our lab to minimize Majorana losses. The TOP trap is comprised of a quadrupole field and a rotating bias field which shifts the $|\vec{B}| = 0$ point outside of the atom cloud. For more details regarding the the TOP trap implemented in our lab, refer to Newman's dissertation [17].

One disadvantage of the TOP trap is that it provides weaker confinement than a quadrupole trap, which results less efficient evaporative cooling. We have successfully reached BEC through RF evaporation in the TOP trap. However, this evaporation process lasted about 60 s, during which, the quadrupole coils heated up a considerable amount. By the end of the day, the interlock protection circuit disabled the BEC coil power supply due to dangerous temperatures measured in the BEC quadrupole coils near the end of the BEC creation process. In order to avoid excessive heating of the BEC quadrupole coils during the BEC creation process, we changed the trapping geometry from a TOP trap to a plugged quadrupole trap, in which more efficient and faster evaporative cooling occurs.

3.1.2 Repulsive Optical Barrier

Far-detuned and high-intensity lasers are used to provide both attractive and repulsive potentials for neutral atoms. The electric field of the light field incident on the atoms induces an atomic dipole moment. The interaction between the electric field of the laser and the induced dipole leads to the following potential energy [31]:

$$U_{dip}(\mathbf{r}) = \frac{3\pi c^2}{2{\omega_0}^3}\frac{\Gamma}{\Delta}I(\mathbf{r}) \tag{3.1}$$

where $I(\mathbf{r})$ is the spatially dependent intensity of the laser, $\Gamma = 2\pi \times 6.07$ MHz is the natural linewidth for ^{87}Rb [32] and Δ is the detuning between the resonant atomic frequency ω_0 and the laser frequency ω. The sign of the dipole potential is given by the detuning of the light field from atomic resonance. Therefore, the potential produced by a red-detuned ($\Delta < 0$) laser beam is negative and the potential minimum is found at the location of maximum intensity of the laser, resulting in an attractive potential. However, for a blue-detuned ($\Delta > 0$) laser, the dipole potential is positive and atoms are repelled by the light field. In this way, the dipole interaction

from a blue-detuned laser creates an optical barrier that most strongly repels atoms at the maximum intensity part of the beam. A plugged quadrupole trap utilizes a blue-detuned laser beam focused at the center of the quadrupole field, creating a repulsive barrier that keeps atoms away from the $|\vec{B}| = 0$ Majorana loss region as shown in Figure 3.1.

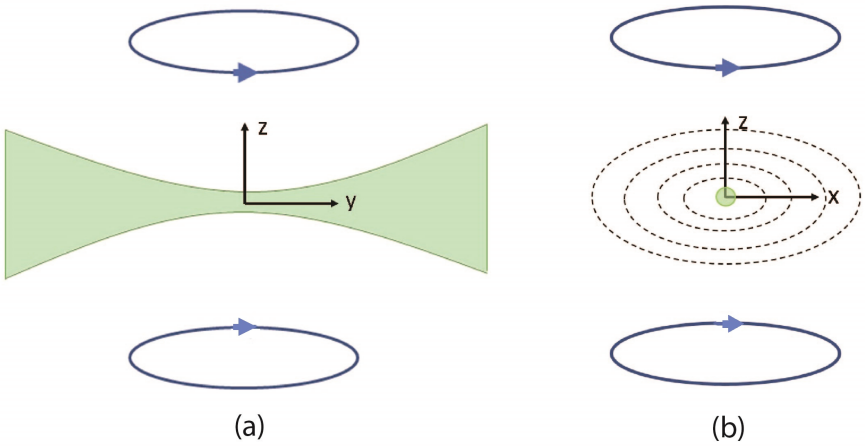

Figure 3.1: Conceptual diagram of plugged quadrupole trap. The spherical quadrupole field is created by a pair of magnetic field coils in an anti-helmholtz configuration. A blue-detuned laser beam is focused at the local minimum of the quadrupole field, plugging the trap region where Majorana losses occur. (a) The plug beam propagates along the y axis. (b) Dashed lines represent in the xz plane represent isomagnetic lines, or lines of constant magnetic field magnitude. The plug is focused at the center of the quadrupole field and propagates perpendicular to the xz plane.

3.1.3 Plug Beam Setup

3.1.3.1 Verdi Laser

A diode-pumped solid-state frequency doubled Nd:YVO_4 Verdi laser provides the blue-detuned light used as the repulsive barrier in our plugged quadrupole trap. In this dissertation, the beam provided by the Verdi laser is referred to as the plug beam as it is used to plug the Majorana loss region in the quadrupole trap. The Verdi laser outputs up to 6.5 W at 532-nm with a $1/e^2$ beam diameter of 2.25 mm. A chiller water cools the heatsink that the laser head is mounted on, stabilizing the output angle and alignment of the laser.

3.1.3.2 External Shutter

In addition to the manually controlled internal shutter on the plug laser, a home-built shutter is placed immediately after the output. Instead of using a commercial high intensity shutter, we modified a hard drive shutter. When current is sent through the voice coil actuator, the pivot arm with a flag attached moves, blocking the laser light [33]. Instead of using a flag to block the light, we attached a silver mirror to the pivot arm to reflect the light a beam dump. The shutter is externally controlled via the timing computer to turn the output of the laser on and off throughout the timing sequence.

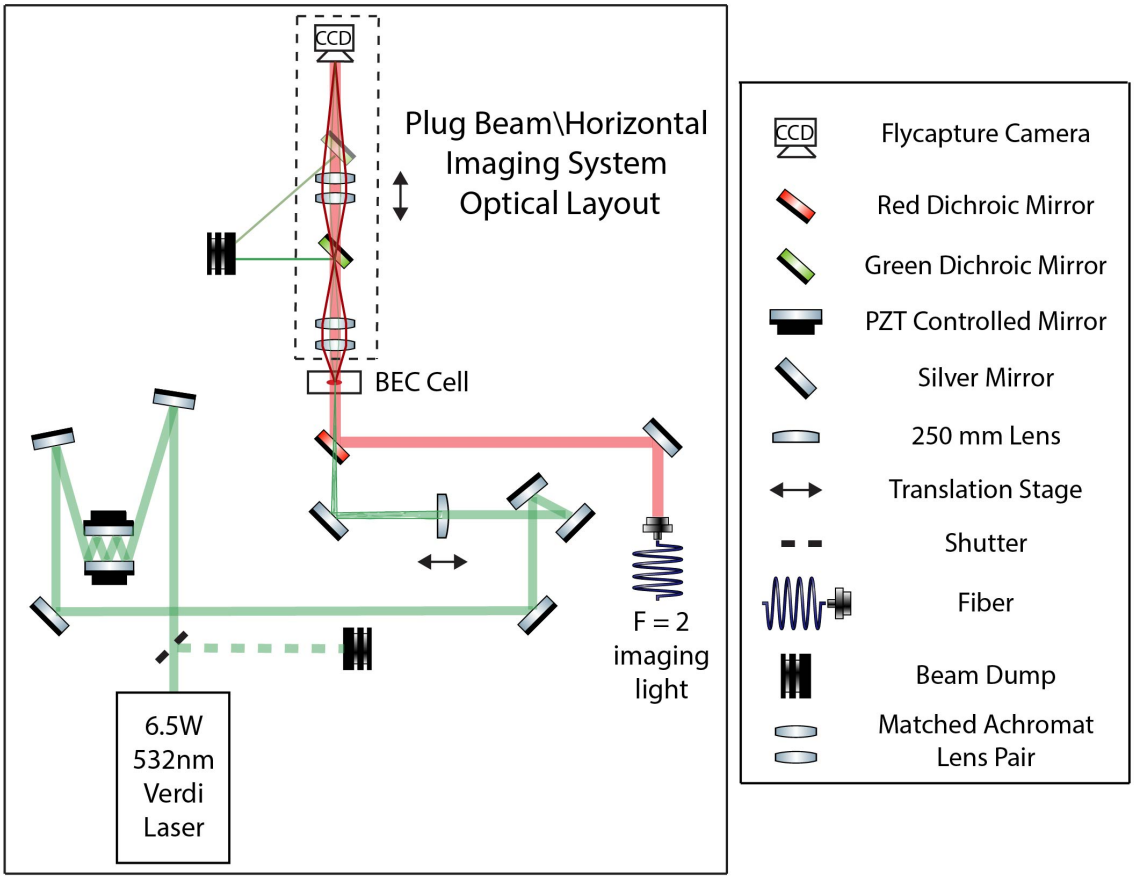

Figure 3.2: Optical layout of plug beam and horizontal imaging system.

3.1.3.3 Optical Layout

When the shutter is open, the plug beam is first reflected into a cavity comprised of two mirrors with PZT control of the horizontal and vertical angles of the mirrors. PZT control is used both for facilitating the plug alignment process and for later use in the experiment, which will be discussed in Chapter 5. The plug laser is reflected back and forth three times before emerging from the cavity. The deviation angle of the plug beam as it exits the cavity is proportional to the number of bounces in the mirror cavity, magnifying the effect of the PZT's on the angle of the plug beam. Two sets of additional mirrors are then used to align the beam to the other side of the optics table near the BEC cell. A periscope is used to increase the height of the plug beam to coincide with the height of the BEC cell. The light is then focused at the center of the BEC cell by a 250 mm focal length spherical lens as seen in Figure 3.2. At the focus of the plug beam, changes in angle from the PZT mirror cavity correspond to changes in the position of the beam.

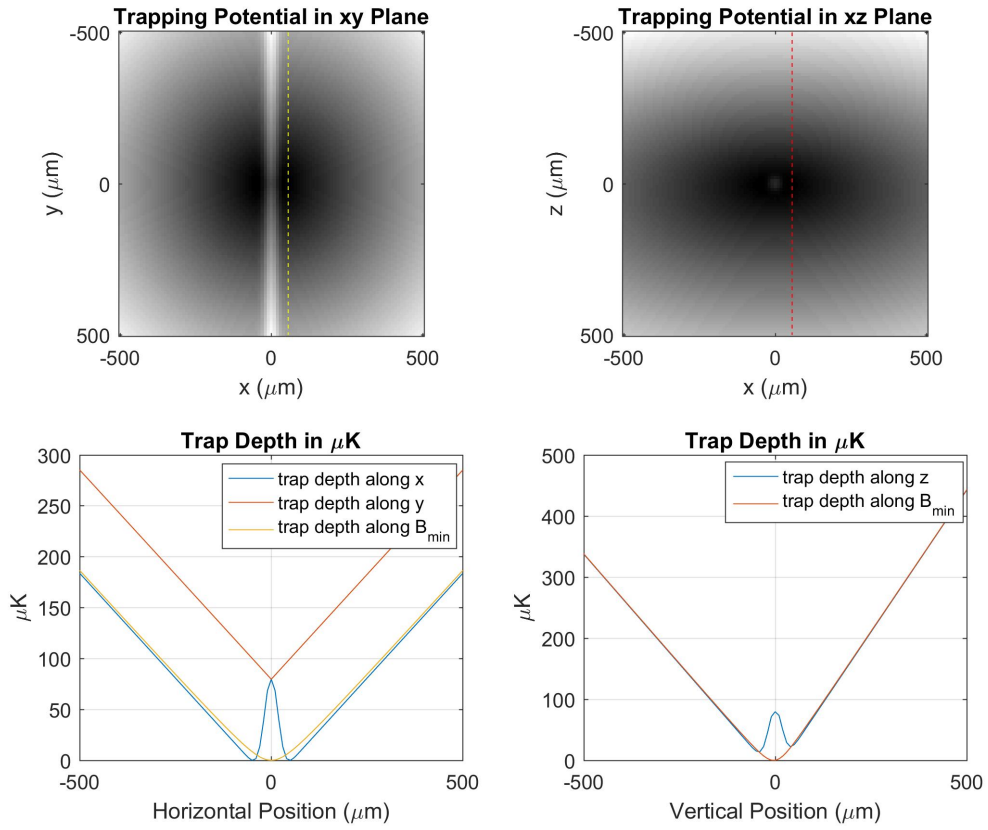

Figure 3.3: Graphs of calculated plugged quadrupole trapping potential for dB/dz = 250 G/cm and 6 W in the plug beam. The height of the repulsive barrier is calculated to be 79.6 μK. **Top left:** Trapping potential cross section in the xy plane. The yellow dotted line shows the location of the B-field minimum in the x-direction. **Bottom left:** Plot of the trap depth along x, y, and along the yellow dotted line in the above graph, corresponding to the B-field minimum. **Top right:** Trapping potential cross section in the xz plane. The red dotted line shows the location of the B-field minimum in the x-direction. **Bottom right:** Plot of the trap depth along z and along the red dotted line in the above graph corresponding to the B-field minimum.

3.1.3.4 Properties of Repulsive Barrier

The beam waist, w_0, at the focus of the 250 mm lens is calculated to be 38 μm using the following equation:

$$2\omega_0 = \left(\frac{4\lambda}{\pi}\right)\left(\frac{F}{D}\right) \tag{3.2}$$

where D is the beam diameter and F is the focal length of the focusing lens. Using the maximum intensity of the plug beam at the focus in Equation 3.1, the potential barrier height, in energy, can be calculated. As seen in Figure 3.3, the height of the repulsive barrier in a 250 G/cm trap corresponds to a temperature of 80 μK. The barrier height in temperature describes the temperature below which atoms will have low enough energies to be repelled by the potential barrier. For the plug beam parameters chosen, this potential barrier is high enough that atoms are repelled from the center of the quadrupole before they are cooled to low enough temperatures that Majorana losses become significant. Therefore the plug beam implemented provides a large enough repulsive barrier that Majorana losses are suppressed.

3.1.4 Plug Beam Alignment

As seen in Figure 3.2, the plug beam is aligned along the same axis as the horizontal imaging system, which is discussed in Chapter 4. Because the plug beam is focused at the location of the atoms which is imaged onto a CCD camera, the horizontal imaging system can be used to align the location of the focus of the plug beam to the center of the atom cloud. Two dichroic filters that pass 780 nm light but reflect 532 nm light reflect most of the plug beam power to a beam dump. However a couple μW of plug beam power reaches the CCD camera and is used for alignment of the plug beam. The plug beam can also be aligned using a Thorlabs alignment camera placed after a matched achromat lens pair that images one of the plug beam reflections off of the dichroic mirror onto the CCD camera. For the current position of the camera and lenses used to image the plug beam, pixel (361, 465) corresponds to the center of plug beam image on the alignment camera for the correct position of the plug beam relative to the quadrupole field minimum.

3.1.5 Bias Fields

Three sets of bias coils are used to translate the zero-point of the magnetic trapping potential in all three directions. Both sets of horizontal bias field coils have 50 turns and are placed 19 mm away from the center of the quadrupole trap as seen in

Figure 3.4. Because of this they provide large bias fields at relatively low currents, ∼9.8 G/A. These coils were originally designed as the AC TOP coils providing the rotating bias field for the TOP trap and have since been converted to provide static bias fields. The vertical bias field coils, not pictured in Figure 3.4 are placed on top and bottom of the shuttle 26 mm away from the center of the quadrupole coils and provide bias fields of 9 G/A. All three bias coils are controlled by analog outputs from the timing computer and are interfaced with commercial power supplies so that the current through each coil pair is easily controlled by the timing sequence.

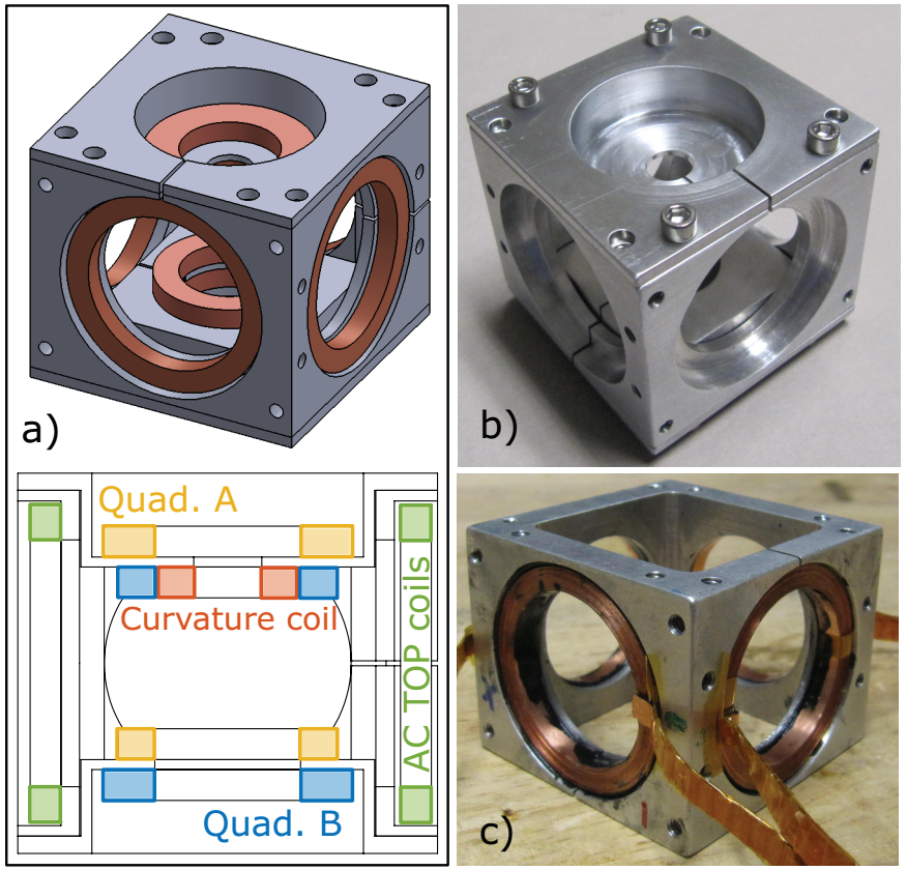

Figure 3.4: a) and d) Drawings of the center piece of the shuttle showing the various coils used in the final trap for the BEC. b) and c) Pictures of the shuttle before and after the coils have been epoxied. Currently the two sets of AC TOP coils are used bias fields for translating the center of the quadrupole field provided by the quadrupole coils shown in the Figure. A third pair of bias coils not pictured here are placed above and below the shutter to provide a vertical bias field. Image taken from reference [17].

3.2 RF Evaporation

Forced evaporative cooling is a common technique used in atomic physics experiments in which high energy atoms are selectively removed from the trap. This allows the remaining atoms to rethermalize, through elastic collisions, to a lower temperature. This process can greatly reduce the average temperature of the atom cloud and consequently, increases the phase-space density of the atoms. Two common evap-

orative cooling techniques used in atomic physics experiments are: RF evaporative cooling, which is discussed in this section, and optical evaporative cooling discussed in Section 3.5.

In RF evaporation, radio frequencies on resonance with an atomic hyperfine spin transition, are applied to induce transitions from trappable to untrappable states. The atoms that transition to untrappable states are consequently repelled from the trap and are lost. In our lab, RF frequencies are used to induce transitions from the weak-field seeking state $|F = 1, m_F = -1\rangle$ to $|F = 1, m_F = 0\rangle$ and the strong-field seeking state $|F = 1, m_F = 1\rangle$. In a plugged quadrupole trap, the magnitude of the magnetic field increases linearly away from the center of the trap, except at the location of the plug. Consequently, the Zeeman energy shift between hyperfine spin states also linearly increases away from the center of the trap. This results in a resonant RF frequency between trapped and untrapped states that is position dependent. Large RF frequencies induce spin flip transitions in high-energy atoms located on the edge of the cloud. Similarly, low RF frequencies remove less energetic atoms that are located close to the center of the trap. Evaporative cooling is then achieved by sweeping the applied RF field from high frequencies to low frequencies in discrete steps, allowing for rethermalization of the atom cloud at each frequency step.

3.2.1 RF Electronics

A programmable Agilent R4400B RF generator is used to generator RF frequency ramps that are pre-loaded from the computer via GPIB. The function generator seeds an Ophir 5303055 Solid-State RF Amplifier that amplifies the RF signal by $\sim +48$ dB. A minicircuits RF switch externally controlled by a TTL output from the timing computer is placed directly before the RF amplifier for switching the RF fields on and off throughout the BEC creation process. The start of the RF ramp on the function generator is also triggered by a TTL pulse from the timing computer for external control of the ramp start time. The output of the RF amplifier is connected to a pair of RF coils comprised of 2 single loops of magnet wire oriented in a helmholtz configuration. These coils provide RF fields on resonance with spin flip transitions to untrappable states for ^{87}Rb atoms trapped in the $|F = 1, m_F = -1\rangle$ state. Figure 3.5 shows a functional diagram of the RF electronic equipment described above and one of the RF coils mounted on the outside of one quadrupole coil.

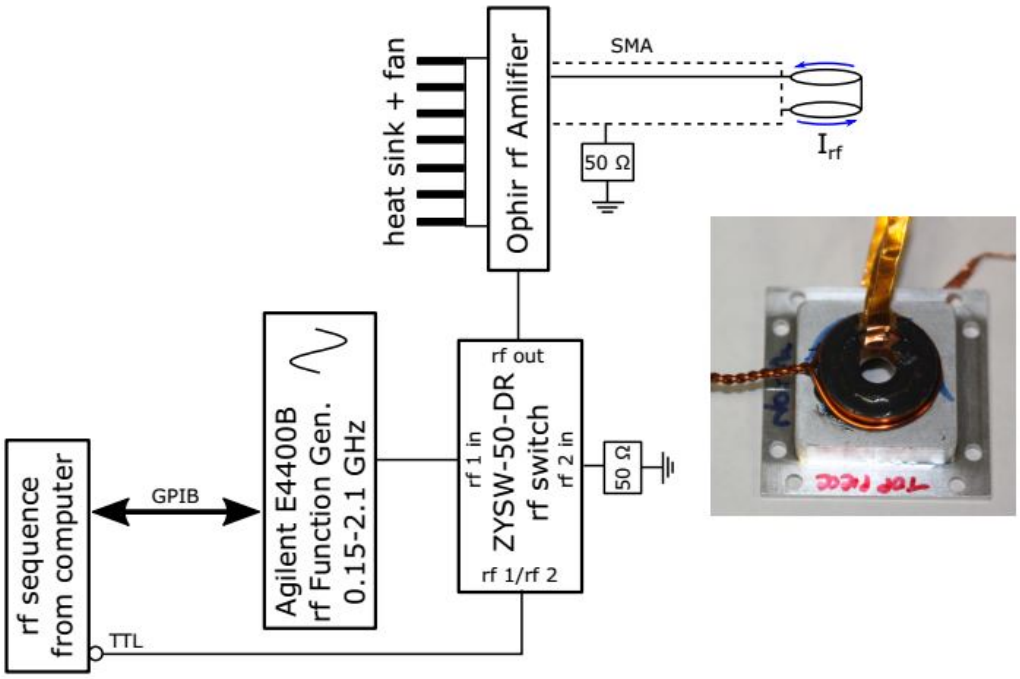

Figure 3.5: Functional diagram of RF electronics used to create RF field during evaporative cooling in the plugged quadrupole trap. Image and caption taken from reference [17].

3.2.2 RF Ramps

Immediately after atoms are transferred to the BEC cell and the quadrupole coils are ramped up to 250 G/cm, the repulsive optical barrier aligned to the center of the quadrupole trap is turned on, resulting in a plugged quadrupole trap. While the plug beam external shutter is opened, an RF field is turned on and swept from 80 MHz to 30 MHz in 2.8 s. This ramp is referred to as the High Frequency Cut as it induces spin flip transitions to untrappable states in the highest energy atoms. The purpose of this ramp is to get rid of the highest energy atoms without allowing time for rethermalization. The subsequent ramps shown in Figure 3.6 are much slower and allow atoms time to rethermalize to a lower temperature as the most energetic atoms leave the trap. The specific RF frequencies and ramp times were chosen to optimize the phase-space density at the end of the RF ramps. See Table 3.1 for information regarding the frequencies and ramp times of the specific ramps. Throughout the evaporation sequence, some atoms are lost but the density of the cloud increases

while the temperature decreases, resulting in a larger phase-space density. See Figure 3.7 for images of atoms in the plugged quadrupole trap at various stages in the evaporation sequence.

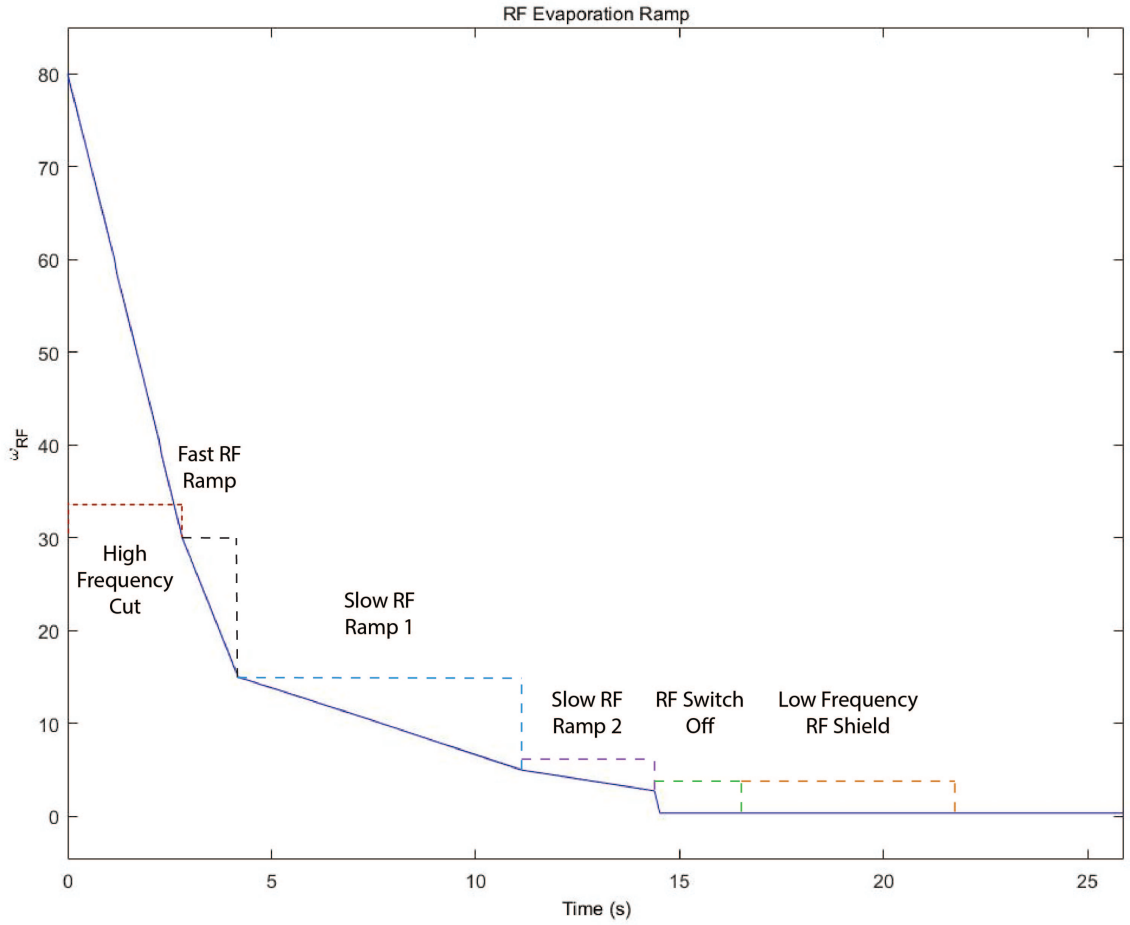

Figure 3.6: RF frequency ramps for RF evaporation in the plugged quadrupole trap.

Table 3.1: Frequencies and ramp times for RF evaporation ramps

RF Ramp	$\omega_{RFstart}$ (MHz)	ω_{RFend} (MHz)	Ramp Time (s)
High Frequency Cut	80	30	2.8
Fast RF Ramp	30	15	2
Slow RF Ramp 1	15	5	6.3
Slow RF Ramp 2	5	2.75	3.25
RF Switch Off	-	-	2
Low Frequency RF Shield	0.35	0.35	~ 6

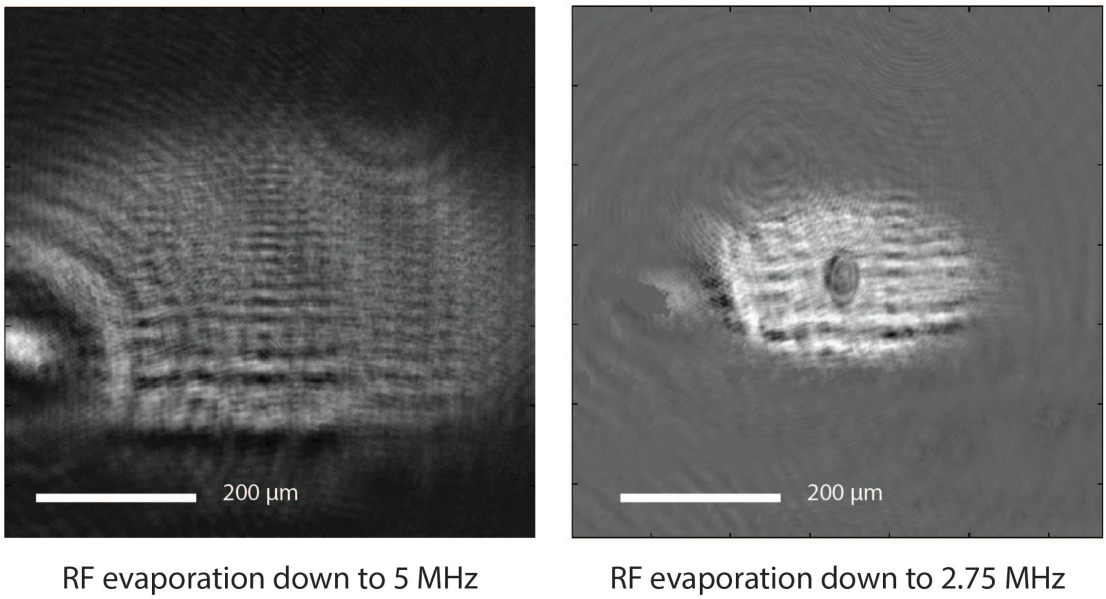

Figure 3.7: Absorption images taken with the horizontal imaging system showing the change in size of the cloud as further RF evaporation occurs. As the atom cloud is cooled through RF evaporation in the plugged quadrupole trap, the size of the cloud decreases and the density increases. This results in an overall increase phase-space density. Full width half max (FWHM) of cloud at $\omega_{RF} = 5$ MHz: FWHM$_x \sim 640$ μm and FWHM$_y \sim 250$ μm. FWHM of cloud at $\omega_{RF} = 2.75$ MHz: FWHM$_x \sim 305$ μm and FWHM$_y \sim 170$ μm.

Spin flip transitions occur in a finite region around $|\vec{B}| = 0$. Due to the finite size

of the plug beam, it is possible for spin flip transitions to occur when atoms are cold enough that they spend appreciable amounts of time near the wings of the repulsive barrier where Majorana losses are still possible. We have experimentally found that evaporation down to RF frequencies below 2.75 MHz can result in Majorana losses. It is possible to evaporate far enough in the plugged quadrupole trap for atoms to condense despite Majorana losses. However, our RF evaporation stage ends at 2.75 MHz to prevent Majorana losses. Atoms are then loaded into a hybrid optical-magnetic trap for further evaporation to condensation.

3.3 Optical Dipole Trap

As discussed in Section 3.1.2, the dipole potential for a red-detuned light field is minimized at the maximum intensity of the light field. Therefore, spatially dependent red-detuned light fields trap atoms in the most intense region of the beam. Because the potential is caused by the interaction of the light field with the induced dipole moment, this trap is referred to as the Optical Dipole Trap. There are two considerations when choosing the light source for an optical dipole trap: intensity and detuning. Even with large detunings of the optical field compared to the resonance frequency of atomic transitions, atoms can still scatter photons, resulting in heating. The scattering rate, which determines the heating rate of the atoms due to the optical field, is given below.

$$\Gamma_{sc}(\mathbf{r}) = \frac{3\pi c^2}{2\hbar {\omega_0}^3}\left(\frac{\Gamma}{\Delta}\right)^2 I(\mathbf{r}) \tag{3.3}$$

$$\Gamma_{sc}(\mathbf{r}) = \frac{\Gamma}{\Delta\hbar} U_{dip}(\mathbf{r}) \tag{3.4}$$

From Equations 3.1 and 3.3, the dipole potential energy and scattering rate depend on the intensity of the optical field and the detuning as follows: $U_{dip} \propto \frac{I}{\Delta}$ and $\Gamma_{sc} \propto \frac{I}{\Delta^2}$. From this we determine that large intensities are needed to create deep enough trapping potentials to trap atoms while large detunings are desired to minimize scattering rates and heating of atoms.

3.3.1 Trapping Laser

A Spectra Physics 30 W single-mode Ytterbium fiber laser operating in CW mode provides the optical dipole potential used to trap atoms in a hybrid optical-magnetic trap after the initial cooling stage in the plugged quadrupole trap. In order to create

BECs in a variety of trapping geometries including geometries that create quasi-2D BECs, increased confinement and trapping strength in the vertical direction is desired. We use free space beam shaping optics to create a "surfboard" shaped optical dipole potential from our trapping laser, discussed in the following section. Depending on the gradient and position of the quadrupole magnetic trap and power in the trapping laser, a variety of hybrid trapping geometries are created.

3.3.2 Trapping Laser Optical Layout

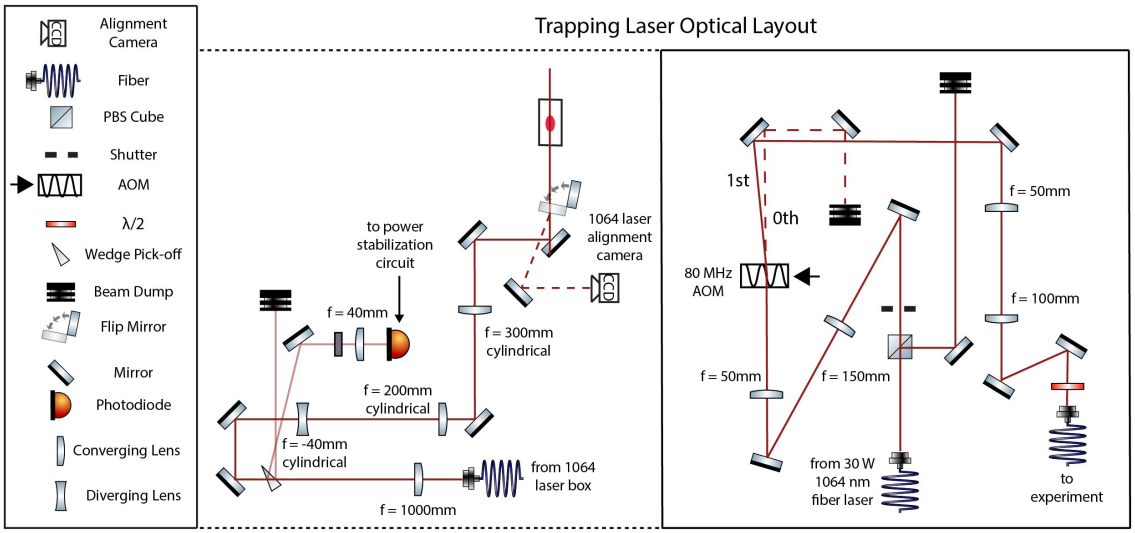

Figure 3.8: Diagram of the optical setup of the 1064-nm red-detuned trapping laser that is used to trap atoms in the hybrid optical-magnetic trap. The cylindrical lenses are oriented so that the beam is focused in the vertical direction.

The Spectra Physics trapping laser outputs 30 W of randomly polarized light. In order to clean up the polarization, a PBS cube is placed immediately after the output of the fiber laser as seen in Figure 3.8. About 15 W is rejected by the PBS cube and sent to a high powered beam dump. The remaining 15 W is sent through a spherical telescope and then to an 80 MHz AOM. The telescope is designed to decrease the beam waist by a factor of three for increased efficiency in the 1^{st} order beam from the AOM. This 1^{st} order beam is sent through additional beam shaping optics and is eventually coupled into an OZ Optics high-power optical fiber. The power of the RF signal that drives the AOM is modified to actively control the intensity of light in the 1^{st} order beam and consequently the intensity of the light out of the optical fiber.

The 0^{th} order beam from the AOM is picked off and reflected to a beam dump. All the optics described above are enclosed in a black, metal box for light suppression. The optical fiber both cleans up the transverse mode of the beam and transports the light from the 1064-nm fiber laser enclosure to the area near the BEC cell.

As seen in Figure 3.8, the output of the trapping laser optical fiber is sent through the following beam shaping optics before it reaches the BEC cell: a long focal length spherical converging lens, a cylindrical lens telescope and a final converging cylindrical lens. The 1000 mm focal length spherical lens is placed about 1000 mm away from the location of the atoms. This spherical lens is the only focusing element in the horizontal direction and therefore, most significantly effects the horizontal beam waist. With an initial beam diameter of 2.7 mm, the beam waist at the focus is calculated to be 250 μm using Equation 3.2. The following 5x cylindrical telescope increases the vertical beam waist to 6.75 mm. An increased vertical beam waist before the final lens results in a smaller vertical beam waist at the focus of the final lens. A 300 mm cylindrical focusing lens is located about 300 mm away from the atoms focusing the beam down to a calculated vertical beam waist of 30 μm at the atoms.

The actual trapping laser beam waists were experimentally measured by placing a temporary mirror in between the final focusing lens and the BEC cell to reflect the beam onto a camera located at the focus position of the trapping laser. The horizontal and vertical beam sizes were measured as the camera was translated around the focus position. After fitting the data to

$$w(z) = w_0\sqrt{1 + \left(\frac{z}{z_R}\right)^2} \tag{3.5}$$

where z_R is the Rayleigh range or distance, z, away from the focus position at which the beam radius increases to $\sqrt{2}$ of the beam waist, the following beam waists were extracted: $w_{0z} = 29.5\mu$m and $w_{0y} = 273\mu$m which correlate well with the calculated values. These beam waists correspond to an aspect ratio of 9.25:1 and can be seen in Figure 3.9. Here, we refer to z as the vertical direction, x as the direction of propagation of the trapping laser, and y as the direction perpendicular to the laser propagation direction.

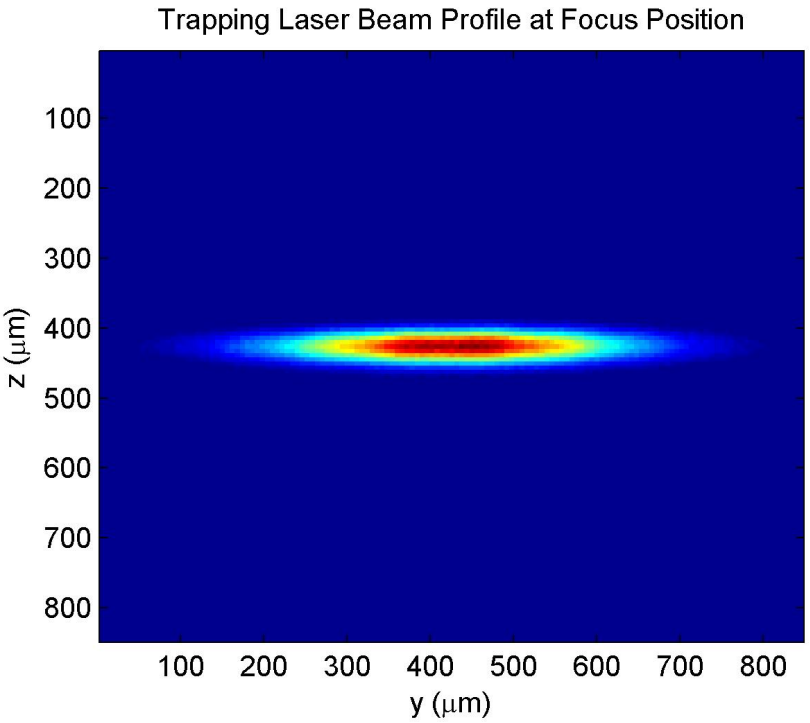

Figure 3.9: Trapping laser beam profile at the focus position. The measured beam radii are: $\omega_{0z} = 29.5\mu$m and $\omega_{0y} = 273\mu$m.

3.3.3 Trapping Laser Alignment Procedure

A flip mirror is placed immediately before the BEC cell and reflects the trapping laser onto a Flycapture alignment camera located at the focus position of the laser. The current trapping laser alignment corresponds to a beam that is centered on pixels (432, 465) on the alignment camera. For small misalignments, use the last two mirrors before the BEC cell to center the beam on the correct pixels on the alignment camera. We used a much more involved alignment procedure when first aligning the trapping position to the position of the atoms which is described below. This alignment procedure may be useful in the future if the trapping laser or flip mirror/alignment camera are greatly misalgined.

1. Align the trapping laser horizontally to be centered on the horizontal split in the shuttle on both sides of the transfer coil mount.

2. Set the height an alignment stick to the height of the center of the BEC cell. Use

the alignment stick to set the height of the trapping laser to the correct height and make sure that it is traveling parallel to the plane of the optics table.

3. After RF evaporation in the plugged quadrupole trap down to 5 MHz, ramp up the trapping laser to the maximum power level, ramp down the quadrupole gradient to less than the strength of gravity, $dB/dz < 31.7$ G/cm, and then image using the horizontal imaging system. As the gradient is decreased, the size of the cloud will increase so that the trapping laser is eventually overlapped with some of the atoms even if the trapping laser is not optimally aligned. As the gradient is decreased to less than the strength of gravity, atoms will fall out of the plugged quadrupole trap and the coldest atoms will be trapped in the optical dipole trap. An image at this state in the timing sequence will show the vertical location of the trapping laser.

4. Fine tune the vertical alignment of the trapping laser by making small changes to the vertical angle of the last mirror before the BEC cell until atoms trapped in the trapping laser are at the correct vertical location.

5. Increase the gradient as close to 250 G/cm while still trapping enough atoms to determine the location of the trapping laser.

6. After evaporation down to 5 MHz, ramp down the gradient to the value found in the last step, increase the laser power to the maximum value and then image using the vertical imaging system.

7. Change the horizontal alignment until the atoms no longer move horizontally when the laser power is ramped up. Note that it is possible to move the trapping laser in the wrong horizontal direction such that the laser is having a weaker influence on the atoms and they no longer move in the presence of the trapping laser. As a check, turn down the gradient to below the strength of gravity and make sure that at least some atoms are still trapped in the optical dipole trap.

8. Try transferring atoms to the hybrid optical-magnetic trap and evaporate close to BEC. Ramp down the strength of the quadrupole field all the way down to zero and monitor the position of the BEC using the horizontal imaging system. Change the location of the final focusing lens until the atom location, and the focus position of the trapping laser, coincide with the center of the quadrupole trap in the x-direction.

3.3.4 Trapping Laser Power Stabilization Circuit

As seen in Figure 3.3.2, a wedge located in between the spherical converging lens and cylindrical telescope reflects a small percentage of the total trapping laser power to a lens that focuses a light onto a photodiode. The voltage measured by the photodiode is proportional to the total trapping laser power and is used as an input to the power stabilization circuit for active feedback on the trapping laser power.

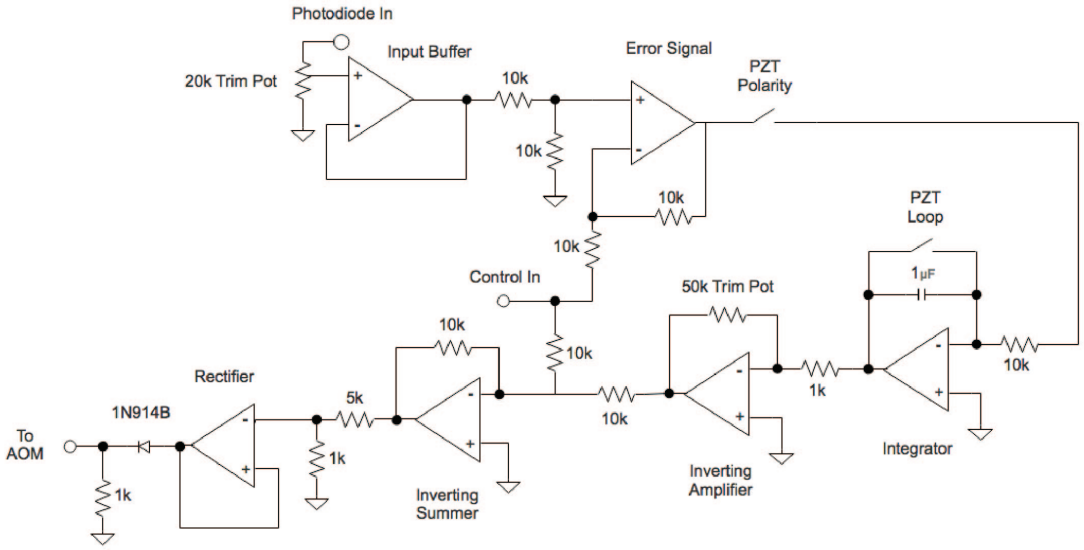

Figure 3.10: Electronics diagram of the trapping laser power stabilization circuit. The circuit is composed of an input buffer, differential amplifier, integrator, inverting amplifier, inverting summer and rectifier.

We have converted a home-built laser lockbox as the power stabilization circuit shown in Figure 3.10. There are two inputs to the circuit: the "control voltage" which is generated by the timing computer for trapping laser power control throughout the experiment and BEC creation process and the "photodiode in" voltage which is proportional to the total laser power as discussed above. The output voltage from the circuit is sent to the amplitude control of the RF signal used to drive the AOM. Changing the amplitude of the AOM drive signal changes the efficiency in the 1^{st} order beam which in turn affects the total trapping laser power.

The "photodiode in" signal is calibrated to an arbitraty voltage level by changing the potentiometer placed immediately before the input buffer shown in the circuit diagram. The calibrated photodiode signal is then subtracted from the control voltage creating an error signal. When the loop gain is enabled, the error signal is

integrated and added to the control voltage continuously until the amplitude of the AOM driving signal is increased or decreased enough to change the trapping laser power to the desired value that the calibrated photodiode signal matches the control voltage. When this happens, the error signal will be zero and the amplitude of the AOM driving signal will be constant, resulting in a constant trapping laser power, until the control voltage is changed. The voltage divider after the summer op amp divides the sum of the control in and the integrated error signal by 5 so that a control in voltage between 0 and 5 V corresponds to an output voltage of 0 and 1 V which changes the efficiency of the 1^{st} order from about 0 to 80 %. The signal is then sent through a rectifying output buffer to protect the AOM driver from having negative voltages sent to the amplitude control of the driving signal. The PZT polarity switch changes the sign of the error signal. Currently the circuit works for the PZT polarity switched to "−". The PZT loop enables or bypasses the integrator op amp chip, resulting in turning on or off the feedback loop.

A neutral density (ND) filter is placed before the photodiode to prevent the trapping laser power measured from saturating the photodiode. The power level incident on the photodiode can be changed by switching the ND filter used to attenuate the incident beam. In this way, an arbitrary power measured by the photodiode can be calibrated to an arbitrary control voltage. We have chosen ND filters and potentiometer values to give the following calibration between the total trapping laser power and the control voltage. The trapping laser power referred to here is measured immediately before the final focusing lens in the optical layout before the BEC cell. We estimate that about 88 % of that power actually reaches the atoms in the BEC cell.

3.4 Transfer to Hybrid Optical-Magnetic Trap

Following the first phase of evaporation, RF evaporation in the plugged quadrupole trap, the coldest atoms are transferred to a hybrid optical-magnetic trap and further cooled in an optical evaporation stage to BEC in a variety of different trapping geometries. One major concern in the transfer process to the hybrid trap is spin flips to other hyperfine spin states. In order for successful and uniform trapping in the hybrid trap among all atoms, they must remain in the $|F = 1, m_F = -1\rangle$ state. If atoms make a spin flip transition to $|F = 1, m_F = +1\rangle$, which is a strong-field seeking state, atoms will be lost because the optical dipole attractive force in the horizontal direction is not strong enough to counteract the repulsive force due to the quadrupole field. If atoms make a spin flip transition to $|F = 1, m_F = 0\rangle$, they would feel a trapping potential due to the optical dipole trap alone, which has a

different trapping potential than the hybrid trap. Therefore, in order to avoid loss and non-uniform trapping of the atom cloud, it is necessary to prevent spin flips during the transfer process and transfer a pure cloud of $|F = 1, m_F = -1\rangle$ atoms to the hybrid trap. For prevention of spin flips throughout the transfer process, we have experimentally determined that a minimum magnetic field of 0.75 G must be maintained throughout the transfer process at the location of the atoms.

3.4.1 Transfer to Hybrid Trap Step 1

The trapping laser is ramped up from 0 W to 4.8 W in 1 s while the vertical magnetic field gradient is constant at 250 G/cm. Horizontally, the trapping laser is centered with the plugged quadrupole trap. However, the trapping laser is vertically positioned 30 μm below the center of the plugged quadrupole which results in a magnetic field strength of 0.9 G at the the trap minimum for prevention of spin flips. The resulting calculated trapping potentials, which reflect the addition of the trapping laser to the plugged quadrupole trap, are shown in Figure 3.12. The trap depth at z = 0, the vertical location of the trapping laser, is deeper than the trap depth at z = 30 μm, the location of the B-field minimum. Therefore, atoms start to be trapped at the vertical position of the trapping laser instead of the B-field minimum as seen in Figure 3.11(b).

3.4.2 Transfer to Hybrid Trap Step 2

During this step, the vertical strength of the quadrupole is linearly ramped from 250 G/cm to 125 G/cm in 0.5 s. During this time, the vertical position of the plug and quadrupole field centers are both linearly ramped from 30μm to 60μm displaced from the trapping laser's vertical position. As the quadrupole field gradient is decreased, the effect of the magnetic field on the trapping potential decreases and the effect of the trapping laser increases. As seen in Figure 3.13, the calculated trap depth plot shows two trap minimum along x = 0 in the z-direction. The trap depth at z = 0 is greater than at z = 100 μm and as a result, more atoms will be trapped at the laser vertical trapping position. At the end of this step, the magnetic field at the trap minimum at z = 0 is 0.72 G for suppression of spin flip transitions.

3.4.3 Transfer to Hybrid Trap Step 3

The vertical magnetic field bias current is increased to further displace the magnetic field center 180 μm from the trapping laser vertical center in 0.5 s. At the same time, the vertical plug position is linearly ramped from 60 μm to 100 μm away from

the trapping laser vertical position. The plug laser external shutter is then closed, turning off the repulsive barrier. The resulting calculated trapping potential, as seen in Figure 3.14, shows a local minimum at z = 0 and a global minimum at z = 180 μm, the vertical B-field center. The trap depth of the local minimum at z = 0 is $\sim$9 μK, which is much less than the trap depth at the magnetic field center. Therefore the coldest atoms are trapped at the vertical position of the trapping laser and the hottest atoms follow the center of the magnetic trap as it is translated further away in the vertical direction from the trapping laser. From this point on, we refer to the local trapping potential minimum at the trapping laser vertical position as the hybrid optical-magnetic trapping potential. All further evaporative cooling occurs in this hybrid trap. The final trapping geometries are modified by changing the power in the trapping laser, the strength of the quadrupole field and the vertical displacement of the quadrupole field center from the trapping laser. Trapping geometries in which BECs are create in our lab are discussed in Section 3.5. Figure 3.11(c) shows atoms immediately after transfer to the hybrid trap.

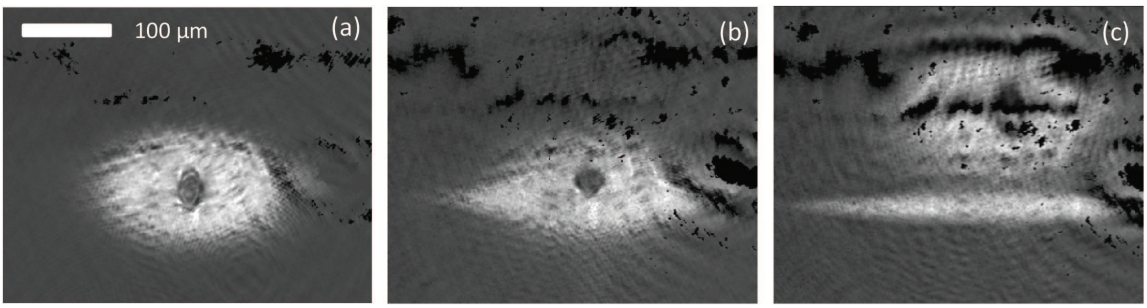

Figure 3.11: Side-view images of the cloud during different stages of transfer to the hybrid trap. (a) Image after RF evaporation down to 2.75 MHz in the plugged quadrupole trap. (b) Image after ramping up trapping laser power. (c) Image after weakening quadrupole trap to 125 G/cm and linearly ramping vertical position quadrupole trap away from axis of propagation of trapping laser. Note that the fringes and black lines are due to imperfect subtraction with the background image and diffraction patterns due to a damaged AR coating on the side of the BEC cell.

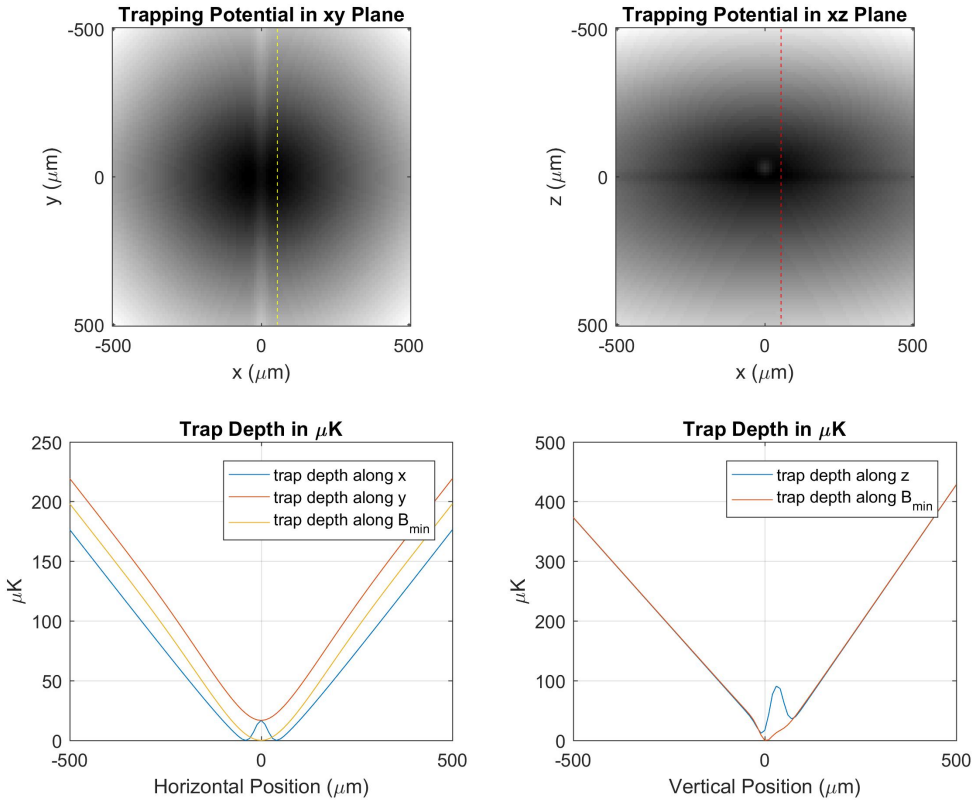

Figure 3.12: Graphs of the trapping potential at the end of the first step towards transfer to the hybrid optical-magnetic trap. Trapping potentials were calculated for dB/dz = 250 G/cm, P_{plug} = 6 W, P_{1064} = 4.8 W, and a 30μm displacement between the vertical position of the trapping laser and the the plugged quadrupole vertical position. **Top left:** Trapping potential cross section in the xy plane. The yellow dotted line shows the location of the B-field minimum in the x-direction. **Bottom left:** Plot of the trap depth along x, y, and along the yellow dotted line in the above graph, corresponding to the B-field minimum. **Top right:** Trapping potential cross section in the xz plane. The red dotted line shows the location of the B-field minimum in the x-direction. **Bottom right:** Plot of the trap depth along z and along the red dotted line in the above graph corresponding to the B-field minimum.

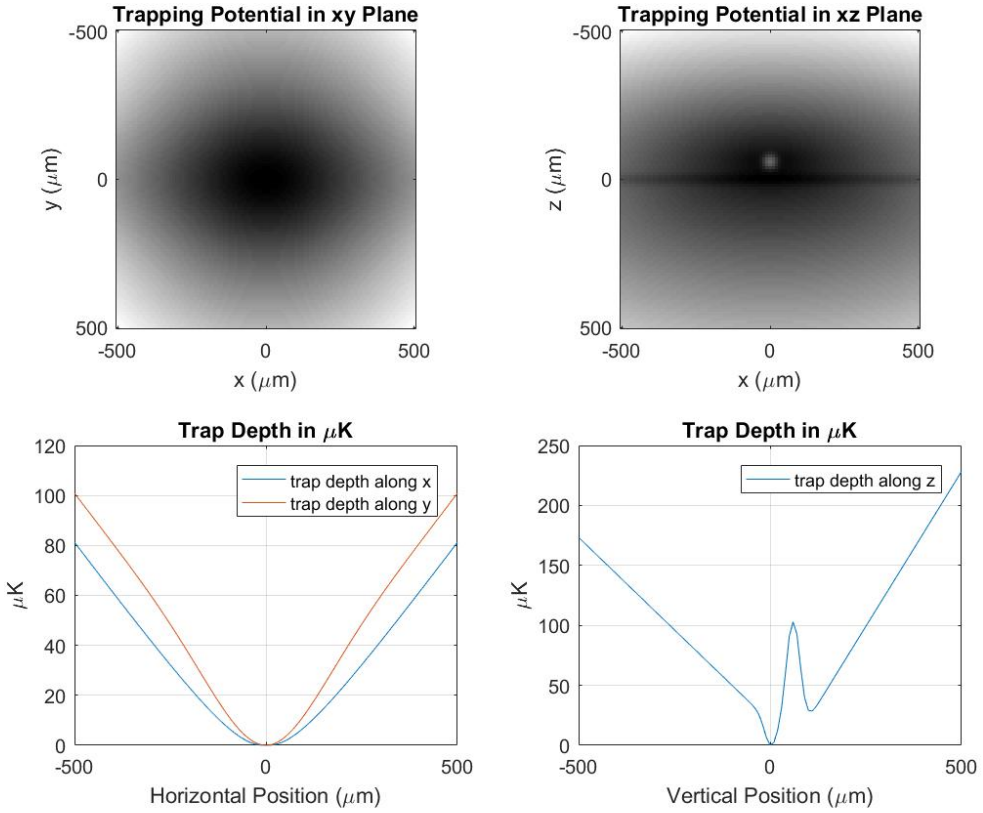

Figure 3.13: Graphs of the trapping potential after the second step of transfer to the hybrid optical-magnetic trap. Trapping potentials were calculated for dB/dz = 125 G/cm, $P_{plug} = 6$ W, $P_{1064} = 4.8$ W, and a 60μm displacement between the vertical position of the trapping laser and the the plugged quadrupole vertical position. **Top left:** Trapping potential cross section in the xy plane. **Bottom left:** Plot of the trap depth along the x and y. **Top right:** Trapping potential cross section in the xz plane. **Bottom right:** Plot of the trap depth along z.

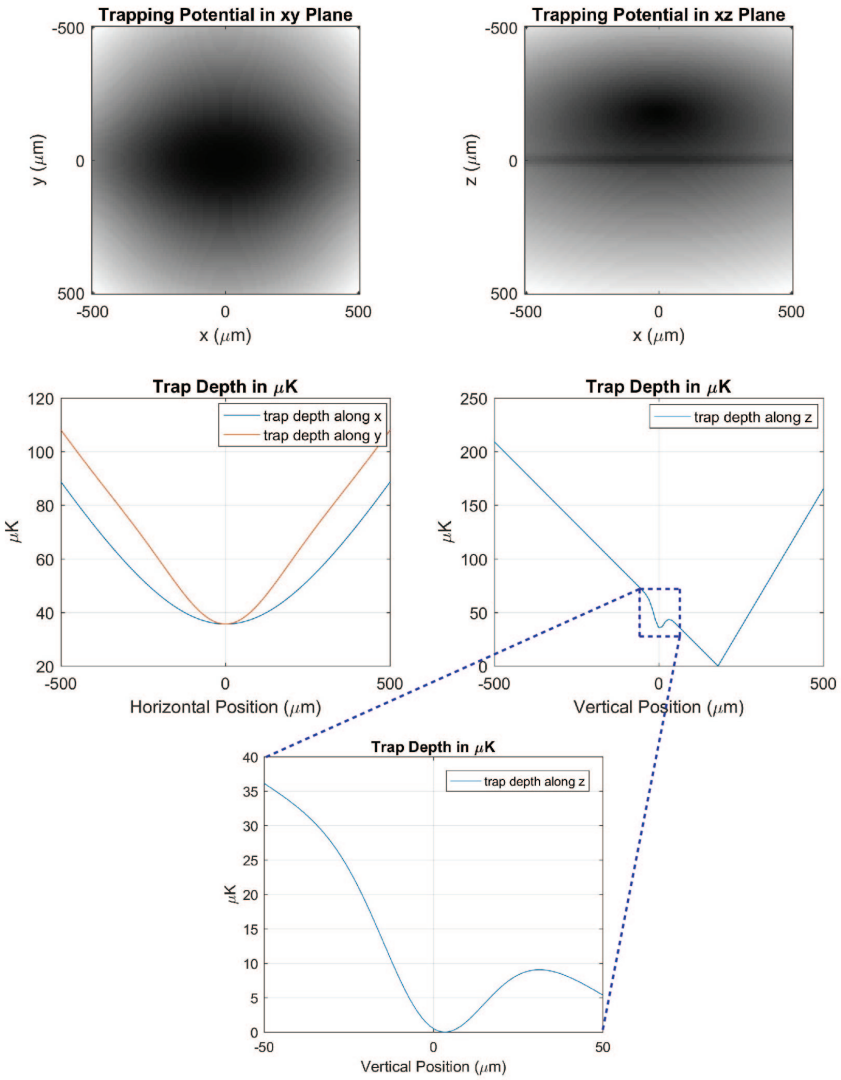

Figure 3.14: Graphs of the trapping potential after transfer to the hybrid optical-magnetic trap. Trapping potentials were calculated for dB/dz = 125 G/cm, P_{plug} = 0 W, P_{1064} = 4.8 W, and a 180μm displacement between the vertical position of the trapping laser and magnetic field center. **Top left:** Trapping potential cross section in the xy plane. **Bottom left:** Plot of the trap depth along the x and y. **Top right:** Trapping potential cross section in the xz plane. **Bottom right:** Plot of the trap depth along z. **Center:** Zoomed in plot of the trap depth in the vertical direction. The trap depth of the trap located at the position of the trapping laser is ~9μK.

Initially after atoms are transferred to the hybrid trap, some of the atoms remain at the position of the magnetic field center as seen in Figure 3.11(c). In order to prevent these atoms, which are the most highly energetic atoms, from colliding with atoms trapped in the hybrid trap at the vertical location of the trapping laser, an RF field at $\omega_{RF} = 0.35$ MHz is applied. Figure 3.15 shows RF frequencies that are on resonance with spin flip transitions to untrappable states in the hybrid trap. $\omega_{RF} = 0.35$ MHz is a small enough RF frequency that as atoms move away from the quadrupole trap center, a spin flip transition will be induced and they will be lost from the trap. However, atoms trapped in the dimple created by the dipole trap will never be on resonance with an RF frequency at 0.35 MHz. This low RF frequency is applied during all of the optical evaporation to BEC that occurs after the initial transfer to the hybrid trap and acts as an RF shield to protect atoms in the hybrid trap from interacting with the high energy atoms at the quadrupole field center.

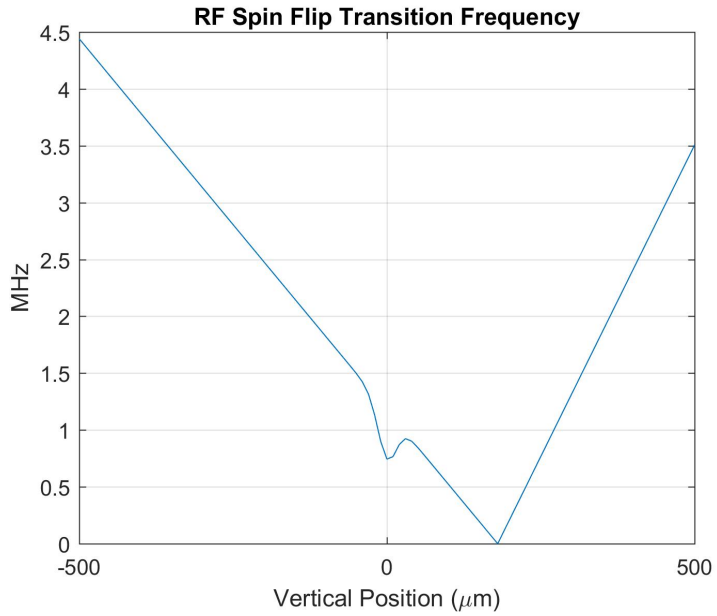

Figure 3.15: Plot of the RF spin flip transition frequencies as a function of the vertical position at the end of transfer to the hybrid optical-magnetic trap. An RF shield at 0.35 MHz is applied during optical evaporation induce spin flip transitions in highly energetic atoms located close to the center of the quadrupole field to prevent them from interacting with atoms in the hyrbid trap.

3.5 Optical Evaporation to BEC

Forced optical evaporation of the most energetic atoms is used to reduce the temperature of the atoms trapped in the hybrid trap until condensation is reached. Instead of using RF fields to induce spin flip transitions in the most energetic atoms that are then lost from the trap, the trap depth is gradually reduced by ramping down the intensity of the trapping laser. As a result, the most highly energetic atoms are lost from the trap and the remaining atoms rethermalize through elastic collisions to a lower temperature. As seen in Figure 3.14, the initial trap depth of the hybrid trap is $\sim$9 μK. This means that any atoms with higher temperatures are attracted to the lower potential position at the center of the quadrupole trap. As the intensity of the laser is reduced, the trap depth is decreased to a corresponding temperature less than 9 μK and all atoms with energies greater than the trap depth are attracted to the quadrupole center. However, all of these atoms will experience spin flip transitions when they become on resonance with the RF shield at 0.5 MHz and are then completely lost from the trap. The atoms remaining in the hybrid trap then rethermalize to a lower temperature.

3.5.1 Evaporation to BEC in the Tight Trap

The specific trapping geometry created by the hybrid trap in which condensation occurs is dependent on the quadrupole field gradient, trapping laser intensity, and vertical displacement between the trapping laser position and quadrupole field center. The simplest evaporation procedure occurs in the "tight trap" in which the trapping laser intensity is simply reduced until condensation occurs while the the other hybrid trap parameters remain constant from initial transfer to the quadrupole trap. These parameters are: dB/dz = 125 G/cm and Δz = 180 μm. Optical evaporation occurs in this trap by gradually reducing the trap depth through a series of linear trapping laser intensity ramps. The trapping laser power is initially ramped from 4.8 W to 1.9 W in the first second and is then ramped down to 1.5 W in the following second. In the next second, the power is linearly ramped from 1.5 W to 1.2 W and then from 1.2 W down to about 0.85 W in the following second. The final value that the trapping laser power is reduced to depends on the initial number of atoms and other apparatus parameters. Usually this value is in between 0.85 W and 0.95 W. After holding at the ending laser power value for 0.25 s, the laser power is ramped up to 1.2 W in 0.25 s. The laser power is always ramped up at the end of the evaporation sequence to 1.2 W so that the trapping geometry for BECs created in the tight trap is similar no matter what power the trapping laser is ramped down to in order for condensation to occur.

Side view images of the atoms in the hybrid trap during different stages of the optical evaporative cooling procedure are shown in Figure 3.16. As seen in Figure 3.18, after allowing the BEC to freely expand from the tight trap, an inverted aspect ratio is observed. This is one way that we verify that we have reached condensation. We also look for a bimodal distribution when graphing a cross-section of the image, showing a difference between the thermal atoms that have a Gaussian distribution and condensate atoms that have a parabolic density distribution. The semi-axis of the parabolic condensate density distribution in direction i is given by the Thomas-Fermi Radius, $R_{TF,i}$. Figure 3.17(a) shows a top down view of a BEC in the tight trap taken with the vertical imaging system which will be discussed in Chapter 4. The Thomas-Fermi radii are: $R_{TF,x} = 33$ μm and $R_{TF,y} = 26$ μm which correspond to about $6{\times}10^6$ atoms.

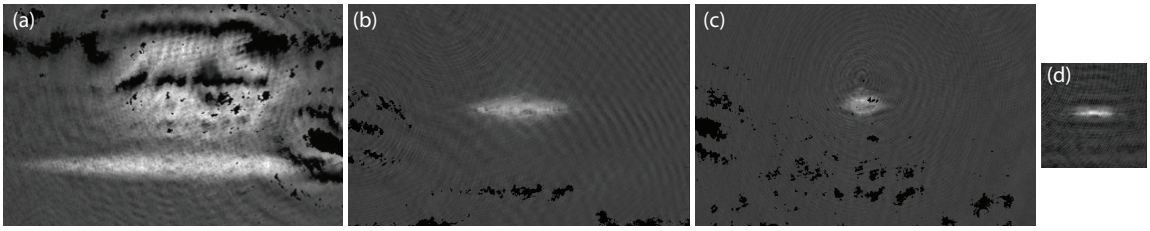

Figure 3.16: Side view images taken with the horizontal imaging system of atoms in the hybrid trap at different stages of the evaporation sequence. Images (a) - (c) are 670 μm $\times$ 350 μm and image (d) is 200 μm $\times$ 200 μm. (a) Image of atoms immediately after transfer to hybrid trap. (b) Image of atoms after first two seconds of optical evaporation. (c) Image of atoms after optical evaporation to just above T_C. Image of BEC in the tight trap. $R_{TF,x} = 36.25$ μm and $R_{TF,z} = 14.6$ μm.

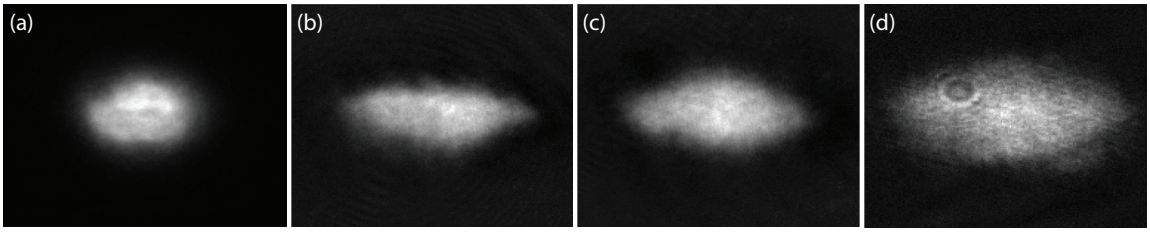

Figure 3.17: 130 μm $\times$ 130 μm top down *in situ* images of a BEC in (a) the 125 G/cm tight trap: $R_{TF,x} = 33$ μm and $R_{TF,y} = 26$ μm, (b) the 44 G/cm weak trap: $R_{TF,x} = 52$ μm and $R_{TF,y} = 23$ μm, (c) the 32 G/cm weak trap: $R_{TF,x} = 45$ μm and $R_{TF,y} = 27$ μm, and (d) the 15 G/cm weak trap: $R_{TF,x} = 74$ μm and $R_{TF,y} = 40$ μm.

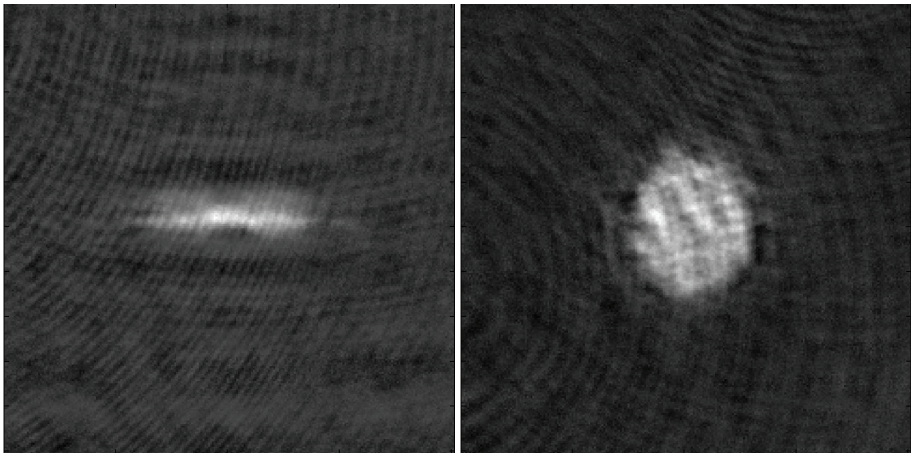

Figure 3.18: 200 μm $\times$ 200 μm side view images of a BEC in the tight trap: dB/dz = 125 G/cm, Δz = 180 μm, P_{laser} = 1.2 W. **Left**: *In situ* image. **Right**: Image after 6 ms of free expansion. The inverted aspect ratio of the condensate in expansion is evident in this image.

3.5.2 Evaporation to BEC in the 44 G/cm Weak Trap

A BEC is easily transferred from the tight trap to a weaker trap by ramping down the vertical quadrupole gradient from 125 G/cm to 44 G/cm in 0.5 s after optical evaporation down to 0.85 W in the trapping laser. The same vertical bias field that was applied in the tight trap to provide a vertical offset between the vertical position of the trapping laser and center of the quadrupole trap remains constant in the weaker trap. This results in Δz = 800 G/cm. No further optical evaporation is needed after transferring the BEC to the 44 G/cm weak trap. Some atoms are lost during the transfer process but most of them remain. Side view *in situ* and expansion images of a BEC in this trap are shown in Figure 3.19. As seen in Figure 3.17(b), the Thomas-Fermi radii are: $R_{TF,x}$ = 52 μm and $R_{TF,y}$ = 23 μm.

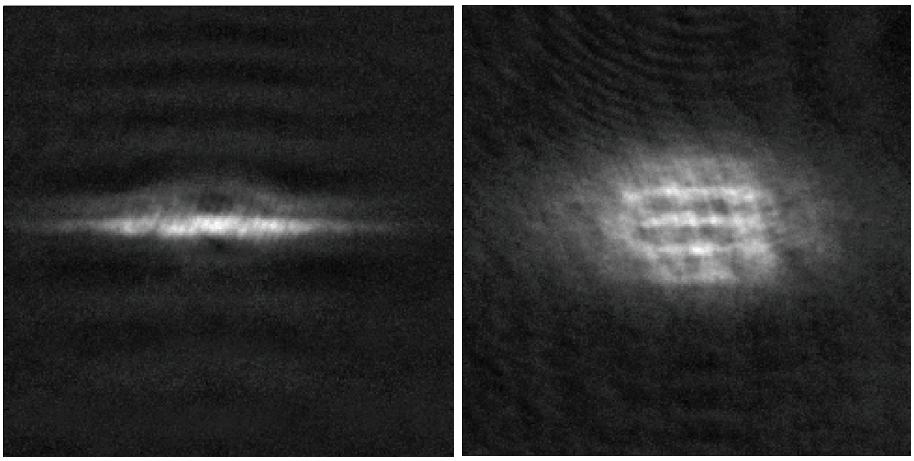

Figure 3.19: 200 μm $\times$ 200 μm side view images of a BEC in the 44 G/cm weak trap: dB/dz = 44 G/cm, Δz = 800 μm, P_{laser} = 0.85 W. **Left**: *In situ* image. **Right**: Image after 6 ms of free expansion.

3.5.3 Evaporation to BEC in the 32 G/cm Weak Trap

Atoms can be transferred from the tight trap to a 32 G/cm weak trap by linearly ramping the vertical quadrupole gradient from 125 G/cm to 32 G/cm and further reducing the trapping laser power from 0.85 W to 0.15 W in 0.5 s. With the same vertical bias field as in the tight trap, the vertical offset between the trapping laser vertical position and center of the quadrupole field in this trap is $\Delta z = 1100$ μm. Side view *in situ* and expansion images of a BEC in this trap are shown in Figure 3.20. As seen in Figure 3.17(c), the Thomas-Fermi radii are: $R_{TF,x} = 45$ μm and $R_{TF,y} = 27$ μm.

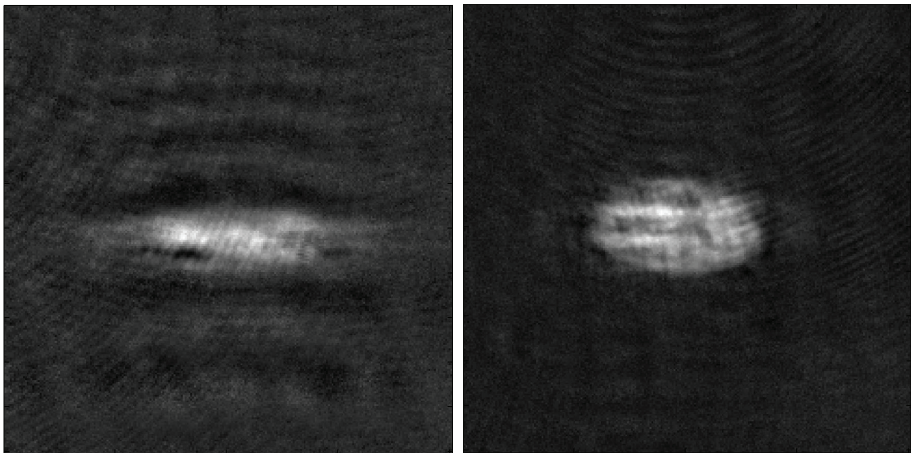

Figure 3.20: 200 μm $\times$ 200 μm side view images of a BEC in the 32 G/cm weak trap: dB/dz = 32 G/cm, Δz = 1100 μm, P_{laser} = 0.15 W. **Left**: *In situ* image. **Right**: Image after 6 ms of free expansion.

3.5.4 Evaporation to BEC in the 15 G/cm Weak Trap

Atoms are transferred from the tight trap to a 15 G/cm weak trap by linearly ramping the vertical quadrupole gradient from 125 G/cm to 15 G/cm and further reducing the trapping laser power from 0.85 W to 0.085 W in 0.5 s. After a 0.25 s hold at 0.085 W, the laser power is linearly ramped up to 0.1 V in 0.25 s. With the same vertical bias field as in the tight trap, the vertical offset between the trapping laser vertical position and center of the quadrupole field in this trap is Δz = 2.3 mm. Side view *in situ* and expansion images of a BEC in this trap are shown in Figure 3.21. As seen in Figure 3.17(d), the Thomas-Fermi radii are: $R_{TF,x}$ = 52 μm and $R_{TF,y}$ = 23 μm.

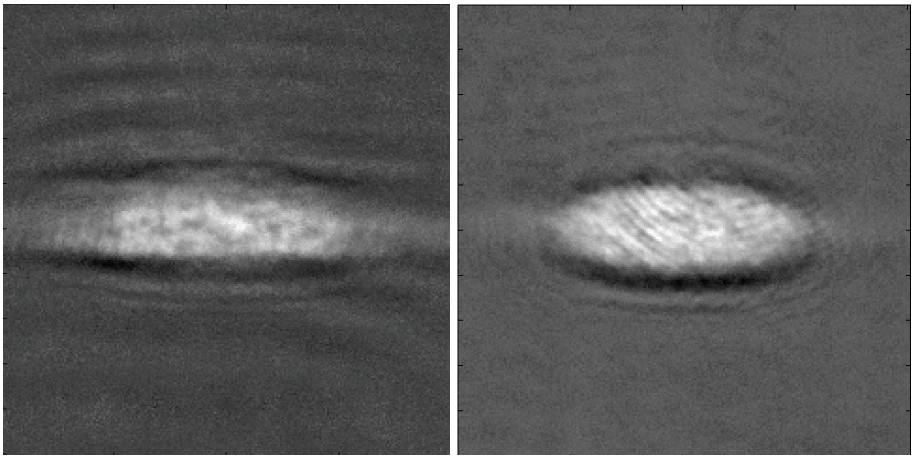

Figure 3.21: 200 μm $\times$ 200 μm side view images of a BEC in the 15 G/cm weak trap: dB/dz = 15 G/cm, Δz = 2.3 mm, P_{laser} = 0.10 W. **Left**: *In situ* image. **Right**: Image after 6 ms of free expansion.

As discussed in this section, BECs have been created in four different trapping geometries in the hybrid optical-magnetic trap. For the 2DQT experiment discussed in this dissertation, BECs are created in the tight trap.

CHAPTER 4

Imaging

One of the crucial updates made to the BEC apparatus was construction and implementation of a high magnification imaging system designed for *in situ* imaging of vortex cores in BECs. All information about condensates, such as number, temperature and density, are extracted from their images, making the imaging system an important component of the apparatus. Section 4.1 describes the light-matter interaction that leads to the different imaging methods used in our apparatus. Sections 4.2 and 4.3 describe the horizontal and vertical imaging systems respectively along with their optical layouts, example images and imaging system characteristics. Finally, a vortex imaging test is presented in Section 4.4, demonstrating the ability of the newly implemented vertical imaging system to resolve vortices in expansion.

4.1 Imaging Techniques

All information we know about BECs created in our apparatus is obtained by optical diagnostics, such as *in situ* and expansion imaging of atomic clouds. As the probe light used to image the cloud interacts with the atoms, three processes occur: absorption of photons, spontaneous emission of photons, and a phase shift of the unscattered transmitted probe light [34]. These processes are used in absorptive, fluorescence and dispersive imaging techniques respectively. In this section, near-resonant absorption and Faraday imaging techniques will be discussed as well as the light-matter interaction responsible for them.

4.1.1 Introduction to Light-matter Interactions

The interaction between light and atoms can be described by the following complex index of refraction of the atoms

$$n_{ref} = 1 + \frac{\sigma_o n \lambda}{4\pi}\left[\frac{i}{1 + 4(\Delta/\Gamma)^2 + I/I_{sat}} - \frac{2(\Delta/\Gamma)}{1 + 4(\Delta/\Gamma)^2 + I/I_{sat}}\right] \tag{4.1}$$

where σ_o is the on-resonance cross section, n is the density of atoms, λ is the wavelength of the probe light, $\Delta = \omega - \omega_o$ is the probe detuning from atomic resonance,

I is the intensity of the probe beam, Γ is the natural linewidth of the atomic transition and I_{sat} is the saturation intensity for the resonant atomic transition. With the "thin lens" approximation method described in reference [34], we assume that the atoms just attenuate and shift the phase of the incoming probe light. The phase shift acquired by the probe beam as it travels through an atomic cloud is related to the real component of the index of refraction and is given by

$$\phi = -\tilde{n}\sigma_o \left[\frac{\Delta/\Gamma}{1 + 4(\Delta/\Gamma)^2 + I/I_{sat}} \right] \tag{4.2}$$

where $\tilde{n} = \int n dz$ is the atom cloud column density integrated along the imaging axis z. Attenuation or absorption of the probe light is related to the imaginary component of the index of refraction and is given by the following equation.

$$\alpha = \frac{-\tilde{n}\sigma_o}{2} \left[\frac{1}{1 + 4(\Delta/\Gamma)^2 + I/I_{sat}} \right] \tag{4.3}$$

As a result, the electric field of the probe beam after passing through the atom cloud is given by

$$E = tE_o e^{i\phi} \tag{4.4}$$

where E_o is the electric field amplitude of the probe beam before interacting with the atom cloud and the transmission of the probe light is given by $t = e^{\alpha}$.

4.1.2 Optical Pumping

In our apparatus, atoms are magnetically trapped in the ^{87}Rb $|F = 1, m_F = -1\rangle$ ground state of the 5 $^2S_{1/2}$ level. For both near-resonant absorption imaging and Faraday imaging techniques in our apparatus, near-resonant light to the $|F = 2 \rightarrow F' = 3\rangle$ transition is sent along the imaging axis to illuminate the atoms while a pumping beam on resonance with $|F = 1 \rightarrow F' = 2\rangle$ transition illuminates the atoms in a direction perpendicular to the probe beam, pumping atoms into the F = 2 level. This optical pumping scheme is shown in Figure 4.1.

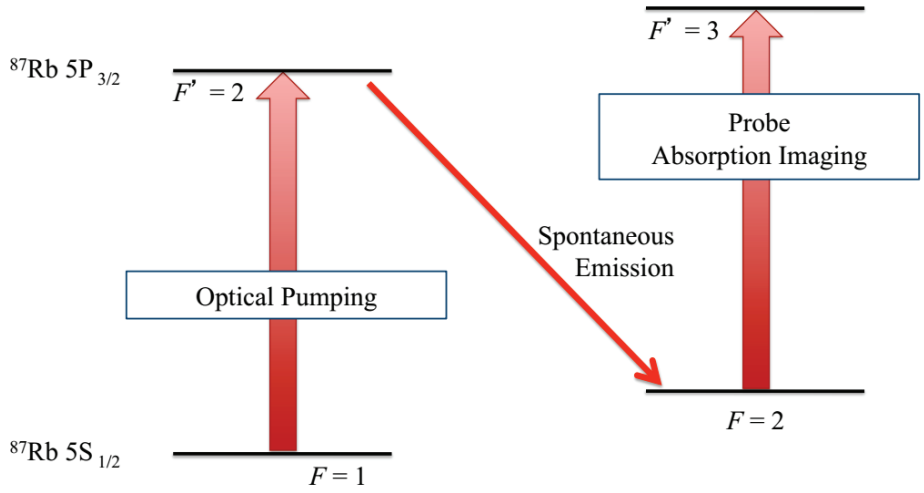

Figure 4.1: Optical pumping scheme used for transferring atoms from $5^2S_{1/2}\ |F=1\rangle$ to $5^2S_{1/2}\ |F=2\rangle$ while imaging on the $5^2S_{1/2}\ |F=2\rangle \rightarrow 5^2P_{3/2}\ |F'=3\rangle$ transition. Image and caption taken from reference [35].

4.1.3 Near-Resonant Absorption Imaging

In absorption imaging, atoms are illuminate with a laser beam close to resonance with the $|F=2 \rightarrow F'=3\rangle$ transition. The probe light is partially absorbed and attenuated by the atom cloud. The shadow cast by the atoms is imaged onto a CCD camera, and the atoms appear as a dark spot on a bright background. The optical depth, which is proportional to the integrated atom density along the imaging axis, is determined from three images: (1) Absorption image of atoms, (2) Background image of probe beam and (3) Dark frame, where no light is incident on the camera. The transmission profile of the atom cloud is extracted by those three images by the following equation

$$t(x,y) = \frac{I_{transmission} - I_{dark}}{I_{background} - I_{dark}}. \tag{4.5}$$

The optical density profile can then be extracted: $t(x,y) = e^{-OD(x,y)}$. The peak atomic density and corresponding atom number can be extracted from the optical density given the size of the atom cloud. The relevant equations are given in reference [17]. Near-resonant absorption imaging is implemented in the horizontal imaging system in our apparatus, and the implementation of this imaging method will be discussed in more detail in Section 4.2.

4.1.4 Faraday Imaging

In the presence of a magnetic field aligned along the imaging axis, σ_+ and σ_- circularly polarized light propagate with different phase shifts due to the circular birefringence of the atom cloud. As a result, linear polarized probe light, which can be decomposed into an equal superposition of σ_+ and σ_- polarized light, experiences a rotation of its initial linear polarization proportional to the atom cloud column density and external magnetic field applied due to the relative phase shift acquired between σ_+ and σ_- components of the probe beam as it travels through the atom cloud. As seen in Figure 4.2, only probe light that interacts with the BEC experiences rotation of its polarization. In our implementation of Faraday imaging, a half-wave plate placed in the imaging path is oriented such that most of the non-rotated probe light, light that does not interact with the BEC, is dumped out of a polarizing beam splitter (PBS) cube port. The signal after the PBS cube is given by $I_F = I_0 \sin^2(\theta_F)$ where I_0 is the intensity of the probe light incident on the PBS cube and θ_F is the Faraday angle of rotation of the linear polarization of the probe beam, which is dependent on the magnetic field and column density of the atoms along the imaging axis. The light transmitted through the PBS cube is then imaged onto a camera which shows a bright spot, corresponding to the condensate, on a dark background. This imaging technique is implemented in the high magnification vertical imaging system discussed in Section 4.3.

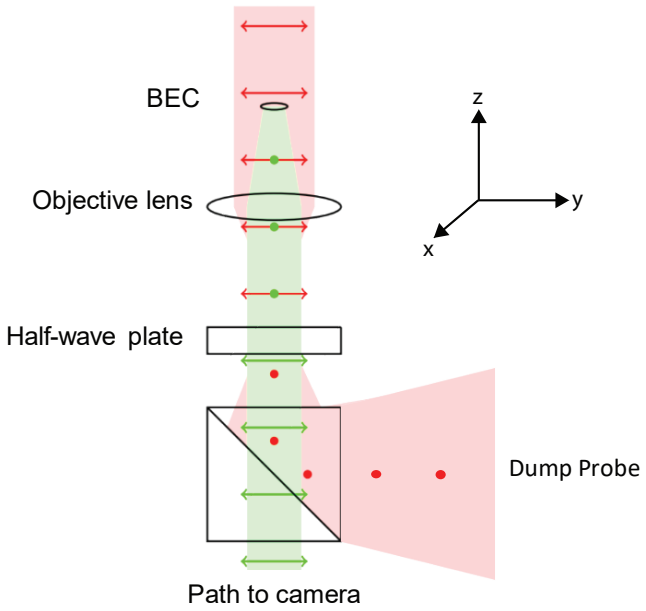

Figure 4.2: Diagram of a generic Faraday imaging system. Due to the birefringence of the BEC, the linear polarization of the probe light is rotated. The rotated component of the probe light is shown in green. The non-rotated component of the probe light that does not interact with the BEC is shown in red and is removed by the PBS cube. Image adapted from reference [35].

4.2 Horizontal Imaging System

A 7 mm diameter collimated probe beam on resonance with the $|F = 2 \rightarrow F' = 3\rangle$ transition illuminates the BEC from the side and co-propagates with the plug beam via a red dichroic mirror, as shown in Figure 4.3. The shadow in the probe beam created by the absorption of the probe light by the BEC is then imaged onto a CCD camera by two matched achromat lens pairs that give a magnification of ~4.5x. The matched achromat lens pairs and the camera are all mounted on a translation stage to facilitate the focusing of the imaging system. A green dichroic mirror and green filter are used to reflect most of the plug beam power to a beam dump to protect the camera from the high intensity plug beam light.

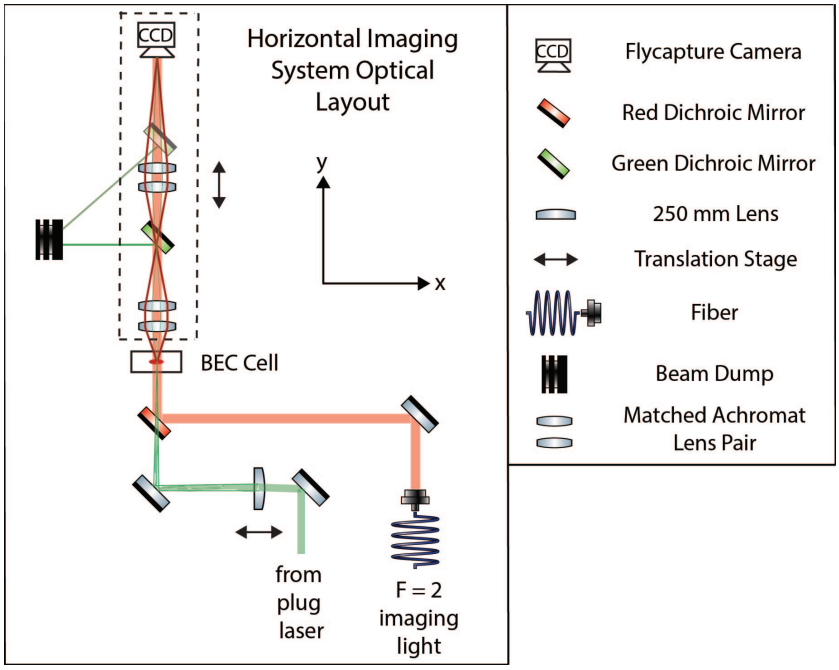

Figure 4.3: Top-down view of the optical layout of the horizontal imaging system. Collimated probe light on resonance with the $|F = 2 \rightarrow F' = 3\rangle$ transition illuminates the BEC from the side. As the light interacts with the atom cloud, some of the probe light is absorbed creating a shadow in the probe beam which is imaged onto a CCD camera. Two sets of matched achromat lens pairs are used to form a 4.5x imaging system. In this setup pumping light on resonance with the $|F = 1 \rightarrow F' = 2\rangle$ atomic transition illuminates the BEC from the top, pumping atoms into the F = 2 ground state.

50 μs before the imaging pulse, the quadrupole magnetic fields are turned off to account for the finite turn-off time of the coils, ensuring that no magnetic fields are on during the imaging pulse which would cause atoms to perceive the probe light as off-resonance due to Zeeman splitting in the presence of a magnetic field. During the 75 μs imaging pulse, repump light on resonance with the $|F = 1 \rightarrow F' = 2\rangle$ transition illuminates the BEC from the top, pumping atoms into the F = 2 ground level. At the same time, the camera is triggered by the timing sequence to capture the image as the probe light illuminates the cloud and is partially absorbed.

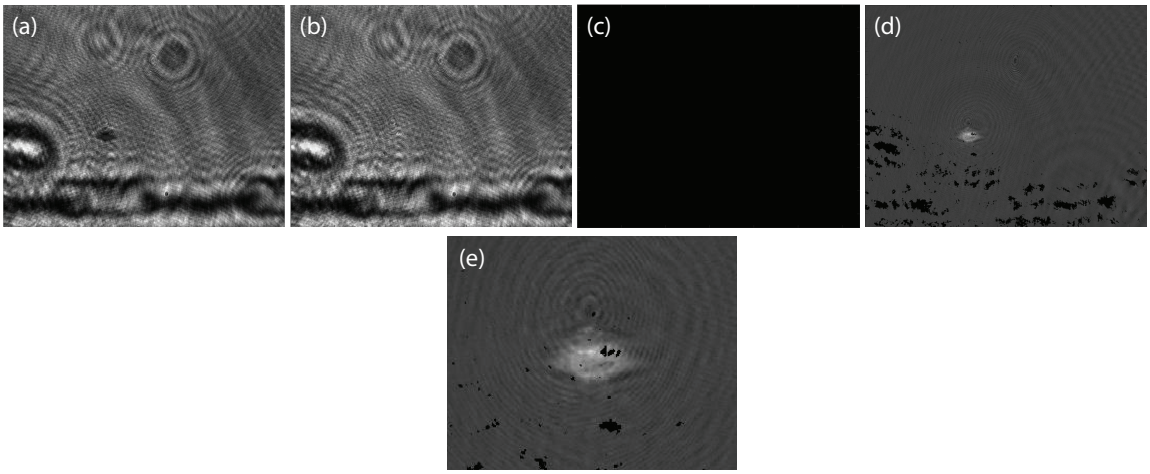

Figure 4.4: Diagram of absorption imaging process in the horizontal imaging system. (a) Absorption image of atoms. On-resonance probe light illuminates the atoms and is partially absorbed by the atoms. The transmitted light is imaged onto the camera. (b) Background image of probe light. This frame is taken to eliminate imaging artifacts such as interference fringes from dust particles on the BEC cell windows and optics and diffraction patterns from the damaged AR coating on the sides of the BEC cell. (c) Dark frame, image taken without atoms or the probe beam. This frame is subtracted from both the absorption and background frames during image processing. (d) Processed image from subtracting the absorption image from the background image. The atom cloud shows up as a bright spot on a dark background. (e) Zoomed in view of processed image. Images (a) - (d) are 1050 μm $\times$ 780 μm and image (e) is $\sim$150μm $\times$ 150μm.

As discussed in Section 4.1.3, usually three images are taken in absorption imaging: the absorption image, background image and dark frame. As shown in Figure 4.4(a), absorption images taken with the horizontal imaging system show many interference fringes from dust particles on the BEC cell windows and optics in the imaging system. The thick dark black lines in the image correspond to the diffraction pattern from a damaged AR coating on the sides of the BEC cell. In order to eliminate most of these imaging artifacts, the absorption image is subtracted from the background image. This results in a bright spot, corresponding to the atom cloud, on a dark background with most of the fringes subtracted out of the image. Figure 4.4(e) shows a zoomed in picture of BEC imaged in the horizontal imaging system. Some fringes are still evident even after image processing. Due to the presence of these fringes, the horizontal imaging system is mostly used for diagnostics

and initial optimization of the evaporation sequences. All characteristics of BECs created in our apparatus are extracted from images taken in the high magnification vertical imaging system.

4.3 Vertical Imaging System

The vertical imaging system, or vortex microscope, was designed for *in situ* imaging of vortices in BECs. A 10 mm focal length Nikon CFI Plan Fluor objective with 0.5 Numerical Aperture is used in conjunction with a 200 mm achromat tube lens to create a 20.16x vertical imaging system. Due to the low background signal level, Faraday imaging is implemented. The imaging light captured by a ProEm-HS Princeton Instruments back-illuminated electron-multiplying CCD camera which is triggered by the timing sequence during the imaging pulse. The specific ProEM camera used ultilizes the eXcelon3 technology for up to 95% quantum efficiency for near infrared wavelengths. The camera has a 1024×1024 pixel sensor with $13\ \mu\text{m} \times 13\ \mu\text{m}$ pixel size. With the given pixel size, the 20.16x magnification imaging system has the potential to resolve features greater than $1.3\ \mu$m, which corresponds to the size of two pixels in the object plane. The size of a vortex core in a BEC is given by the healing length, which is the distance over which the condensate density returns to its' bulk value in response to a localized perturbation. The healing length is given by the following equation

$$\xi = \frac{1}{\sqrt{8\pi n a}} \tag{4.6}$$

where n is the atom density in the BEC and $a \sim 5.5 \times 10^{-9}$ m is the s-wave scattering length. For typical atom densities of about $3{\times}10^{14}$ m^{-2} for BECs created in the tight trap discussed in Chapter 3, the corresponding vortex core size is $0.15\ \mu$m. Therefore, vortices in the tight trapping configuration are not resolvable *in situ*. However, these vortex cores are easily resolvable in expansion after the density has decreased which increases the size of a vortex core or a resolvable size. In the future, vortices may be resolved *in situ* with this imaging system when present in BECs with weaker radial trapping.

4.3.1 Optical Layout

As seen in Figure 4.5, a 2 mm collimated near-resonant probe beam is used to illuminate the BEC. Before reaching the BEC, the probe beam is first sent through a PBS cube that cleans up the polarization of the light eliminates any ellipticity of the polarization of beam. The probe beam is then sent through 50 mm and 100 mm

lenses in a 2x telescope configuration which increases the diameter of the probe beam to 4 mm at the location of the atoms. A PBS cube is placed in between the two lens to couple a collimated blue-detuned 660-nm laser into the system, which is focused at the location of the atoms by the 100 mm spherical lens. This focused beam provides a repulsive barrier that can be used to create vortices in a BEC as discussed in Chapter 1. The path of this beam is not shown in Figure 4.5. A half-wave plate placed immediately before the BEC cell is oriented to minimize the amount of background probe light that propagates through the imaging system. Background probe light that does not interact with the BEC diverges out of the objective lens and is dumped out of one of the ports of a PBS cube placed after the objective. Probe light that interacts with the BEC rotated by the Faraday angle which is dependent on the external magnetic field, probe beam detuning and integrated atom density of the cloud. This light is collimated out of the objective lens and the amount of transmitted light through the following PBS cube depends on the Faraday angle. Therefore, it is important to chose a magnetic field and probe beam detuning combination that yields a large Faraday imaging signal for a given condensate density. We have found that we have large Faraday imaging signals for a probe beam that is +5 Γ detuned from the atomic transition and an external magnetic field strength of 8.4 to 12.36 G at the BEC location during the imaging pulse.

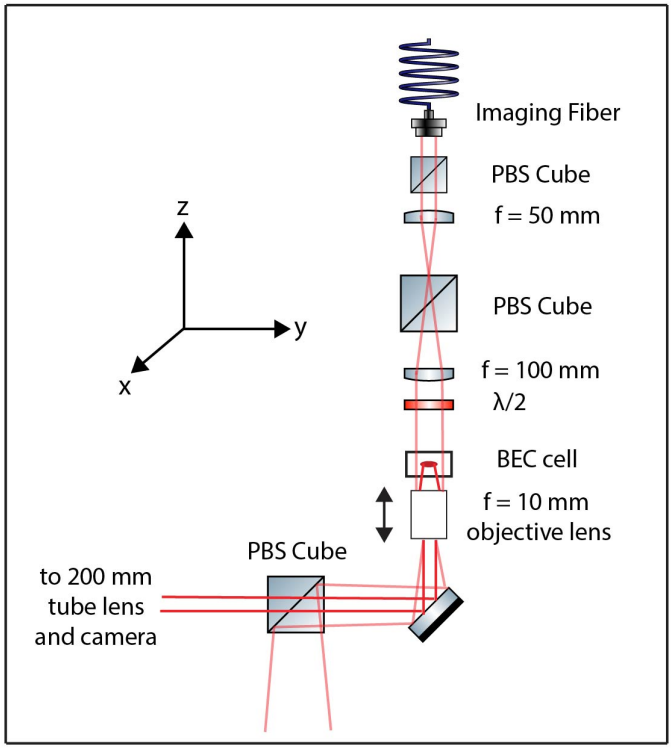

Figure 4.5: Optical layout of vertical imaging system designed for Faraday imaging. Linearly polarized collimated probe light illuminates the BEC from the top. Light that interacts with the BEC experiences a rotation of its initial linear polarization and is transmitted through the PBS cube after a further polarization rotation by the half-wave plate and is sent to a 200 mm tube lens which images the light onto a camera. Background probe light that does not interact with the BEC experiences no rotation of its linear polarization and is dumped by the PBS cube. The 10 mm focal length objective lens and 200 mm tube lens create a 20.16x vertical imaging system.

4.3.2 Imaging Sequence

During the 75 μs imaging pulse, collimated repump light illuminates the BEC from the side, pumping atoms into the F = 2 ground state. At the same time, the quadrupole field coils and the curvature coil, which provides curvature to the magnetic field, can be used to cancel the effects of gravity and provides an offset to a quadrupole magnetic field, are snapped to yield a 8.4 to 12.26 G magnetic field at the location of the atoms. Probe light +5 Γ detuned from the $|F = 2 \rightarrow F' = 3\rangle$

transition illuminates the atoms. Light rotated by the circular birefringence of the BEC is partially transmitted through the PBS cube after the objective depending on the density of the cloud and is then sent to a 200 mm achromat tube lens which focuses the light onto the ProEM camera. Because most of the background probe light is eliminated by the PBS cube, the BEC shows up as a bright spot on a dark background as seen in Figure 4.8.

4.3.3 Magnification Calibration

The magnification of the imaging system was calibrated by imaging an airforce test target of known size onto the BEC plane and measuring the size of the corresponding image captured by the ProEm camera. The airforce target followed by a 50 mm spherical lens were placed to the right of the large PBS cube shown in Figure 4.6. The target was illuminated by a probe beam from the right and was initially imaged onto a CCD camera after transmission through the PBS cube. The CCD camera was placed the same distance away from the PBS cube as the BEC plane in order to make an accurate measurement of the size of the airforce target image created at the location of the atoms. This image is shown in Figure 4.7 (a). From this image, we measured the spacing between two lines in Group 4 Element 6 to be 117.36 μm. The airforce target image at the BEC plane was then imaged with the vertical imaging system. The spacing between the lines in the same Group and Element on the airforce target was measured to be 2.366 mm as shown in Figure 4.7 (b). By dividing the the distance in image (b) by the distance in image (a), we calibrated the magnification of the imaging system to be M = 2.366/0.11736 = 20.16.

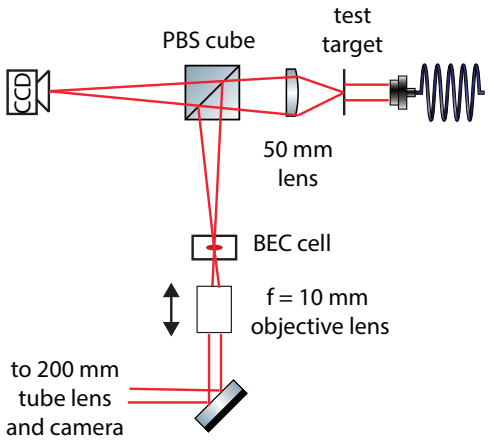

Figure 4.6: Optical layout for calibration of magnification of vertical imaging system. The test target is imaged onto the BEC plane. The size of the test target at the BEC plane is determined by imaging the same target a CCD camera placed the same distance away from the target as the BEC by the probe light that is transmitted through the PBS cube. The image of the test target at the BEC plane is then imaged by the vertical imaging system and the size of the target is measured.

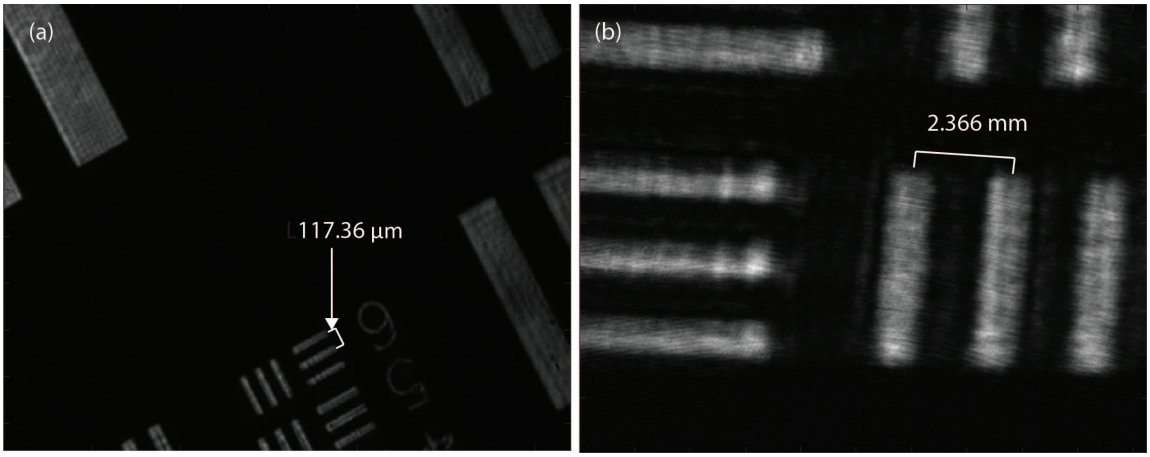

Figure 4.7: (a) Image of test target on CCD camera corresponding to image of target at BEC plane. The distance between lines in Group 4 Element 6 was measured to be 117.36 μm. (b) Image of test target at BEC plane onto ProEM camera with vertical imaging system. The distance between the same lines as in (a) was measured to be 2.366 mm. This corresponds to a calibrated magnification of M = 20.16.

4.3.4 Image Processing

Before extracting BEC characteristics, such as atom number, condensate fraction and temperature, from Faraday images, the images go through an image processing routine. Even though most of the background probe light is eliminated in Faraday imaging, the small amount that propagates to the camera necessitates background subtraction. Similar to absorption imaging, three images are taken: (1) Faraday image, (2) Background probe light image, and (3) Dark frame. The background image is subtracted from the Faraday image, resulting in a bright spot on a dark background with all background light eliminated. An example of a Faraday image after this background subtraction is shown in Figure 4.8. The background corrected Faraday image is then fit using a bimodal fitting routine that fits the condensate component to a parabolic Thomas-Fermi distribution and fits the thermal component to a Bose-Enhanced Gaussian distribution. These fits and corresponding data for a slice through the image are shown in the plot in Figure 4.8. The number of condensate atoms is extracted from the Thomas-Fermi radii using the following equation

$$N_{BEC} = \frac{\bar{l}}{15a}\left[\frac{m_{Rb}{R_{TF,i}}^2{\omega_i}^2}{\hbar\bar{\omega}}\right]^{5/2} \tag{4.7}$$

where $\bar{l} = \sqrt{\frac{\hbar}{m_{Rb}\bar{\omega}}}$ is the mean harmonic oscillator length, $\bar{\omega} = (\omega_x\omega_y\omega_z)^{1/3}$ is the geometric average of the trapping frequencies and $R_{TF,i}$ is the Thomas-Fermi radius in a given direction. After the total atom number and condensate number are extracted from fitting parameters, the condensate fraction N_{BEC}/N_{tot} is extracted. The temperature of the cloud is then calculated using the following equations

$$T = \left(1 - \frac{N_{BEC}}{N_{tot}}\right)^{1/3} T_C \tag{4.8}$$

$$T_C \approx \frac{\hbar\bar{\omega}}{k_B}\left(\frac{N_{tot}}{1.202}\right)^{1/3} \tag{4.9}$$

where T_C is the critical temperature. BEC characteristics extracted from the Faraday image shown in Figure 4.8 are: $N_{BEC} = 6.15 \times 10^6$, $N_{BEC}/N_{tot} = 0.483$, $T_C = 672\mu$K and $T = 539\mu$K.

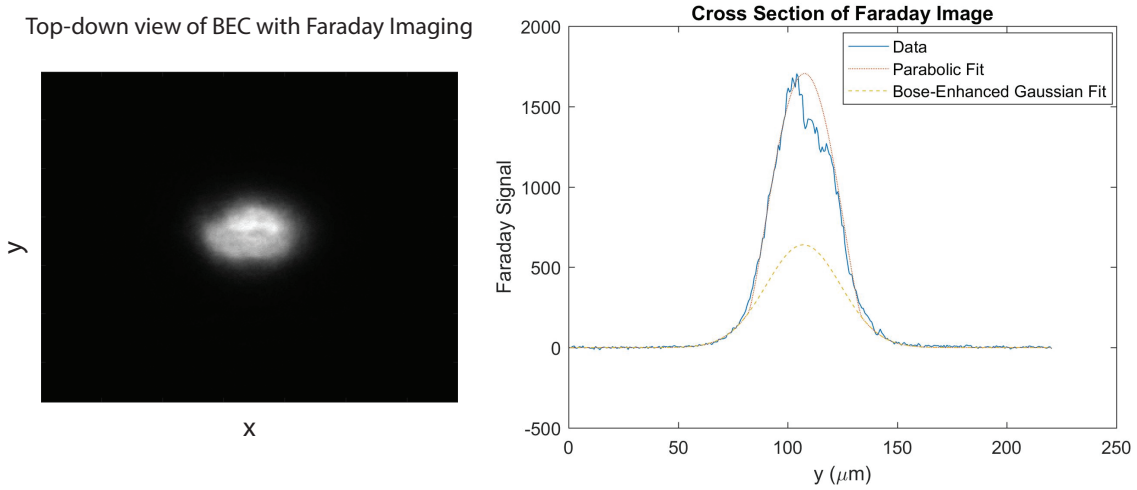

Figure 4.8: Left: 225 μm $\times$ 225 μm image of a BEC using Faraday imaging with the vertical imaging system. The slight background light that does appear on the camera is subtracted out in this image. Right: Cross section of the Faraday image along y. This plot shows the data from the image in blue, the Bose-Enhanced Gaussian fit, corresponding to the thermal component, in the yellow dashed lines and the Parabolic fit, corresponding to the condensate atoms, in the red dotted line.

4.4 Vortex Imaging Test

Before any experiments where done in the apparatus, we did a vortex imaging test to determine the necessary expansion procedure to resolve vortices created in BECs in our apparatus with a known vortex nucleation mechanism. When two BECs collide, they interfere creating solitons which eventually decay to vortices. We used this vortex nucleation mechanism to create vortices for the imaging test.

4.4.1 Vortex Nucleation

Atoms were initially optically cooled in the hybrid trap to just above T_C as shown in Figure 4.9 (a). The plug beam vertical position was then ramped to the position of the atoms, causing the thermal cloud to split into two, shown in Figure 4.9 (b). As seen in Figure 4.9 (c), further optical evaporation in the presence of the plug beam resulted in the creation of two separate BECs. In the last step of the vortex nucleation process, the plug beam vertical position was ramped away from the atoms over 100 ms allowing the BECs to collide. As the BECs collided, they formed one

BEC and vortices were resolved in expansion after a 50 ms hold time. We have not resolved solitons created by interference between the two BECs but suspect that they are present before they decay to vortices during the 50 ms hold.

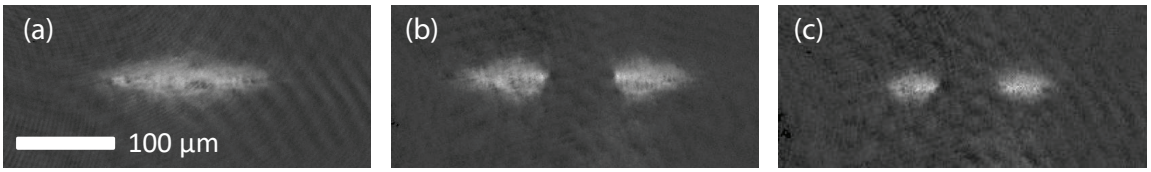

Figure 4.9: Side view absorption images of the atom cloud during various stages of the vortex nucleation process. (a) Image of atoms optically cooled to just above T_C in the hybrid trap. (b) Image after the plug beam vertical position is ramped up to split the thermal cloud into two. (c) Image after further optical evaporation in hybrid trap in the presence of the plug beam. 2 BECs are created. The plug beam vertical position is then ramped away from the atoms over 100 ms, allowing the BECs to collide.

4.4.2 Results

We found that vortices were resolvable in BECs after a combination of both radial and vertical expansion steps. Initially, the atoms undergo 6 ms of radial expansion achieved by snapping the magnetic fields, which provide most of the radial confinement, to a much weaker value while the trapping laser remains at the same value. During this step, the atoms effectively expand exclusively in the radial direction. This is followed by a 7 ms vertical expansion step during which the trapping laser power is snapped to 0 W, which results in fast vertical expansion of the atoms. Figure 4.10 shows the resulting images of BECs after 6 ms radial and 7 ms vertical expansion steps. Both images on the left show BECs after the discussed expansion procedure in which the vortex nucleation method was not used. These images are used as a reference to compare to the BEC expansion images in which the vortex nucleation methods was used. The images in Figure 4.10 clearly show that vortices are resolvable after the given expansion procedure. Therefore, we have determined that vortices can be resolved with the vertical imaging system after the correct expansion procedure from BECs in the tight trap.

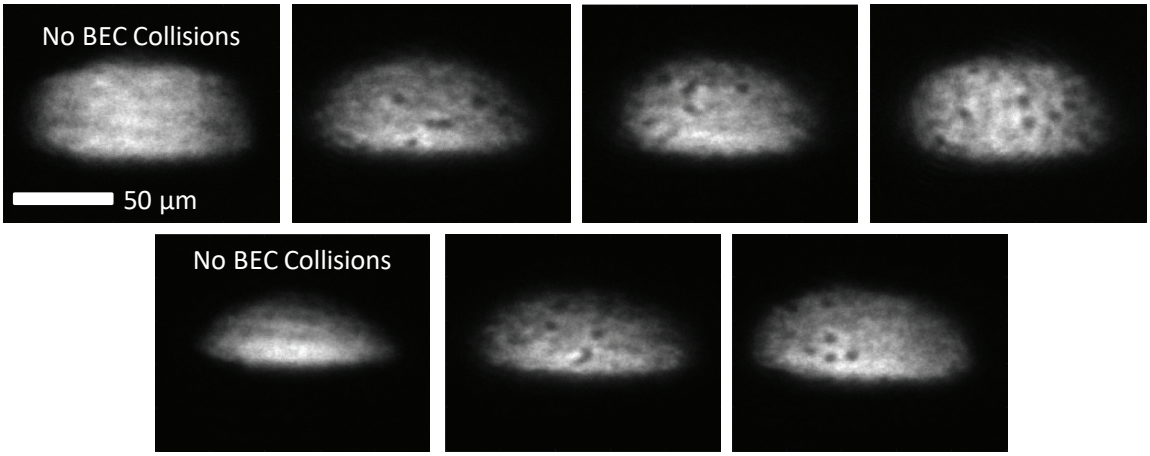

Figure 4.10: Faraday images of BECs after 6 ms radial and 7 ms vertical expansion. Images on the left show BECs that were never split and collided to create vortices. These are used as a reference to compare to the rest of the images that were taken after expansion from collided BECs. Vortices are clearly resolvable.

CHAPTER 5

Experiment

As discussed in Chapter 1, experimental studies of vortex nucleation and the onset of turbulence in a superfluid are important for achieving a deeper understanding of the overall problem of turbulence. The experiments of this chapter were aimed at investigating thermal counterflow in dilute-gas BECs as a possible vortex nucleation mechanism and method of inducing turbulence.

5.1 Introduction

One method of creating turbulence in superfluid helium is through thermal counterflow, in which the normal and superfluid components flow in opposite directions. This is achieved by applying heat to the closed end of a channel containing superfluid helium. The normal fluid component, which carries all heat and entropy in the fluid, flows away from the heater carrying heat with it while the superfluid component flows in the opposite direction to eliminate any mass flow [16]. Above a critical heat flux, the superfluid becomes turbulent which manifests in a tangle of quantize vortex lines [15]. To date, thermal counterflow turbulence has not been simulated or studied in dilute-gas BECs provoking the following research question that motivates this dissertation: *Is the onset of turbulence due to thermal counterflow unique to superfluid helium or will thermal counterflow create turbulence in dilute-gas BECs?*

Similar research questions are also motivated by a vortex nucleation mechanism previously studied in our lab. In Reference [13], vortex dipoles were created by swiping a blue-detuned laser beam used as an optical barrier through an oblate BEC. By forcing superfluid flow around the Gaussian barrier above some critical velocity, a vortex dipole is formed in the wake of the optical barrier. The critical velocity of the barrier's motion was related to the theoretical dipole activation energy, or the energy needed to create a vortex dipole in a 2D BEC [18]. Some interesting questions motivated by this experiment follow: *Would vortex dipoles be created if the repulsive optical barrier was replaced with some other barrier, such as an atom with kinetic energy comparable to the dipole activation energy? Moreover, if a cloud of high-kinetic energy thermal atoms was sent through a BEC, would vortices be created?*

This chapter presents the first experiments, to our knowledge, on high-energy thermal counterflow in 2D and 3D dilute-gas BECs. In these experiments, we collide a high-kinetic energy thermal cloud with a stationary BEC to create counterflow between the condensate and thermal atoms. However, due to the prevalence of atom-atom collisions in a gas of thermal and condensate atoms, the effect of collisions in this experiment must be considered: *What are the role of collisions in heating and atom loss? How would collisions between the high kinetic energy thermal cloud and the condensate atoms affect the onset of turbulence in the condensate? What is the dominant scattering process in dilute-gas BEC thermal counterflow?*

This chapter discusses initial measurements aimed at understanding thermal counterflow in dilute-gas BECs. Section 5.2 describes the experimental process for inducing thermal counterfow in our BECs. In Section 5.3, initial thermal counterflow data is presented including images of BECs and calculated heating and loss rates. An analysis of the data follows in Section 5.4. Section 5.5 offers conclusions of the thermal counterflow experiment and answers the research questions presented at the beginning of this chapter.

5.2 Experimental Details

This section describes technical details of our experimental procedure including experimental considerations for achieving thermal counterflow in dilute-gas BECs, the procedure for splitting and preparing two separated atom clouds, optical evaporation to BEC with a spatially separated ancillary thermal cloud and collisions between the ancillary thermal cloud and BEC. In preparation for the thermal counterflow experiment, a thermal cloud is initially transferred from the plugged quadrupole trap to the hybrid optical-magnetic trap. For detailed information regarding the transfer process, see Chapter 3. The hybrid trap is composed of a 1064-nm trapping laser operating at 5 W and a magnetic quadrupole field with dB/dz = 125 G/cm. The trapping laser is aligned down the x-axis of the BEC cell in the x-direction as is focused at the location of the atoms with the following parameters: $w_{0z} = 29.5\mu$m, $w_{0y} = 273\mu$m and $z_R = 2.6$ mm, which results in a "surfboard" shaped trapping geometry. The |B| = 0 point of the quadrupole field is positioned 180 μm above the trapping laser position. The calculated trapping potentials in this initial hybrid trap are shown in Figure 5.1a. After loading atoms into the trap, atoms undergo an initial stage of optical evaporative cooling in which the laser power is linearly ramped from 4.8 W to 1.9 W in the first second and then linearly ramped down to 1.5 W in the following second. As the power of the trapping laser is decreased, the height of the trapping potential in the vertical direction decreases, allowing the most energetic

atoms to escape and the remaining atoms to rethermalize at a lower temperature. For more information regarding optical evaporation, see Chapter 3. After the first stage of optical evaporative cooling, the atoms are cooled to just above T_c.

In order for thermal counterflow to be realized in a dilute-gas BEC, we want our apparatus to have the following capabilities: First, we desired the ability to create two clouds or split one cloud into two. Second, we wanted the ability to cool the two clouds to different temperatures: one to below T_c, in order for a significant fraction of atoms to condense, and one to above T_c; we refer to this cloud as the ancillary cloud. And lastly, the ancillary cloud should be given a variable amount of kinetic energy so that we can study collision energies above and below the dipole activation energy in the BEC. Our apparatus utilizes a blue-detuned plug beam in conjunction with horizontal bias fields to achieve the capabilities discussed above.

The 532-nm plug beam that initially creates a repulsive optical barrier for the plugged quadrupole trap is used to split the cloud in the hybrid trap into two. For more information regarding the plug laser and optical setup, see Chapter 3. The plug beam setup utilizes a mirror with PZTs for precise control of both the horizontal and vertical positions of the focused plug beam via the timing computer. After the first stage of optical evaporation, the external plug beam shutter is opened and the vertical position of the beam is linearly ramped from 100 μm to 0 μm displaced from the horizontal propagation axis of the trapping laser. The barrier height of the plug beam is large enough to completely separate the cloud into two in the x-direction as seen in Figure 5.1b. The two clouds are located at the two trap minima in the x-direction: the potential minimum on the left side of the plug beam in the figure holds the BEC, or the target cloud, and the ancillary thermal cloud is held in the potential minimum on the right.

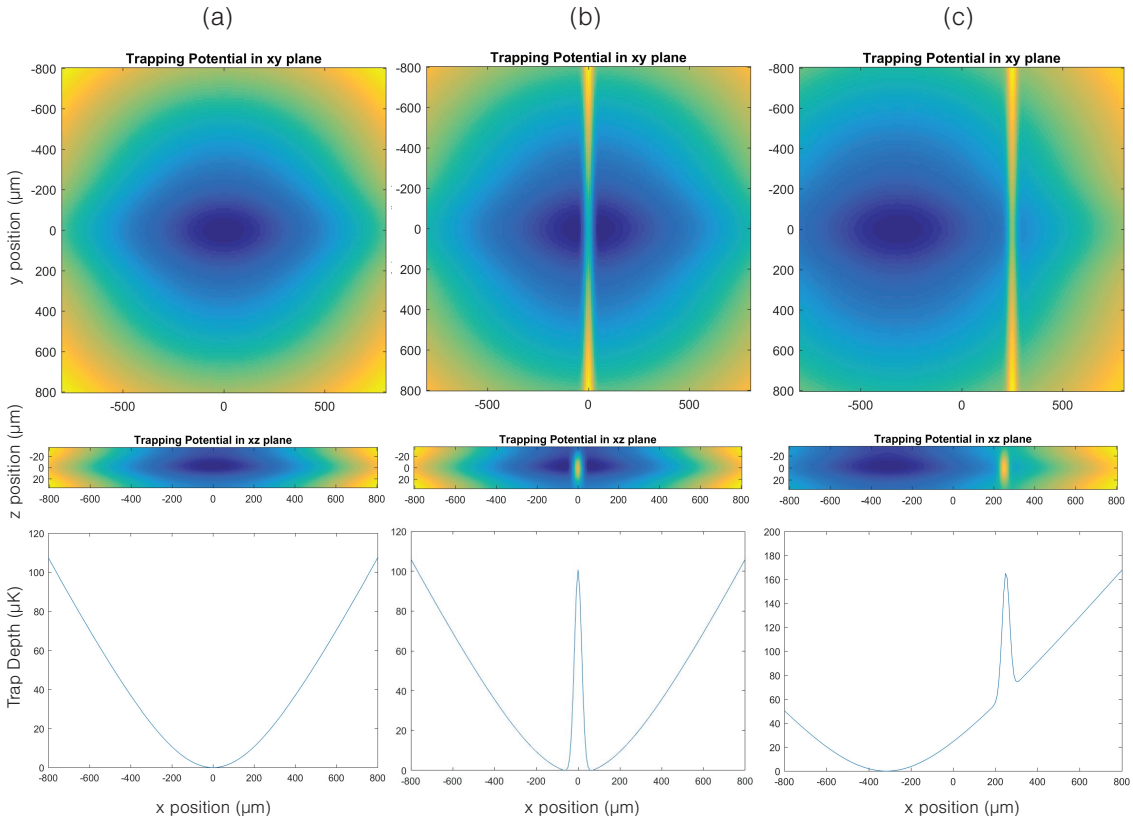

Figure 5.1: Calculated trapping potentials for different stages in experimental procedure. The top row images give the trapping potential in the xy plane, the middle row shows the trapping potential in the xz plane and the bottom row shows the trap depth along the x-axis. Note that in each plot, 0 corresponds to the initial hybrid trap minimum position. (a) Calculated trapping potentials in the combined optical-magnetic trap. This trapping geometry results in a single cloud located at the center of the trap. (b) Calculated trapping potentials after the plug beam is ramped up to the center location of the hybrid trap in both x- and y-directions. In the presence of the plug, the cloud is split into two in the x-direction. (c) Calculated trapping potentials with the plug beam horizontally offset 260μm from the initial hybrid trap minimum and a horizontal bias field resulting in a 300 μm horizontal shift of the hybrid trap minimum in the x-direction. As the plug beam horizontal position and hybrid trap horizontal position are linearly ramped away from their initial positions, the two clouds are separated by the same amount. Note that the horizontal bias field and corresponding horizontal shift of the hybrid trap minimum is determined by the desired kinetic energy of the ancillary cloud. As soon as the repulsive barrier is turned off, the ancillary cloud travels towards the hybrid trap minimum and its initial potential energy is fully converted to kinetic energy as it collides with the target cloud.

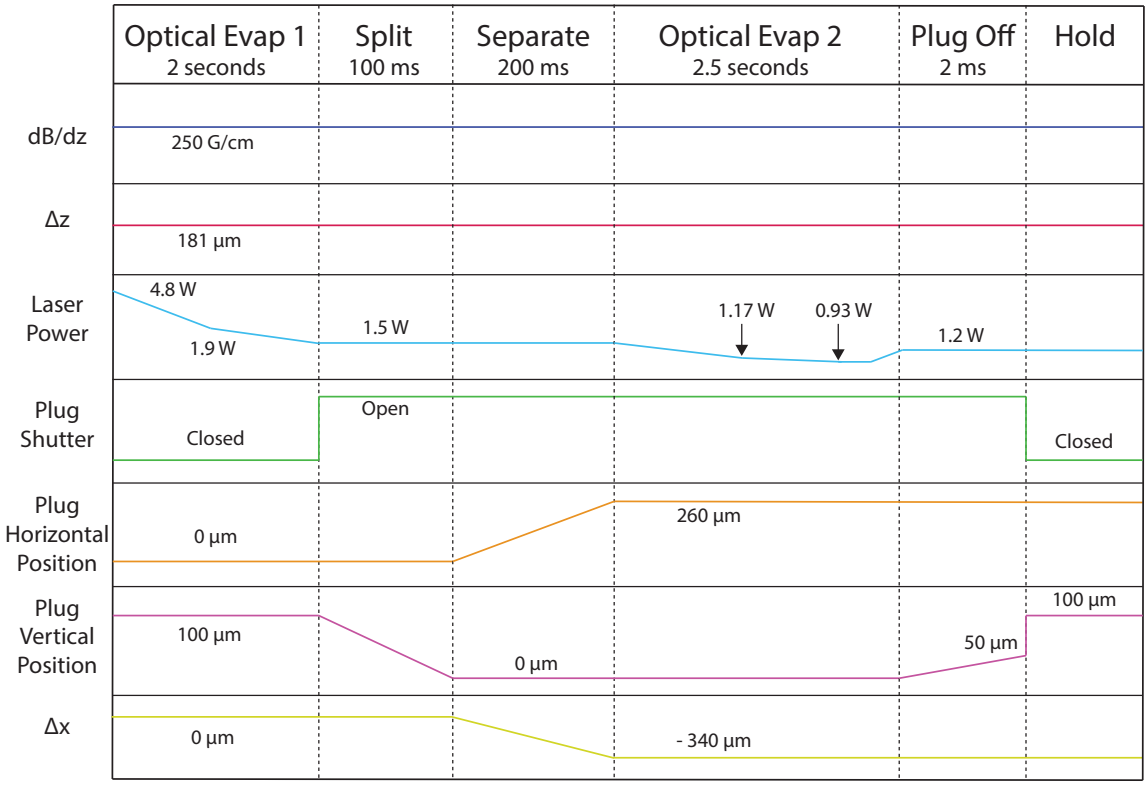

Figure 5.2: Experimental procedure for creating a condensate and an ancillary cloud with a variable amount of kinetic energy. The sequence starts immediately after transfer to the hybrid optical-magnetic trap and includes evaporative cooling, splitting and separation of the two clouds and collisions between the target and ancillary clouds. Δz refers to the displacement of the vertical position of the magnetic trap from the trapping laser propagation axis and Δx refers to the horizontal displacement of the hybrid trap minimum from its initial position through horizontal translation of the magnetic field. This specific sequence gives a BEC and an ancillary cloud separated by 600 μm.

Through a combination of moving the repulsive barrier and ramping up a horizontal bias field in the x-direction, the ancillary cloud is displaced from the harmonic trap center, increasing the potential energy of the cloud by a variable amount corresponding to the displacement from the trap center. The horizontal position of the repulsive barrier in the x-direction is ramped to the right of the hybrid trap initial center position by 260 μm while a horizontal bias field oriented in the x-direction is linearly increased to move the center of the hybrid trap to the left (further away

from the repulsive barrier) by a variable amount. As the horizontal position of the repulsive barrier is moved to the right, the ancillary cloud is moved with it. Similarly, as the horizontal bias field is ramped up, the condensate moves as the hybrid trap center is translated. The resulting calculated trapping potentials are shown in Figure 5.1c. As the ancillary cloud is further displaced from the trap center, its potential energy increases. In this way, the cloud can be given a variable amount of energy by controlling the displacement distance through the plug beam position and horizontal bias field value.

In the vortex dipole experiment discussed in Section 5.1, a vortex dipole pair is created once the blue-detuned beam is swept through the oblate BEC above a critical velocity, which was related to the dipole activation energy. The energy needed to create a vortex dipole pair in a 2D condensate is given by

$$E_{pair} \simeq \frac{2\pi\hbar^2 n_{2D}}{m}\ln(d/\xi) \tag{5.1}$$

where n_{2D} is the 2D density, or number of atoms per area, d is the separation between the vortices in the dipole and ξ is the healing length of the condensate, or approximate size of a vortex core. In order to determine how far the ancillary cloud needs to be displaced from the center of the harmonic trap, the vortex pair energy is equated to the potential energy in a harmonic trap given by the following equation.

$$PE = \frac{1}{2}m{\omega_x}^2x^2 = E_{pair} \simeq \frac{2\pi\hbar^2 n_{2D}}{m}\ln(d/\xi) \tag{5.2}$$

Solving for the distance away from the center of the harmonic trap yields the following equation.

$$x = \sqrt{\frac{2E_{pair}}{m{\omega_x}^2}} = \frac{2\hbar}{m\omega_x}\sqrt{\pi\ln(d/\xi)n_{2D}} \tag{5.3}$$

For $n_{2D} = 1.65\times10^{15}$ m^{-2}, $\omega_x = 2\pi\times$(33 Hz) and $d = 4\xi$, the calculated distance that corresponds to the dipole activation energy is $\sim$600μm. Therefore 840 μm, 600 μm, 400 μm, 260 μm and 165 μm were chosen as the initial separations between ancillary and target clouds to allow tests of thermal counterflow at energys at, above and below the 2D dipole activation energy. For all the separations, except for 165 μm, the plug beam position is horizontally translated to move the ancillary cloud to the right by 260 μm. In the case of the smallest separation, the ancillary cloud is only translated 165μm to the right. For separations 840 μm, 600 μm and 400 μm, the hybrid trap center is translated to the left by 580 μm, 340 μm and 140 μm respectively to give the desired separations.

After the plug position and trap center are translated, separating the two clouds

by the desired amount, a second evaporative cooling stage is used to cool the left cloud to condensation. In order to cool the two clouds to different temperatures, we exploit the position dependence of the vertical trap depth. We changed the position of the final trapping laser focusing lens until the focus position coincided with the translated position of the ancillary cloud. This resulted in a higher trap depth at the ancillary cloud near the focus position and lower trap depth at the position of the condensate cloud. In this way, evaporative cooling occurred in the left cloud until a significant fraction of atoms condensed while the trap depth at the location of the ancillary cloud was large enough that atoms were not evaporatively cooled. This resulted in a condensate target cloud and an ancillary thermal cloud. In order to reach condensation in the left cloud, the trapping laser power was linearly ramped down to 1.17 W in the first second and was then down to a power in between 0.9 W and 1.1 W, depending on the distance between the condensate and the trapping laser focus position. After the second laser power ramp, the power is held constant for 0.25 s to allow for rethermalization and is then ramped back up to 1.2 W in the final 0.25 s of the evaporation stage. The final ramp up to 1.2 W ensures that no matter what power the laser is ramped down to for condensation to occur, collisions are studied in nearly the same trapping geometry.

Finally, the repulsive barrier vertical position is linearly ramped from 0 μm to 50 μm away from the hybrid trap center in 2 ms. At this distance, the barrier is far enough away from the ancillary cloud that the atoms are no longer influenced by it and start to move towards the hybrid trap center. In the next step, the plug beam is fully turned off by ramping the vertical position to 100 μm away and shutting the external shutter. The condensate is not affected by turning off the repulsive barrier and remains at the center of the hybrid trap. After one fourth of the oscillation period in the x-direction, the ancillary cloud reaches the hybrid trap minimum and collides with the BEC with kinetic energy equal to its initial potential energy. In this way, counterflow is induced between the condensate and the ancillary cloud. Variable hold times are chosen to allow interaction between the clouds during multiple oscillations of the ancillary cloud. Images are then taken with Faraday imaging in the vertical imaging system *in situ* and in expansion as discussed in Chapter 4. BEC number, fraction and temperature were also extracted from BEC images for atom-atom interaction analysis.

5.3 Experimental Results

This section begins with a discussion of the different methods in which the thermal counterflow experimental data are presented. Data for each separation corresponding

to specific kinetic energy values of the ancillary cloud are grouped together and briefly discussed.

At each separation, images of the target cloud were taken *in situ* and in expansion after different hold times during which the ancillary and target cloud collided. All images presented in this chapter were taken with the high magnification imaging system to show the cloud in the xy plane. The expansion procedure used in these images was the same as that for the vortex imaging test discussed in Chapter 4. This ensures that our imaging system will be able to image vortices if they are created due to thermal counterflow in the condensate. The interaction time, or time in which the ancillary and target clouds were overlapped at the center of the hybrid trap, was calculated using an average size of the condensate in the x-direction $2R_{TF_x} = 64$ μm and horizontal trapping frequency $\omega_x = 2\pi\times(33$ Hz) given the initial displacement of the ancillary cloud from the harmonic trap center and hold time. It is important to note that the images presented in this section are intensity autoscaled and consequently, the brightness of the image does not correspond to BEC column density. For the in-trap images, the size of the cloud gives a better indication of atom number. In the expansion images, both the condensate atoms and its associated thermal atoms (not the ancillary cloud) are visible and corresponding BEC number fractions can be interpreted.

From many of the images, BEC atom number, BEC fraction, thermal fraction and total atom numbers were extracted. After normalizing BEC fraction, thermal fraction and total atom number to the initial total atom number, these values were plotted as a function of the interaction time for a given separation. Finally, the temperature of the condensate was calculated and plotted as a function of interaction times for a given initial separation.

5.3.1 840 μm Separation Data

Figure 5.3 shows images of the target cloud before interaction with the ancillary cloud and after the following interaction times: 2.57 ms, 12.14 ms and 18.38 ms which correspond to experimental hold times of 100 ms, 500 ms, and 750 ms. No vortices are seen in expansion under the same conditions in which vortices were seen in the vortex imaging test. At this separation, we would expect to see vortices, if thermal counterflow were to induce vortex nucleation at all, because the kinetic energy of the ancillary cloud at an initial separation of 840μm was greater than the dipole activation energy. After imaging with a variety of different expansion procedures, no vortices were seen. Instead, we observed a signification amount of atom loss as seen in the change in size of the BEC *in situ* and in expansion after interaction

with the ancillary cloud. The apparent atom loss with interaction time is confirmed in the normalized atom fraction number plots in Figure 5.5 and Table **??** which contains the actual BEC atom number at different interaction times. This suggests that atom-atom collisions between atoms in the ancillary and condensate clouds are significant in thermal counterflow in dilute-gas BECs. As seen in Figure 5.4, the temperature is not significantly affected by interaction with the ancillary cloud in thermal counterflow. Temperatures of BECs that were held for the same time without interaction with the ancillary cloud are plotted alongside the temperatures of BECs after different interaction times. The temperatures of the clouds with and without interaction with the ancillary cloud are relatively the same. This suggests that either there is no significant amount of heating due to interactions with the ancillary cloud or that atoms are given enough energy to be suddenly lost from the trap.

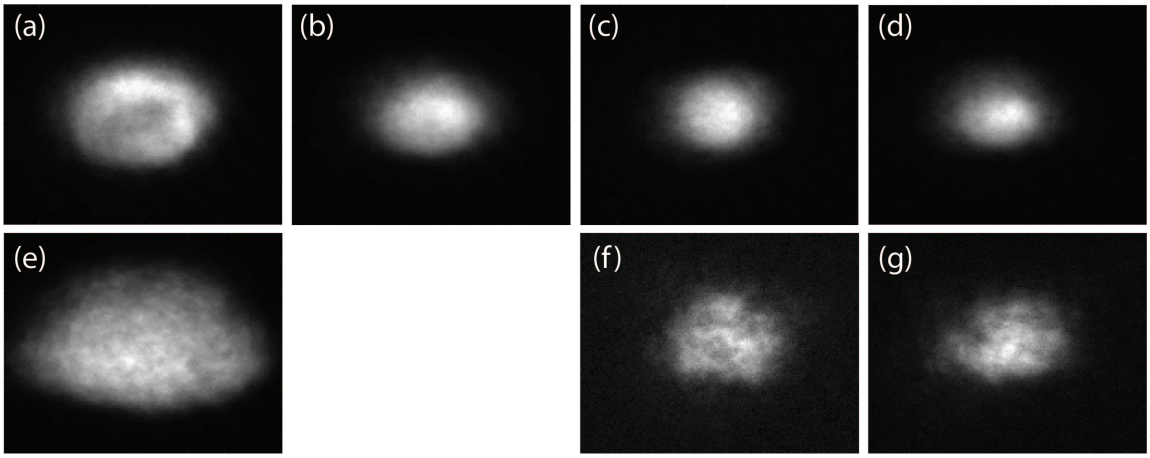

Figure 5.3: 97 μm $\times$ 97 μm images of BECs taken *in situ* (top row) and in expansion (bottom row) with an initial separation of 840 μm, corresponding to an ancillary cloud kinetic energy greater than the dipole activation energy. These images were taken after the following interaction times: (a) & (e) 0 ms, (b) 2.57 ms, (c) & (f) 12.13 ms and (d) & (g) 18.38 ms. Atom loss is evident in both *in situ* and expansion images. No significant thermal cloud associated with the BEC is seen in expansion which suggests that either not much heating occurs or atoms are given enough energy that they are suddenly lost from the trap.

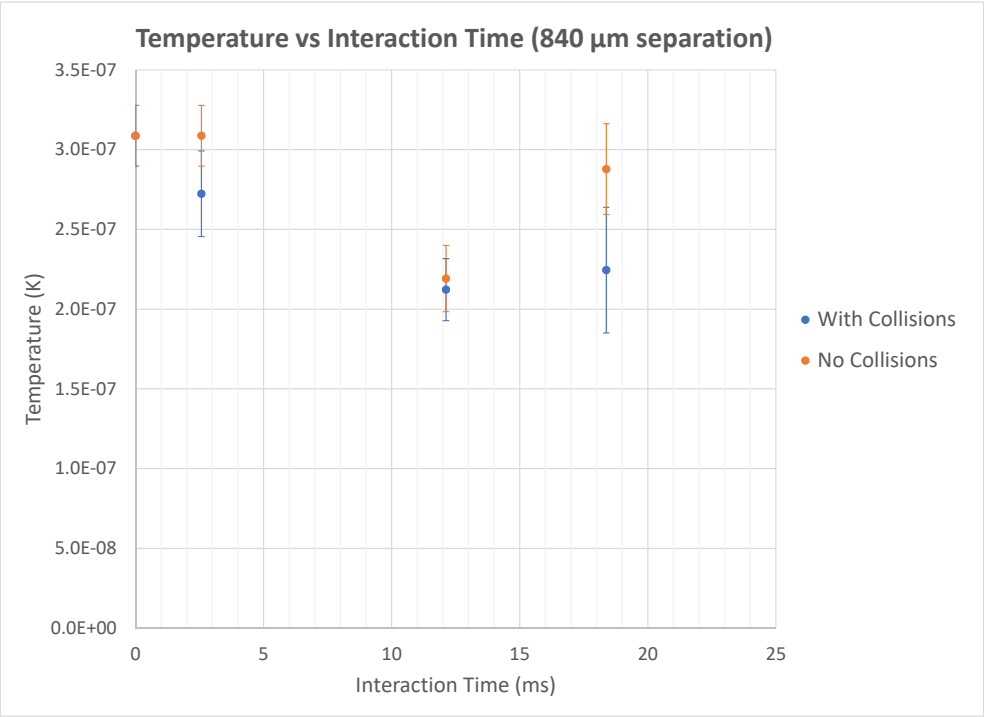

Figure 5.4: Extracted temperatures from fits to data of the target cloud at various interaction times with 840μm initial separation. Temperatures are also given for the target cloud without interaction with the ancillary cloud for reference. There is no overall trend of heating or cooling as interaction time increases.

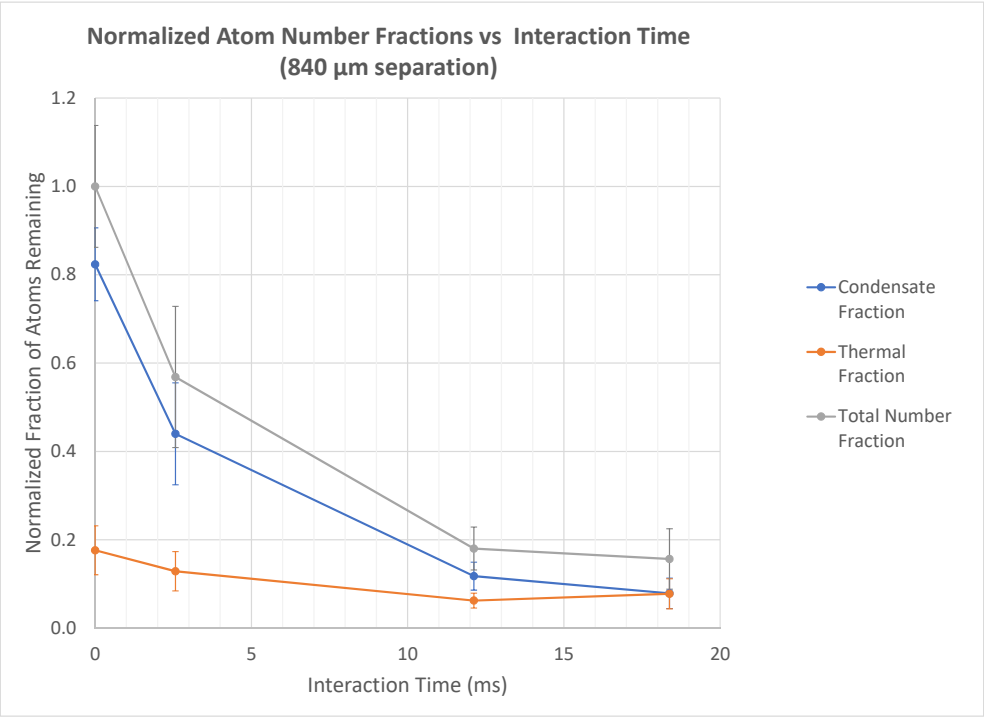

Figure 5.5: Extracted BEC fraction, thermal fraction, and total number fraction from fits to data normalized to the initial total atom number at 0 ms interaction time at various interaction times with 840μm initial separation. In general, atom loss, from both condensate and thermal atoms, increases with increasing interaction time.

5.3.2 600 μm Separation Data

Figure 5.6 shows images of the BECs before interaction with the thermal cloud and after the following interaction times: 0.48 ms, 3.38 ms and 15.93 ms which correspond to experimental hold times of 10 ms, 100 ms, and 500 ms. At 600 μm initial separation, the atoms in the ancillary cloud have kinetic energy comparable to the dipole activation energy when they interacts with the target cloud. As shown in Figure 5.6, no vortices are seen in expansion. Once again, atom loss is apparent

Interaction time (ms)	BEC number (10^6)	BEC Fraction	Temperature (μK)
0	5.1	0.82	309
2.57	2.75	0.77	272
12.13	0.74	0.65	212
18.38	0.49	0.50	224

Table 5.1: BEC number, BEC fraction and temperature of condensates for different interaction times at 840 μm initial separation.

in the changing size of the BEC in both the *in situ* and in expansion images. Images (b) and (f) show the BEC *in situ* and in expansion respectively after one pass of the ancillary cloud through the condensate resulting in 0.48 ms interaction time. Even after one pass, condensate atoms are lost as seen in the change in size of the expansion image from no interaction in image (e) to expansion after one pass of the thermal cloud in image (f). In-trap image (d) at 15.93 ms interaction time suggests that after enough interaction, heating is evident. The cloud in image (d) does not have hard edges on the outside which corresponds to a significant thermal component that is not seen in images (a) - (c). At this separation, there was not enough data to extract accurate numbers and temperatures so Figure 5.6 represents the majority of the data at 600μm initial separation.

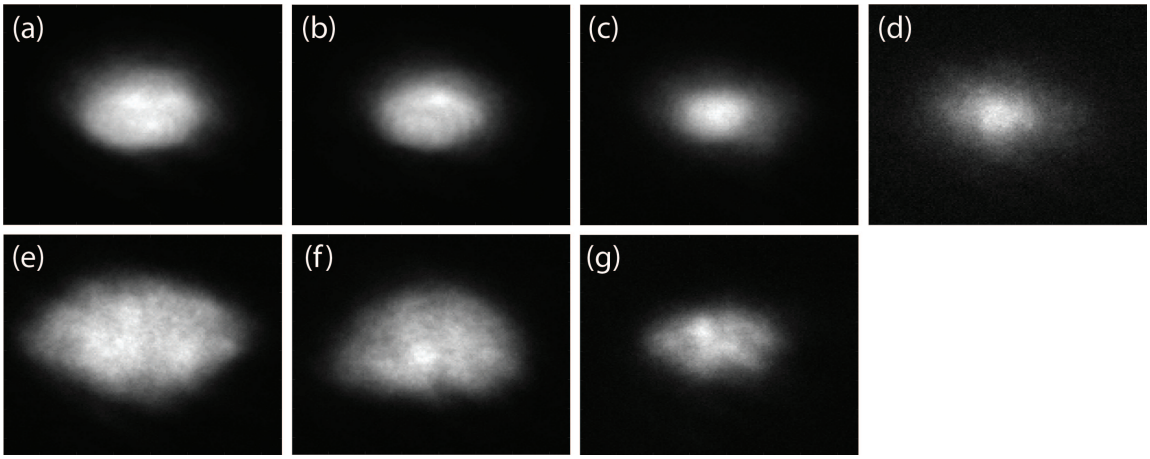

Figure 5.6: 97 μm $\times$ 97 μm images of BECs *in situ* (top row) and in expansion (bottom row) with an initial separation of 600 μm, corresponds to an ancillary cloud kinetic energy equal to the dipole activation energy. These images were taken after the following interaction times: (a) & (e) 0 ms, (b) & (f) 0.48 ms, (c) & (g) 3.38 ms and (d) 15.93 ms. Atom loss is evident in both *in situ* and expansion images. Comparison between images (a) and (b) and (e) and (f) shows atom loss due to one pass of the ancillary cloud through the condensate. No significant heating is seen at the earlier interactions times but heating is seen in (d) after 15.93 ms of interaction between the condensate and the ancillary cloud. The shape of the image in (d) does not have hard edges like the rest of the images which corresponds to a significant thermal component. This suggests that lower-kinetic energy ancillary clouds with long enough interaction times with the condensate can cause heating.

5.3.3 400 μm Separation Data

Figure 5.7 shows in-trap and expansion images of the target cloud before interaction with the ancillary cloud and after the following interaction times: 5.41 ms and 25.5 ms which correspond to experimental hold times of 100 ms and 500 ms. At 400 μm initial separation, the ancillary cloud has kinetic energy less than the calculated dipole activation energy when it interacts with the condensate. As shown in Figures 5.7 and 5.8, no vortices are seen in expansion. Atom loss is shown in images (b) and (e) in Figure 5.7 in the changing size of the BEC. After 25.5 ms interaction time, expansion image (f) shows a significant thermal component compared to image (e) which indicates heating of the cloud due to interactions between the ancillary cloud and the condensate. Image (g) is the same expansion image as (f) with the condensate part of the cloud saturated to emphasize the thermal atoms. The thermal

component expands much faster than the condensate atoms and is much less dense which can be seen in the larger extent and lower intensity of the thermal component in the expansion image. Figure 5.8 shows expansion images at eight different interaction times giving a clearer picture of the overall heating and loss of atoms in the condensate. Images (a) - (e) clearly show loss of condensate atoms while (f) - (h) show an increase in the thermal component, corresponding to heating, and loss of condensate atoms as well. This temperature increase observed in images (f) - (h) is confirmed in the calculated temperature as a function of interaction time in Figure 5.9. From the Figure, it appears that the temperature increases linearly with increasing interaction time. This suggests that heating occurs at smaller interaction times in images (a) - (e) as well as the longer interaction times where the thermal component is obvious. The apparent increased atom loss with increased interaction time observed in Figures 5.7 and 5.8 is confirmed in the normalized atom fraction number plots in Figure 5.10 and Table **??** in which number and temperature data extracted from BEC images are summarized. Figure 5.10 shows that the total atom number and BEC fraction decreases while the thermal fraction increases with increasing interaction time corresponding total atom loss and heating of the condensate as a result of interactions between the ancillary cloud and condensate.

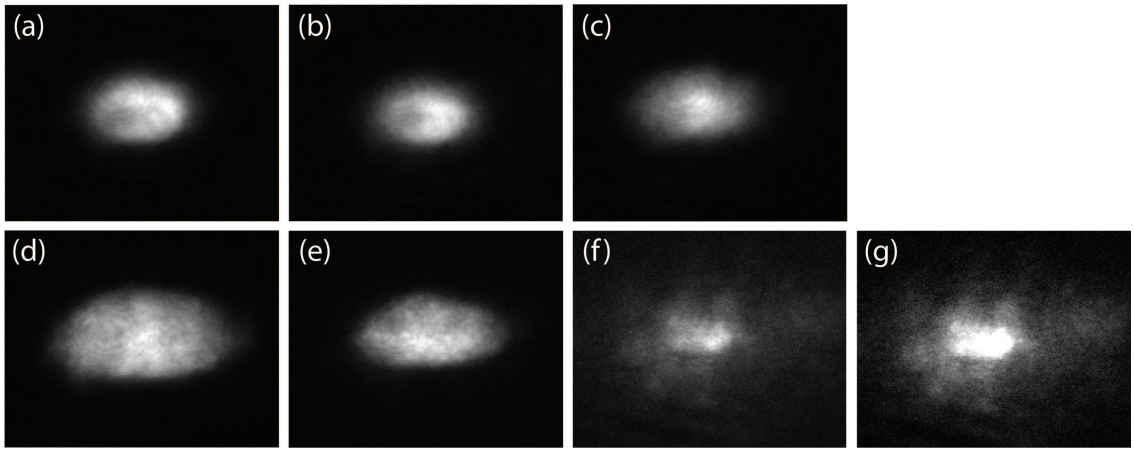

Figure 5.7: 129 μm $\times$ 129 μm images of BECs taken *in situ* (top row) and in expansion (bottom row) with an initial separation of 400 μm, which corresponds to an ancillary cloud kinetic energy less than the calculated dipole activation energy. These images were taken after the following interaction times: (a) & (d) 0 ms, (b) & (e) 5.41 ms and (c), (f) & (g) 25.5 ms. Atom loss is evident in both *in situ* and expansion images for the smallest interaction time. At the longer interaction time a significant amount of heating is apparent in the low density thermal component of the cloud seen in the expansion image (f). Some fraction of atoms are still condensed which is evident in the bright spot in the middle of image (f) corresponding to the condensate atoms that expand much more slowly than the thermal atoms. Image (g) is the same as image (f) with the condensate atoms saturated to exaggerate the thermal component of the cloud that has a much larger spatial extent in expansion than the condensate atoms. A difference in shape between in-trap images (b) and (c) also suggests heating at longer interaction times. Image (c) has a more gaussian distribution and image (b) has the hard edges characteristic of the Thomas-Fermi distribution in a condensate.

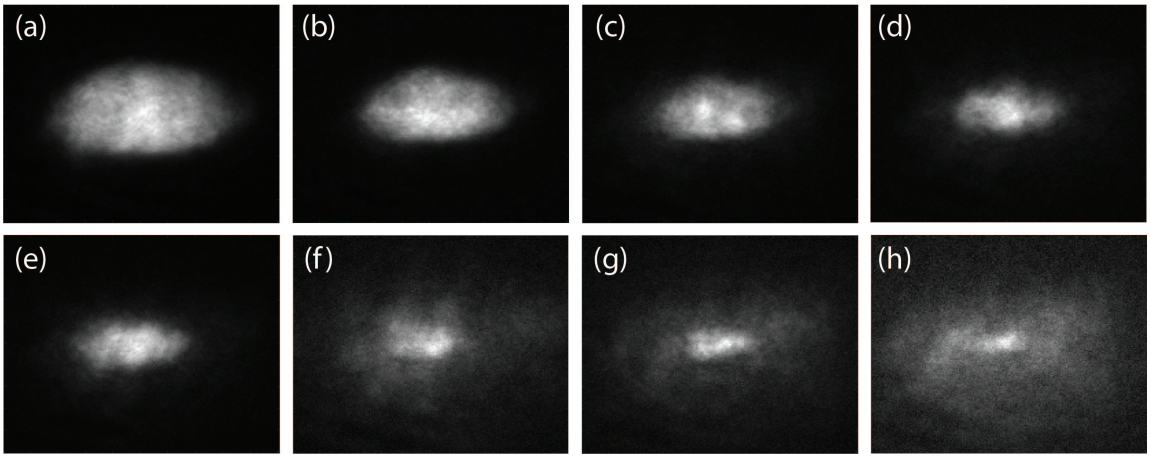

Figure 5.8: 129 μm $\times$ 129 μm expansion images of BECs with an initial separation of 400 μm, which corresponds to an ancillary cloud kinetic energy equal to the dipole activation energy. These images were taken after the following interaction times: (a) 0 ms, (b) 5.41 ms, (c) 10.04 ms, (d) 15.45 ms, (e)20.09 ms, (f) 25.5 ms, (g) 30.9 ms and (h) 38.63 ms which corresponds to experimental hold times of 0, 100, 200, 300, 400, 500, 600 and 750 ms respectively. In images (a) - (e) the size of the condensate in expansion decreases with increasing interaction time but no significant thermal component is shown, which corresponds to total atom number loss. However, in image (f) after 25.5 ms interaction time, a significant thermal component is observed corresponding to heating of the cloud. In images (f) - (h), there is continued BEC atom loss as the size of the condensate decreases and increase in the number of atoms in the thermal cloud corresponding to heating. Image (h) shows an expansion image of a BEC with a very small thermal component. At this point the temperature of the cloud is just below T_c. This suggests that with larger interaction times, the temperature would increase above T_c resulting in no condensed atoms.

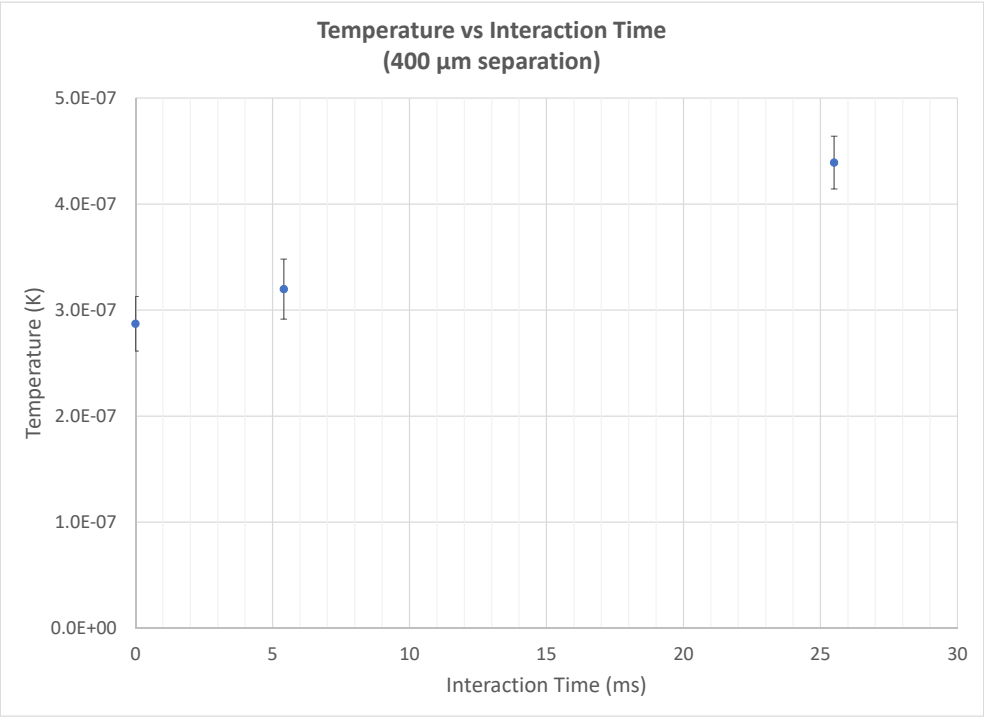

Figure 5.9: Extracted temperatures from fits to data at various interaction times with 400μm initial separation. The temperature appears to linearly increase with increasing interaction time suggesting that heating occurs for all interaction times at 400μm initial separation.

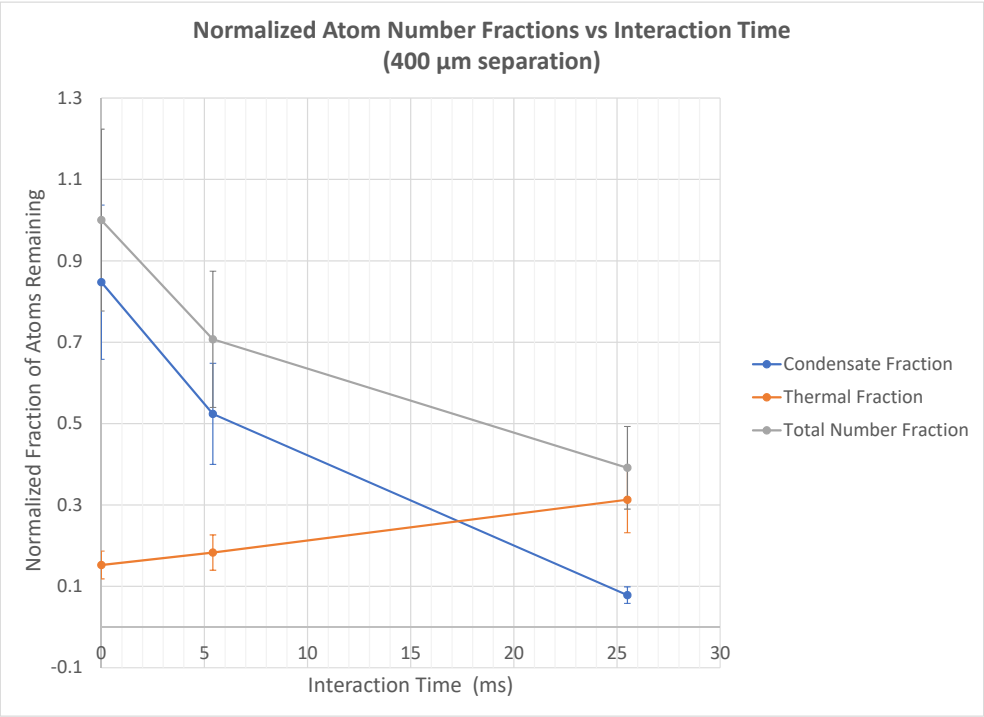

Figure 5.10: Extracted BEC fraction, thermal fraction, and total number fraction from fits to data normalized to the initial total atom number at 0 ms interaction time at various interaction times with 400μm initial separation. This plot shows that total number and BEC fraction decreases with increasing interaction energy which corresponds to increasing atoms loss. The thermal fraction increases with increasing interaction time indicating that the heating occurs when the ancillary cloud and BEC interact.

5.3.4 260 μm Separation Data

Figure 5.11 shows *in situ* and expansion images of condensates after the following interaction times with the ancillary cloud: 5.95 ms, 8.33 ms, 11.9 ms, 14.28 ms, 15.47 ms and 23.8 ms which correspond to experimental hold times of 75, 100, 150, 175, 200 and 300 ms respectively. At 260 μm initial separation, the atoms in the

Interaction time (ms)	BEC number (10^6)	BEC Fraction	Temperature (μK)
0	5.4	0.85	287
5.41	3.3	0.74	320
25.5	0.5	0.20	439

Table 5.2: BEC number, BEC fraction and temperature for different interaction times at 400 μm initial separation.

ancillary cloud have a kinetic energy less than the calculated dipole activation energy when they interact with the condensate. As shown in Figure 5.11, no vortices are seen in expansion. However, a significant amount of atom loss and heating is evident in both expansion and in-trap images. As seen in expansion images (e) - (m), the high-density component of the cloud corresponding to the condensate atoms decreases with increasing interaction time. Heating is evident by the change in shape of the cloud from a Thomas-Fermi distribution with hard edges in image (a) to a Gaussian distribution with soft edges in image (k). The apparent heating of the cloud with increasing interaction time between the high energy thermal cloud and the condensate is also observed in the expansion images. It is evident in images (l) - (n) that the condensate fraction decreases as the thermal fraction increases until no condensate atoms remain. At this point, the cloud has been heated to above T_c and the condensate has been destroyed. Figure 5.12 shows the calculated temperature of the cloud at different interaction times. The first three data points show a linear increase in the temperature with increasing interaction time. Figure 5.13 shows the normalized BEC fraction, thermal fraction and total fraction of atoms remaining at different interaction times. The first three data points show a decrease in BEC fraction and total atom number and an increase in thermal fraction. This corresponds to a temperature increase due to the interaction between the ancillary cloud and the condensate. Around 15 ms interaction time, many atoms are lost in both the condensate and thermal components of the target cloud. As interaction time increases, loss and heating continues until the condensate fraction goes to 0 and a thermal cloud remains. Specific number and temperature values corresponding to Figures 5.12 and 5.13.

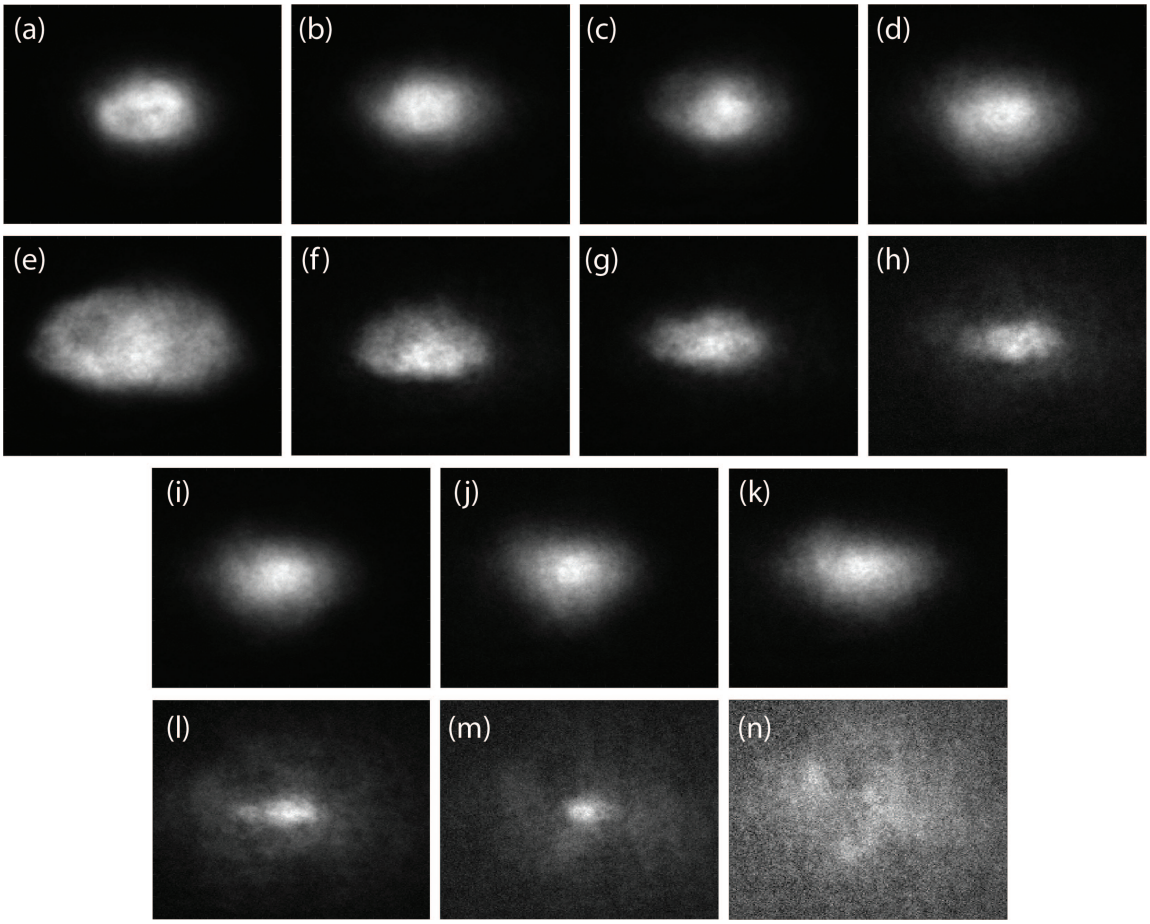

Figure 5.11: 129 μm $\times$ 129 μm images of BECs taken *in situ* (first and third rows) and in expansion (second and fourth rows) with an initial separation of 260 μm, which corresponds to an ancillary cloud kinetic energy less than the calculated dipole activation energy. These images were taken after the following interaction times: (a) & (e) 0 ms, (b) & (f) 5.95 ms, (c) & (g) 8.33 ms, (d) & (f) 11.9 ms, (i) & (l) 14.28 ms (j) & (m) 15.47 ms and (k) & (n) 23.8 ms corresponding to experimental hold times of 0, 75, 100, 150, 175, 200 and 300 ms respectively. Atom loss and heating are both apparent in the in-trap and expansion images. The size of the high density component of the cloud, or condensate atoms, decreases with increasing interaction time in expansion corresponding to decreases condensate fraction. The shape of the cloud *in situ* changes from one with hard edges in image (a) with 0 ms interaction time to a Gaussian distribution shown in image (k) which corresponds to a thermal distribution instead of a Thomas-Fermi distribution in a condensate. The heating of the cloud with interaction time is obvious in expansion images (l) - (n) in which a cloud with a small BEC fraction is heated to above T_c and no condensate atoms remain. For any interaction times above 23.8 ms, the cloud remains a thermal cloud and atom loss is increased.

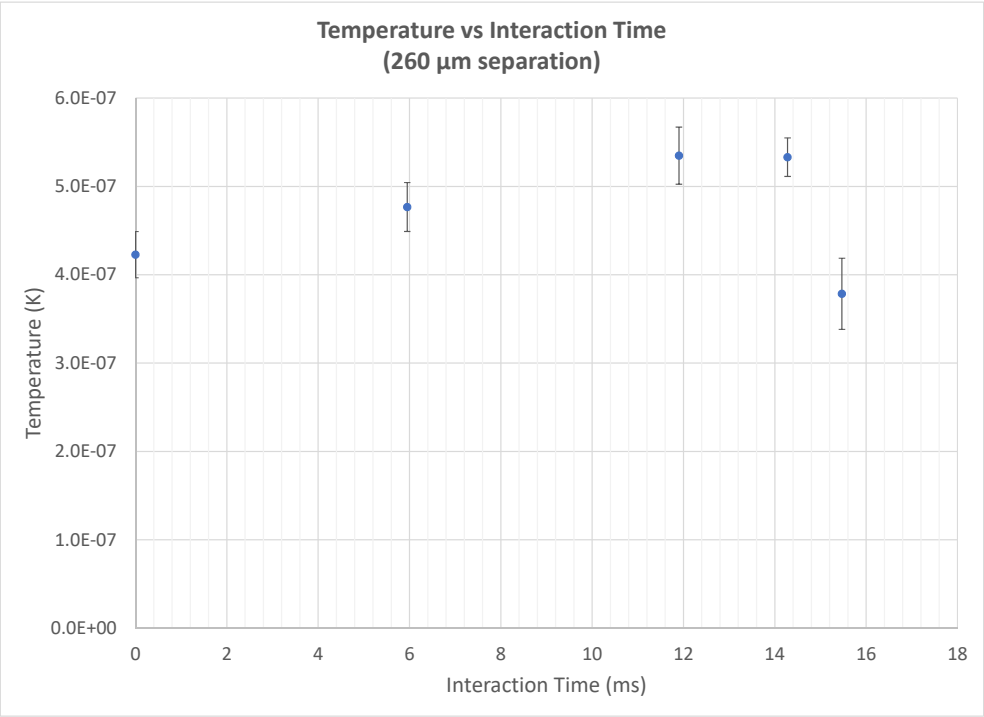

Figure 5.12: Extracted temperatures from fits to data at various interaction times with 260μm initial separation. The first three data points show a linear increase of temperature with increasing interaction time.

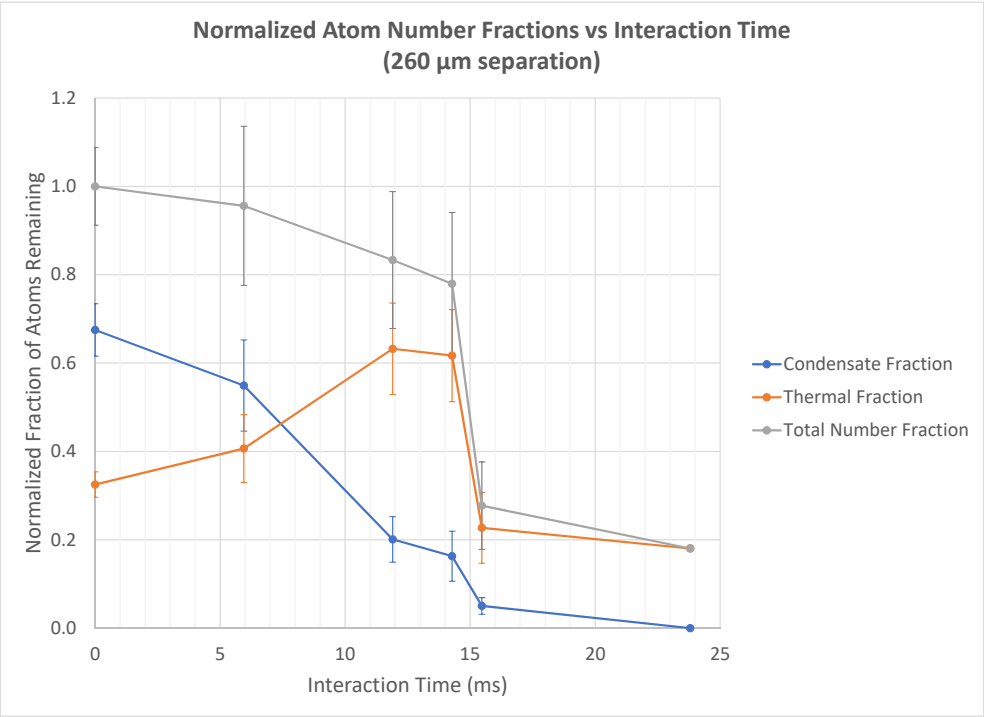

Figure 5.13: Extracted BEC fraction, thermal fraction, and total number fraction from fits to data normalized to initial total atom number at various interaction times with 260 μm initial separation. This plot shows that total number and BEC fraction decrease with increasing interaction time which corresponds to increasing atoms loss. The first three data points show an increase in the thermal fraction with increasing interaction time indicating heating of the cloud. However, around 15 ms interaction time, there is loss of both thermal and condensate atoms in the target cloud.

5.3.5 165 μm Separation Data

Figure 5.14 shows *in situ* and expansion images of condensates after the following interaction times with the ancillary cloud: 9.41 ms, 18.83 ms and 24.48 ms which correspond to experimental hold times of 75, 150 and 200 ms respectively. At 165 μm initial separation, atoms in the ancillary cloud have a kinetic energy less than the

Interaction time (ms)	BEC number (10^6)	BEC Fraction	Temperature (μK)
0	7.2	0.68	423
5.95	5.9	0.55	477
11.9	2.2	0.20	535
14.28	1.8	0.16	533
15.47	0.54	0.05	378
23.8	0.0	0.0	-

Table 5.3: BEC number, BEC fraction and temperature for different interaction times at 260 μm initial separation.

calculated dipole activation energy when they interacts with the condensate. As shown in Figure 5.14, no vortices are seen in expansion. As seen in most of the other separations, heating and condensate atom loss are evident in the BEC images. Expansion images (d) - (g) clearly show loss of condensate atoms with the decreasing size of the BEC component of the cloud as well as heating with the increasing thermal component. Figure 5.15 shows the temperature of the cloud at different interaction times. The last three data points show a linear increase in the temperature with increasing interaction time. Figure 5.16 shows the normalized BEC fraction, thermal fraction and total fraction of atoms remaining at different interaction times. Total atom number as well as number of condensate atoms decreases with increasing interaction time. In general, the thermal fraction increases which corresponds to increased temperature of the cloud. The actual atom numbers and temperatures are given in Table **??**.

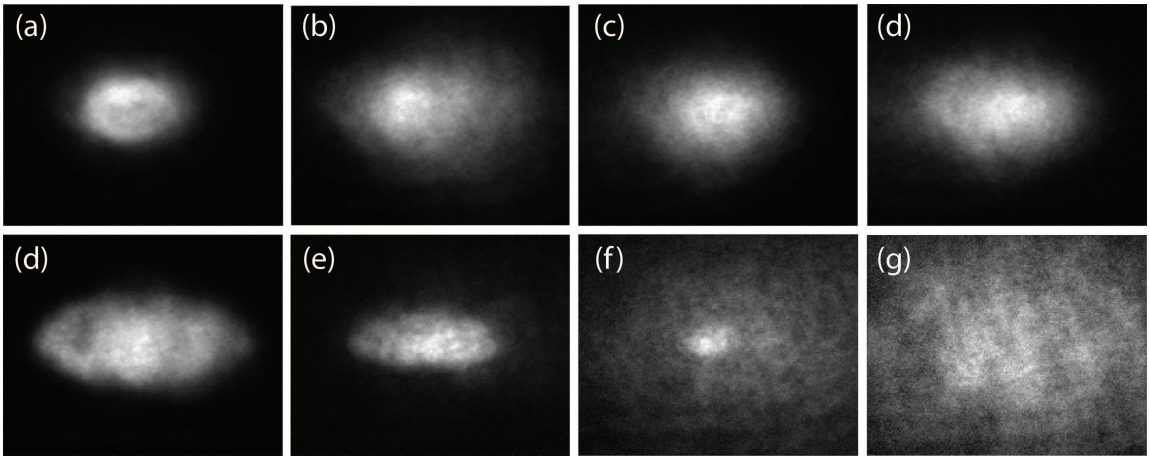

Figure 5.14: 129 μm $\times$ 129 μm images of BECs taken in-trap (top row) and in expansion (bottom row) with an initial separation of 165 μm, which corresponds to an ancillary cloud kinetic energy less than the calculated dipole activation energy. These images were taken after the following interaction times: (a) & (e) 0 ms, (b) & (f) 9.41 ms, (c) & (g) 18.83 ms and (d) & (h) 24.48 ms corresponding to experimental hold times of 0, 75, 15 and 200 ms respectively. Atom loss and heating are both apparent in the *in situ* and expansion images. After 24.48 ms of interaction time, the BEC has almost completely turned into a thermal cloud as seen in expansion image (g). Expansion images (d) and (e) show loss of condensate atoms and image (f) shows a significant fraction of thermal atoms indicating heating of the atom cloud.

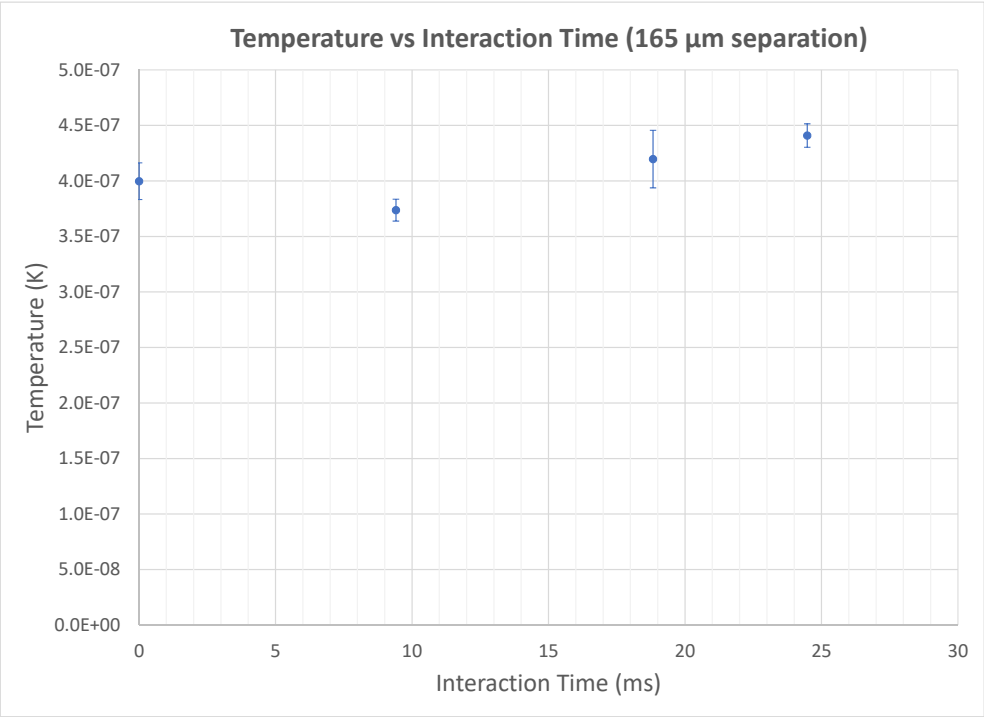

Figure 5.15: Extracted temperatures from fits to data at various interaction times with 165μm initial separation. The last three data points show a relatively linear increase in the temperature with increasing interaction time.

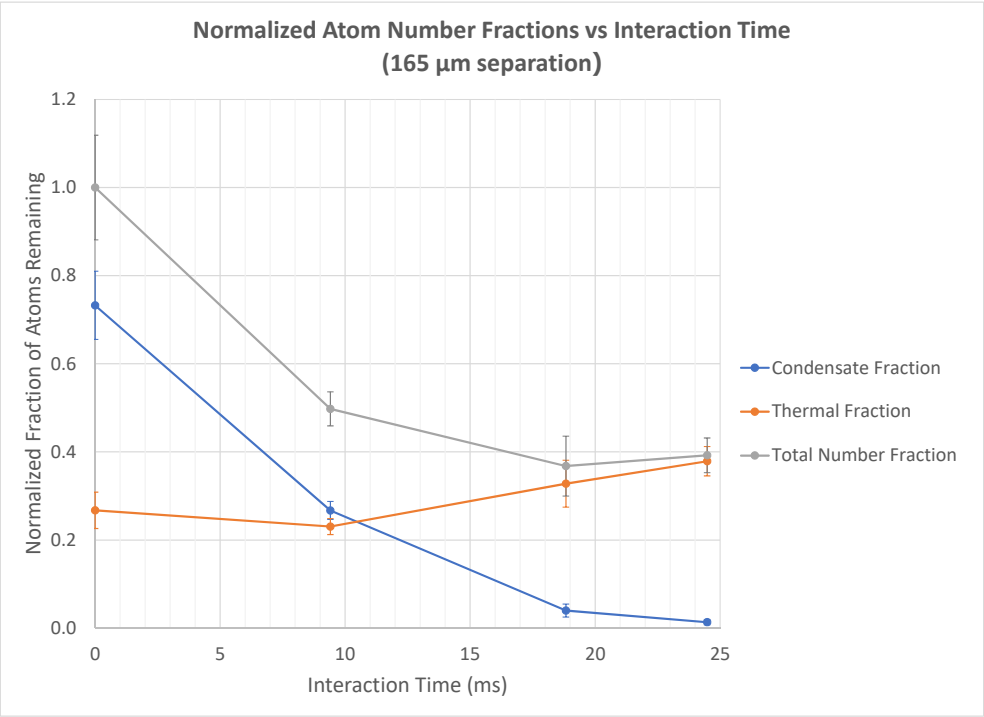

Figure 5.16: Extracted BEC fraction, thermal fraction, and total number fraction from fits to data normalized to intial total atom number, at various interaction times with 165μm initial separation. There is an increasing total atom number loss as well as condensate number loss with increasing interaction times. For the most part, the thermal fraction increases with increasing interaction time which corresponds to heating of the atom cloud.

5.4 Discussion

The experimental data presented in Section 5.3 revealed that vortices were not observed in BECs after interaction with the ancillary cloud. Even in the experiment with the largest initial separation where the kinetic energy of the ancillary cloud was larger than the calculated dipole activation energy, vortices were not observed. However, heating and atom loss were seen in almost every experiment with different

Interaction time (ms)	BEC number (10^6)	BEC Fraction	Temperature (μK)
0	6.9	0.73	400
9.41	2.5	0.54	374
18.83	3.8	0.11	420
24.48	1.3	0.03	441

Table 5.4: BEC number, BEC fraction and temperature for different interaction times at 165 μm initial separation.

initial separations and different interaction times. This motivates a further discussion of atom-atom collisions in order to understand the mechanisms responsible for the heating and atom loss observed in the thermal counterflow experiments.

5.4.1 Consideration of Atom-Atom Collisions

Inelastic collisions are collisions that change the state of the trapped atoms. As a result, atoms can be lost from the trap when scattered to untrapped states. Heating of the atomic sample also occurs as kinetic energy is released from the collisions [36]. Because atoms in our apparatus are trapped in the ^{87}Rb $|F = 1, m_F = -1\rangle$ ground state, spin flips due to inelastic collisions are suppressed by conservation of angular momentum [37]. At high enough densities, 3-body collisions, in which a diatomic molecule and a free atom are produced, are the dominant inelastic collisions in alkali atoms where the spin relaxation process is suppressed as in the case discussed above. When the diatomic molecule is created, the molecule and the free atom share the kinetic energy gained in the binding of the molecule [36]. As a result, the molecule is no longer in a trappable state and the free atom has enough energy to escape the trap resulting in the loss of three atoms. Because this loss mechanism depends on three atoms being in the same region in space, it becomes significant at high densities and can limit the lifetime of a condensate.

BECs created in our apparatus have a lifetime on the order of 30 s. This implies that on the hundreds of ms timescale of the thermal counterflow experiment, 3-body loss is not significant. In the presence of the ancillary thermal cloud, the peak density slightly increases, but not enough to increase the 3-body loss rate so that significant atom loss is observed over the experiment timescales. This suggests that 3-body loss is not responsible for atom loss observed in the thermal counterflow experiment.

Elastic collisions, in which the atoms' quantum states remain unchanged, are the other type of atom-atom collision that occurs. In elastic collisions, momentum is

elastically transferred between atoms which aids rethermalization of an atomic sample [36]. Evaporative cooling utilizes 2-body elastic collisions to transfer momentum between atoms until the entire atomic sample rethermalizes to a lower temperature after the selective removal of highly energetic atoms from the sample. In this case, 2-body elastic collisions aid in the cooling of an atomic sample. However, if high-energy atoms were added to the atomic sample instead of removed, 2-body elastic collisions could theoretically cause heating of an atomic sample. This is most likely the mechanism responsible for both heating and loss observed in our experiment.

5.4.2 Discussion of Heating and Loss Mechanisms

As the ancillary cloud collides with the target cloud, some momentum is transferred to the condensate through 2-body elastic collisions between atoms in the two clouds. After the ancillary cloud has passed through the condensate, elastic collisions between the condensate and its associated thermal cloud result in rethermalization of the cloud to a higher temperature. It is possible that during the rethermalization process as the transferred momentum is distributed throughout the cloud in three dimensions that some atoms have enough energy to escape the trap. This would correspond to total atom loss observed in experimental data from all ancillary cloud kinetic energies tested.

As discussed in Section 5.3, a linear increase in temperature is observed with increasing interaction times for initial separations of 165 μm, 260 μm and 400 μm. After fitting the experimental data from two larger initial separations, the following equations were obtained:

$$T_{400} = 5.951t + 287.36 \text{ nK} \tag{5.4}$$

$$T_{260} = 9.411t + 422.33 \text{ nK} \tag{5.5}$$

where T_{400} and T_{260} are the temperatures of the target cloud after collisions with an ancillary cloud with initial separations of 400 μm and 260 μm respectively and t is the interaction time in ms. After normalizing the above equations to the initial temperature given by the intercepts, the following normalized heating rates were obtained.

$$\frac{1}{T_{400}}\frac{dT_{400}}{dt} = .0207 \text{ ms}^{-1} \tag{5.6}$$

$$\frac{1}{T_{260}}\frac{dT_{260}}{dt} = .0223 \text{ ms}^{-1} \tag{5.7}$$

The percent difference between the calculated normalized heating rates is only 7.4%.

This suggests that the heating of the condensate due to collisions with the ancillary cloud is independent of the kinetic energy of the atoms in the ancillary cloud. Similarly, Figure 5.17 shows that the change in the normalized BEC fraction with interaction time is roughly the same for 165 μm, 260 μm and 400 μm initial separations. This suggests that loss of condensate atoms due to interaction between the ancillary cloud and the condensate is more dependent on interaction time than the kinetic energy of atoms in the ancillary cloud.

Scattering of atoms due to a collision between the ancillary cloud and condensate is shown in Figure 5.18. The image was taken after 12.13 ms of interaction time at which point the ancillary cloud (left) had just collided with the condensate (right). The condensate and high energy thermal clouds are saturated to allow the scattered atoms to be visible in the image. A halo of scattered atoms in the shape of an eclipse is seen to the left of the condensate as a result of the collision. See Reference [38] for more information regarding imaging of atom scattering patterns due to cold collisions of atoms. The scattering pattern observed confirms the analysis that the collision between the two clouds results in a transfer of momentum to the BEC. We suspect that the scattered atoms eventually travel back towards the BEC location at the center of the trap and elastic collisions between the scattered atoms and the remaining atoms results in rethermalization of the cloud to a higher temperature.

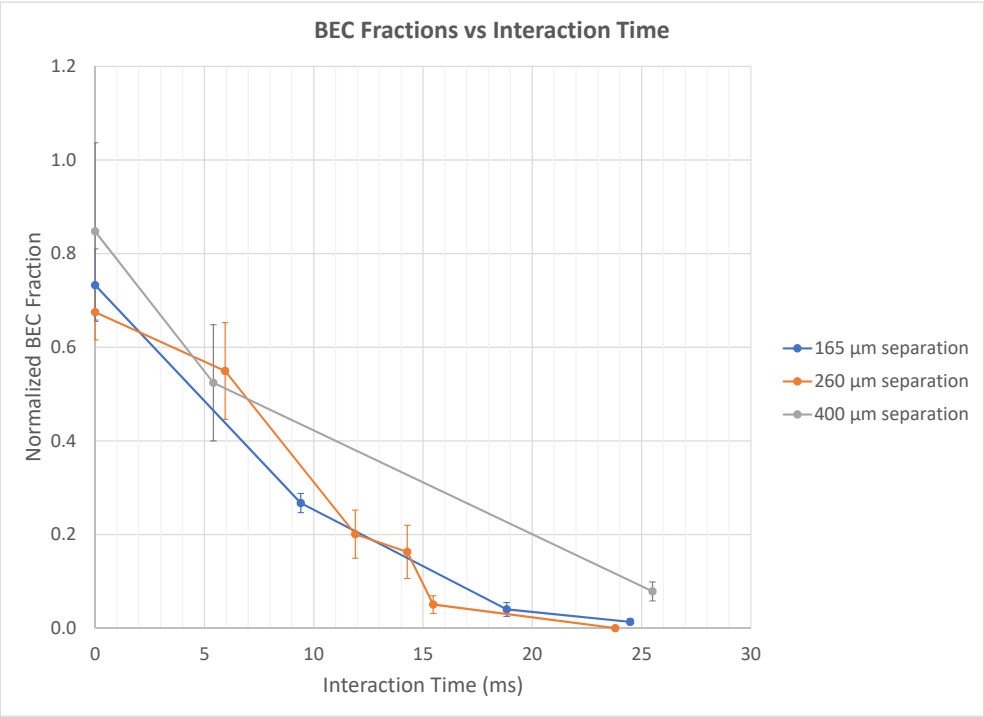

Figure 5.17: Extracted BEC fraction from fits to data normalized to initial atom number as a function of interaction time for 165μm, 260μm and 400μm initial separations. For each separation, the normalized condensate fraction decreases at roughly the same rate with increasing interaction time.

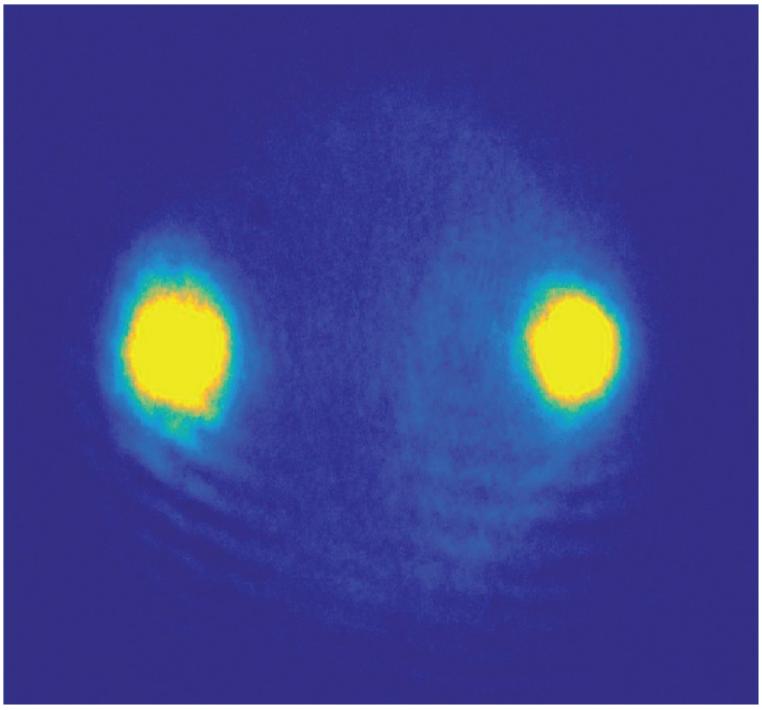

Figure 5.18: 453 μm $\times$ 284 μm image taken after a 12.13 ms hold time with an 840 μm initial separation. The ancillary cloud (left) has just collided with the BEC (right), moving right to left. The BEC and ancillary clouds are saturated to allow the scattered atoms to be visible. A halo of scattered atoms in the shape of an eclipse is seen to the left of the condensate as a result of the collision.

5.5 Conclusion

We conclude from the experimental data that thermal counterflow does not create vortices in dilute-gas BECs under typical experimental conditions. Instead, heating and atom loss from elastic collisions between atoms a the high-energy thermal cloud (ancillary cloud) and the condensate dominate BEC dynamics. Few-body interactions and collisions between atoms in dilute-gas BECs is one of the main differences between BECs and superfluid helium. Dilute-gas BECs can be considered a quantum fluid. They can be made closer to the hydrodynamic regime via density increases [39]. Although this would possibly enable vortex production, three-body loss rates would also be increased. The introduction of a low-density ancillary thermal cloud into the experiment results in a cloud that is no longer in the hydrodynamic regime as the two clouds are overlapped. As a result, significant heating and atom loss occur

during these collisions.

These are interesting results because forced heating of a condensate and methods for destroying a condensate have not been well studied. Techniques for cooling condensates are well known such as optical and RF evaporation. However, there is no method for RF and optical heating. In addition, laser beams can be used to stir up vortices in a condensate and the condensate still has a relatively long lifetime compared to the interaction times on the order of tens of ms during which the condensate was destroyed in the thermal counterflow experiments. For these reasons, data presented in this chapter provide exciting new insights into methods for heating and destroying condensates as well as the limitations of dilute-gas BECs for quantum turbulence studies.

APPENDIX A

Timing Sequence

This appendix gives a detailed explanation of every step in a simplified version of the most current timing sequence. The timing sequence described in this chapter includes the necessary time steps to create a BEC and a thermal cloud in the tight hybrid optical-magnetic trap, displace the two clouds by a variable amount, and allow a thermal ancillary cloud to collide with a target BEC. The timing sequence described was used to do the experiment of Chapter 5 described in this dissertation. The purpose of this appendix is to explain all of the steps in the timing sequence and serve as a reference for current and future students, aiding them in their understanding of the timing sequence.

A.1 Cooling and Trapping in MOT cell

1. **Start run – No trip:** This time step is disabled at the beginning of the timing sequence. The TDK power supply used to trip at the end of every run when all values reset to the MOT loading parameters. We found that starting the timing sequence with this disabled time step prevents the power supply from tripping at the end of each run.

2. **MOT load:** 2D cooling and repump light, push beam light, and 3D cooling and repump light are all on. This means that all of the shutters are open and that for the 3D cooling and repump light and push beam, the AOM amplitude voltage is set to about 0.85 V (on a scale from 0 to 1 V). The AOM RF switch for all light is also on (these switches are controlled by a TTL output from the computer, high is on, low is off). The TDK power supply is set to the MOT load value which is around 7 A. The plug vertical and horizontal PZT control voltages are also set in this time step to values that center the plug the in quadrupole trap once the atoms are transferred to the BEC cell.

3. **Push beam off:** In this step, the push beam shutter is closed and the AOM RF switch is turned off which blocks the push beam. In the presence of the push beam, the atoms in the MOT are slightly displaced from the center of the magnetic trap. Turning the push beam off 500 ms before the CMOT timestep

allows the atoms to relax back to the center of the magnetic trap for the most efficient transfer of atoms to the magnetic trap.

4. **2D repump and cooling beams off:** The 2D repump and cooling shutters close during this time step to prevent any atoms traveling from the 2D to 3D MOT chambers during the CMOT stage.

5. **CMOT:** The Compressed MOT stage is designed to further cool and compress the atoms trapped in the MOT for better transfer to the magnetic trap. During the CMOT stage, the 3D repump and cooling AOM amplitudes are snapped to a lower value, immediately decreasing the repump power. Throughout the duration of the time step, the 3D cooling frequency is linearly ramped further away from resonance to increase the amount the light is red–detuned. The magnetic field is also snapped to a lower value during this stage.

6. **Pump into F = 1:** By turning off the 3D repump light off 0.5 ms before the 3D cooling light is turned off, all of the atoms are pumped into the F=1 ground state. The 3D repump light is turned off by pre–triggering the shutter to close at the beginning of the time step, snapping the AOM amplitude voltage to 0 V and turning the RF switch to the AOM off.

7. **Dark:** All lights and fields are turned off 1 ms before transfer into the magnetic trap. This is done by turning off the RF switch to the 3D cooling AOM, snapping the 3D cooling AOM to 0 V, and snapping the current in the MOT coils to 0 A.

8. **Transfer to Magnetic trap:** The MOT coils are snapped up to the catch value and most atoms in $|\mathrm{F} = 1, m_\mathrm{F} = -1\rangle$ are trapped in the quadrupole field created by the MOT coils.

9. **Kill pulse:** The 3D cooling light is turned on for 2.5 ms to get rid of any atoms that are still in F = 2.

A.2 Magnetic Transfer

10. **Coils 3-5 ramp up:** Coils 3-5 are the coils that are used to transfer atoms from the MOT cell to the BEC cell on the north side of the chamber. During this step, the coils are ramped up to their transfer start values over 500 ms.

11-16. **Transfer North Forward:** Coils 3-5 follow waveforms created in MATLAB to transfer atoms from the MOT cell to the north BEC cell with close to constant magnetic field gradient in the direction of transfer. This transfer is broken up into six different time steps.

17-22. **Transfer North Back:** These time steps are used to transfer atoms back from the north BEC cell to the MOT cell. The waveforms in these transfer steps are simply reversed from those in the transfer north forward steps. Usually these time steps are disabled but they can be used if transfer efficiency to the BEC cell and back needs to be measured.

23. **Transfer to BEC quadrupole coils:** During this time step, transfer coils 3-5 are linearly ramped from their ending forward transfer value down to 0 A while the BEC quadrupole coils are linearly ramped up from 0 A to a current that creates a gradient of 250 G/cm in 500 ms.

A.3 RF Evaporation

24. **Start RF evaporation:** The RF switch is turned on to allow amplification of the RF output from the Agilent function generator. The RF sweep trigger is switched to low during this step, triggering the start of RF frequency ramps that have been previously programmed by the MATLAB RF evaporation code and stored in the function generator. This time step starts with a high frequency cut, during which frequencies are swept from 80 MHz down to 30 MHz in about 3 s. The high frequency cut selectively evaporates the high energy atoms, preventing them from colliding with the rest of the atom cloud and heating it up throughout the evaporation procedure. RF evaporation continues at a much slower rate after the high frequency cut to frequencies below 30 MHz. At the beginning of this step, the vertical bias field is ramp up from 0 to 0.93 V which slightly changes the vertical position of the quadrupole trap. This is done to provide a 30 μm vertical displacement between the plugged quadrupole trap and the optical dipole trap as soon as the 1064-nm trapping laser is ramped up.

25. **RF evaporation to 5 MHz:** The RF switch is again enabled during this time step and the function generator sweeps the RF frequency down to 5 MHz to provide further RF evaporation. The plug beam shutter is opened during this time step. The plug beam should be focused at the center of the quadrupole

trap by the horizontal and vertical PZT control voltages set in the MOT loading stage. During this time step, the atoms are trapped in a plugged quadrupole trap which prevents Majorana losses and allows atoms to be successfully cooled.

26. **RF evaporation to 2.75 MHz:** In this time step, the RF switch is enabled and the RF frequency is swept from 5 MHz to 2.75 MHz in 3.114 s. This is the final stage of RF evaporative cooling.

A.4 Transfer to Hybrid Optical-Magnetic Trap and Optical Evaporation

27. **Transfer to ODT:** This is the first step in transferring atoms from a plugged quadrupole trap to the hybrid optical-magnetic trap. The 1064-nm trapping laser is vertically aligned 30 μm below the center of the plugged quadrupole trap. At the beginning of the time step, the RF switch to the 1064-nm AOM is switched on so that light will be coupled into the fiber and sent to the BEC cell (currently we are using the RF AOM switch as a shutter instead of a physical shutter). The computer control voltage that sets the output power of the 1064-nm laser through a feedback circuit is linearly ramped from 0 to 4.78 V, which corresponds to about 4.8 W in the trapping beam.

28. **Weaken quadrupole field:** This is the second step in transferring atoms to the combined optical-magnetic trap. In the first 500 ms, the quadrupole field is linearly ramped from 250 G/cm to 125 G/cm while the vertical PZT control voltage ramps the vertical position of the plug beam from 30 μm to 60 μm above the optical dipole trap center. In the next 500 ms, the plug vertical PZT voltage is ramped all the way to 0 V moving the plug so far above the dipole trap vertically that it no longer influences the atoms. At the same time, the vertical bias field is linearly ramped from 0.93 V to 2.3 V, which corresponds ramping the vertical center of the quadrupole trap from 30 μm to 180 μm above the optical dipole trap center.

29. **Optical Evaporation Stage 1:** During this step, the atoms are optically cooled by ramping down the laser power which decreases the height of the potential, allowing the hot atoms to escape the trap. In the first second of optical evaporation, the laser power is linearly ramped from 4.8 W to 1.9 W. In the following second, the laser power is then ramped down to 1.53 W. The first ramp occurs at a much faster rate than the second because more efficient

evaporation occurs at higher densities, or higher 1064-nm beam powers. During the transfer to the combined optical-magnetic trap, some atoms leave the position of the optical dipole trap and follow the movement of the center of the quadrupole field. In order to eliminate those atoms and prevent interactions with atoms trapped in the optical dipole trap, the RF switch is turned on at a frequency of 350 kHz. At such a small RF frequency, only atoms close to the center of the quadrupole field are eliminated.

30. **Split cloud:** During this time step, the plug vertical PZT voltage is ramped up to 4 V, moving the plug to a vertical position that provides a repulsive barrier to the atoms, splitting them into two clouds. At the beginning of the time step, the plug shutter is opened and the plug horizontal PZT voltage is snapped to around 1.7 V to provide the desired splitting ratio of the atoms into the two separate clouds.

31. **Move clouds away:** The horizontal PZT voltage is ramped up linearly from the splitting value in the previous time step to 5.95 V while the vertical PZT voltage is linearly ramped up from 4 to 6 V. These ramps move the right cloud from the center of the trap to 250 μm displaced horizontally. At the same time, the horizontal bias field is ramped up from 0 V to 1 V, 2.27 V or 4 V, moving the left cloud 150 μm, 350 μm or 590 μm, respectively, away from the initial position of the cloud. This results in a total separation between the two clouds of 400 μm, 600 μm and 840 μm respectively.

32. **Optical evaporation to BEC:** In this time step, optical evaporation continues to cool down the atom cloud until a significant amount of atoms have condensed. This step is broken up into four different ramps. In the first second, the laser power is ramped down to 1.17 W. During the following second, the laser is ramped down to a value between 0.9 and 1.1 W (the ending laser power for evaporation to BEC depends on how far away the BEC is displaced from the focus of the optical dipole trap). The laser power is then held constant for the next 250 ms which allows the atoms to rethermalize and is then ramped back up to 1.2 W in the last 250 ms.

    * For creating one cloud instead of two, disable steps 30-31.

33. **Heating ancillary thermal cloud:** This time step is usually disabled but can be enabled if the ancillary cloud starts to condense and a completely thermal cloud is desired for the experiment. During this step, the plug position is oscillated with a small amplitude which results in heating of the ancillary cloud without affecting the target cloud.

34. **660 ramp up:** Use this time step when disabling steps 30 and 31 if looking for vortices by colliding two BECs. The 660-nm laser current is controlled by the computer voltage and is ramped up and down in 250 ms, separating one BEC into two and colliding them back together. The 660-nm laser shutter is also pre–triggered to open at the beginning of the time step so that the light reaches the atoms as soon as the current is ramped up. This method is known to create vortices and has been used as a check to make sure the expansion procedure is such that vortices can be imaged in expansion.

35. **660 off:** This step pre-triggers the 660-nm laser shutter to turn off at the beginning of the time step and provides a hold time after the BECs have collided together.

36. **532 nm laser off:** During this time step, the plug vertical PZT control voltage is ramped down from 6 to 3 V in 2 ms. At 3 V, the vertical position of the plug is far enough above the atoms that it no longer influences them. As a result, the ancillary cloud is no longer constrained by the repulsive barrier and can move back towards the center of the trap.

37. **Ancillary cloud oscillation time:** During the first few ms of this hold time, the vertical PZT control voltage is ramped down to 0 V to ensure that the plug beam does not affect the atoms. During this hold time, the thermal cloud oscillates in the hybrid optical–magnetic trap and has a variable number of collisions with the BEC depending on the hold time. The plug shutter is also closed during this time step.

    * For doing the experiment, disable steps 34-35

A.6 Expansion

38. **Radial expansion:** This time step is used for expansion with Faraday imaging. During this step, the 1064-nm laser power is held constant at 1.2 W, preventing much vertical expansion. The quadrupole coils are ramped to 52 G/cm and the current in the Anti-Gravity coil is ramped to 0.85 A while the bias fields are ramped off. This results in much weaker radial trapping frequencies than before and some radial expansion. All bias fields are ramped off and the quadrupole and Anti-Gravity coil currents are ramped to the above values to avoid sloshing of the BEC expansion position.

39. **Vertical expansion:** The 1064-nm laser power is snapped off by disabling the RF AOM switch which allows for rapid vertical expansion as well as some radial expansion. The current through the quadrupole and Anti-gravity coils is the same as in step 38.

40. **Faraday in trap imaging:** For in trap Faraday imaging, all of the bias fields are snapped off and the 1064-nm laser power is snapped to 0 W. The quadrupole and anti-gravity coils are snapped to the values given in step 38. These coils provide a large enough bias field to image BECs with large signals at $+5\Gamma$ cooling imaging light detuning.

41. **Absorption imaging expansion:** All light and magnetic fields are turned off allowing the atoms to freely expand for the length of the time step. For *in situ* absorption images, use 0.05 ms as the expansion time.

A.7 Imaging

42. **AOMs on:** The amplitude control of the AOMs has a response time of about 40 μs. Therefore, the cooling and repump AOM amplitudes are turned on 50 μs before the imaging pulse to ensure that the output power is at the correct value throughout the entire pulse. During this time step, the repump and cooling AOM frequencies are also set to the correct values for the imaging pulse.

43. **Imaging pulse:** At the beginning of this time step, the cooling imaging and repump AOM switches are turned on and their shutters are pre–triggered to open, allowing both repump and imaging light to reach the atoms for the 75 μs imaging pulse. The repump light pumps all of the atoms into F = 2, allowing

atoms to be imaged with cooling light. The camera is triggered at the beginning of this step to capture the image.

44. **Hold between pulses:** There is a finite time that it takes the camera to read out the data from the previous image and be ready to take another image. For the flycapture camera this time is about 200 ms. However for the Princeton Instruments camera, the readout time is usually between 600 to 700 ms, depending on the Region of Interest size and amount of binning. To be safe, we hold for 750 ms in between imaging pulses so that all three images are triggered. This also allows all of the atoms to leave the location of the trap so that they are not imaged in the background frame.

47. **Hold between pulses:** Same as time step 44.

48. **Dark frame:** The camera is triggered here to take an image without any imaging light. This frame is subtracted from both the imaging and background frames to get rid of any ambient light present during the imaging pulses.

A.8 MOT Reset

49. **MOT reset:** All of the values are turned back to the MOT load values to begin to load the MOT again for the next run. The MOT coils are ramped back up to 7 A instead of being snapped up so that the TDK power supply does not trip during this time step.

50. **Push beam on:** The push beam is turned back on to allow loading of the 3D MOT from the 2D MOT.

APPENDIX B

Lab Trouble-shooting Guide

This appendix is designed as a trouble-shooting guide for the lab. Section B.1 is related to MOT trouble-shooting and Section B.2 describes how to trouble-shoot imaging, atom transfer, RF evaporation, and optical evaporation to BEC.

B.1 MOT Trouble-shooting

Follow these steps to debug issues related to low MOT number or no MOT at all.

1. Check MOT coil current. The current should be 7 A. The total output current is displayed on the front panel of the TDK power supply. During the MOT load time step, the only coils that have current running through them are the MOT coils, so the total current corresponds to the MOT current.

2. Measure the cooling and repump powers in 2D and 3D MOT splitters at 1900 mA drive current and compare to values in Table B.1. If the measured cooling powers are a couple of milliwatts different than the values given in the table, there probably will not be a huge difference in MOT number. However, if the measured cooling powers are 5 - 10 mW different than the values given in Table B.1, the fiber coupling into the 4- and 6-way splitters will need to be peaked up in order to create large MOTs.

3. Compare 2D MOT gradient and bias field currents to the values given in Table B.2.

Table B.1: MOT beam powers

	Repump Power (mW)	Cooling Power (mW)
2D fiber #4	3.7	63
3D fiber #5	2.2	28

Table B.2: 2D MOT gradient and bias field currents

	Voltage (V)	Current (A)
Horizontal 2D MOT Coil	6.1	1.79
Vertical 2D MOT Coil	5.7	1.78
2D Horizontal Bias Coil	1.2	0.71
2D Vertical Bias Coil	0.7	0.46

4. Measure the push beam power. With P_{push} = 600 μW and a detuning of $\Delta\nu$ = 0Γ, the MOT will load in about 2 s. However, if there is no power in the push beam under normal MOT load conditions, it is probably due to misalignment of the 60 MHz AOM that controls the frequency shifts of both the push beam and imaging beams. If this is the case, it is most likely that light into both push beam and imaging fibers is misaligned and will need to be realigned before imaging the atoms.

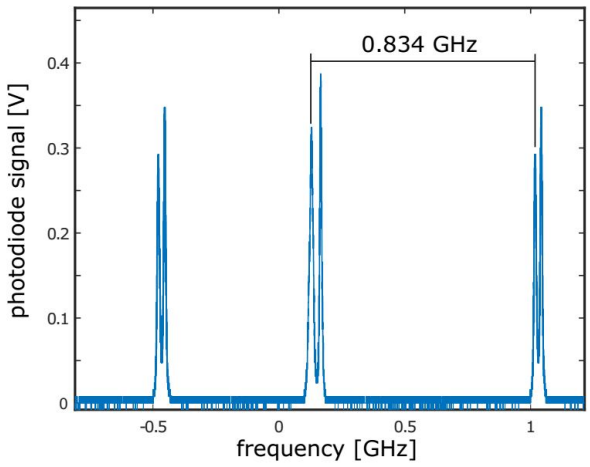

Figure B.1: Scanning Fabry-Perot (FP) cavity trace of the repump and cooling lines. The free spectral range of the FP cavity is 1.5 GHz. The ground-state splitting in ^{87}Rb is 6.834 GHz, so the repump and cooling lines are separated by 6.834 GHz modulo 1.5 = 0.834 GHz. The master and slave lasers show up as separate peaks due to slight differences in alignment into the FP cavity. Figure and caption taken from reference [17].

5. Check repump and cooling frequencies. Use the Fabry-Perot (FP) cavity trace to confirm that all repump and cooling lasers are single-mode and that the slave lasers are completely injection locked to their respective master lasers. Figure B.1 shows what the trace should look like when all lasers are single-mode, injection locked, and lasing at the correct frequencies. The repump and cooling lines are 6.843 GHz apart, due to the ground state splitting of ^{87}Rb. The free spectral range of the FP is 1.5 GHz. Therefore the spacing between the repump and cooling peaks seen on the FP trace should correspond to 6.834 GHz modulo 1.5 GHz, which is 0.834 GHz.

   Occasionally, problems with the lock boxes occur where the desired transition for locking is centered on the oscilloscope, but as soon as the loop gain is enabled, the laser locks to an adjacent transition. To test if this problem occurs, use the following procedure:

   - Center the desired locking signal on the oscilloscope
   - Turn the ramp gain all the way down
   - Change the PZT offset until the line is centered vertically at 0 V

   If the MOT starts to load when both lasers are unlocked but manually set to the correct frequency, the problem is with the lock box. Usually this occurs if the PZT is set to the opposite polarity needed to lock to the slope of the locking signal.

B.2 Trouble-shooting for No Atoms Imaged at the End of the Evaporation Sequence

In order to find out why atoms are not imaged at the end of the evaporation, it must be determined if the problem is due to imaging or a loss mechanism during atom transfer or evaporative cooling. If it is determined that the problem is not due to imaging, checks must be made throughout the evaporation sequence to determine where the problem arises.

B.2.1 Imaging Trouble-shooting

Check imaging parameters using the following procedure:

1. Measure background light level in second image taken to make sure that imaging light is on during the imaging pulse. For the horizontal imaging system with absorption imaging, a typical background image has between 60 to 120 counts

depending on the power during the imaging pulse. For the vertical imaging system with Faraday imaging, a typical background image has between 7 and 26 counts.

2. Open the repump imaging shutter and measure the repump power. The repump imaging power into the fiber should be about 4 mW and the repump power out of the imaging fiber should be about 600 μW. If the correct repump imaging power is measured before the fiber but not after the fiber, peak up the fiber coupling. If the fiber coupling seems to be optimized but the output power is still low, close the shutter and look at the fiber under the fiber scope. If the fiber core is dirty, clean it and then measure the output power. Dirty fiber cores can cause low output powers.

3. Check the camera settings:

   Horizontal Imaging with the FlyCapture Camera:

   - Shutter time: 10 ms
   - Gain: 2 dB
   - Imaging pulse length: 75 μs
   - Trigger Polarity: High
   - Trigger: Enabled

   Vertical imaging with the Princeton Instruments Camera:

   - Quality: Low Noise
   - Speed: 1 MHz
   - Analog Gain: Low
   - Mode: Frame Transfer
   - Storage shift rate: 1.2 μs
   - Trigger response: Readout per Trigger
   - Trigger determined by: Rising Edge
   - Exposure time: 75 μs
   - Frames to save: 3

4. Check cooling imaging light detuning during the imaging pulse. For diagnostic imaging from the side, use on resonance light by setting the imaging light AOM frequency voltage to 0.505 V. For Faraday imaging, usually +5Γ detuning is used by setting the imaging light AOM frequency voltage to 1 V.

Table B.3: Faraday Imaging B-field currents

	$V_{computer}$ (V)	Current (mA)
Quadrupole Coils	1.54	69
Anti-Gravity Coil	1.85	88

5. Check the magnetic field coil currents during the imaging pulse. During absorption imaging, all magnetic fields, including gradients and bias fields, should be turned off during the imaging pulse. Having stray magnetic fields on during absorption imaging results in imaging light that is no longer on resonance with the atoms. In these images, the atom cloud appears to be much less dense when compared to on resonance images with all magnetic fields off during the imaging pulse. For Faraday imaging, the bias fields should be turned off and the quadrupole coils and anti-gravity coil currents should be snapped the values given in Table B.3 immediately before the imaging pulse.

B.2.2 Atom Transfer Trouble-shooting

Use the horizontal imaging system to image atoms immediately after transfer from the 3D MOT chamber to the BEC cell in order to rule out problems with the transfer sequence. When the atoms are initially transferred to the BEC cell, the image of the cloud will fill the entire camera sensor. This results in an absorption image that is almost completely black because most of the imaging light is absorbed by the atom cloud. If atoms are not detected immediately after transfer, there is most likely a problem with the current in the transfer coils. Use the following procedure to determine the specific problem related to atom transfer:

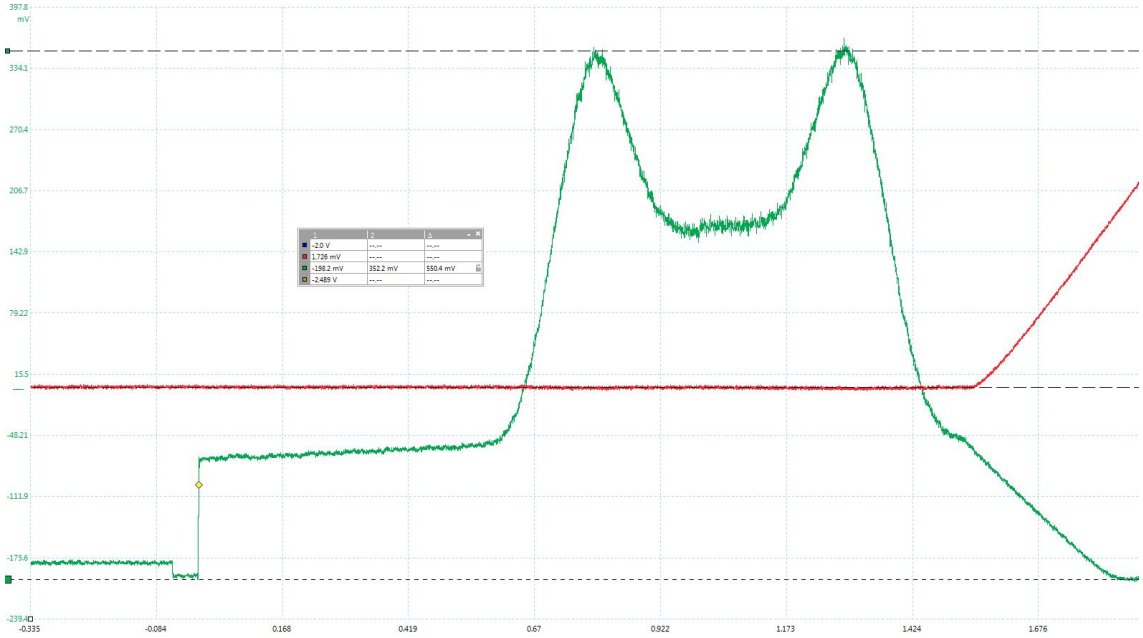

Figure B.2: Trace of the voltage drop across the 15Ω resistor due to output current of a CLSM-200LA current sensor which is proportional to total current through transfer coils. The trace shows the normal noise level on the current during transfer. The peak voltage shown in this trace is 550 mV, which corresponds to 73 A measured by the curent sensor and is about one-third of the peak total transfer current.

1. A CLSM-200LA closed loop Hall effect current sensor is used to measure roughly one third of the total output current from the TDK power supply. (There are three 3 AWG cables that connect the positive terminal of the TDK power supply to the source terminal on all of the MOSFETs. The current sensor only measures current through one of the cables, which should be about one-third of the total output current.) The current sensor outputs a current that is 1/2000 of the measured current. The picoscope shows the voltage drop across a precision 15 Ω resistor from this proportional current. This trace is proportional to the total current during transfer and should be monitored each run. Use Figure B.2 as a diagnostic to compare with transfer currents measured each day.

2. Compare the transfer current noise level measured with current sensor to the noise level in Figure B.2. The diagnostic trace in Figure B.2 shows a normal amount of noise on the transfer coils which does not result in any significant amount of atom loss. In the past, we have had problems with large noise levels on the transfer

coils currents which resulted in poor transfer efficiency. An example of this can be seen in Figure B.3.

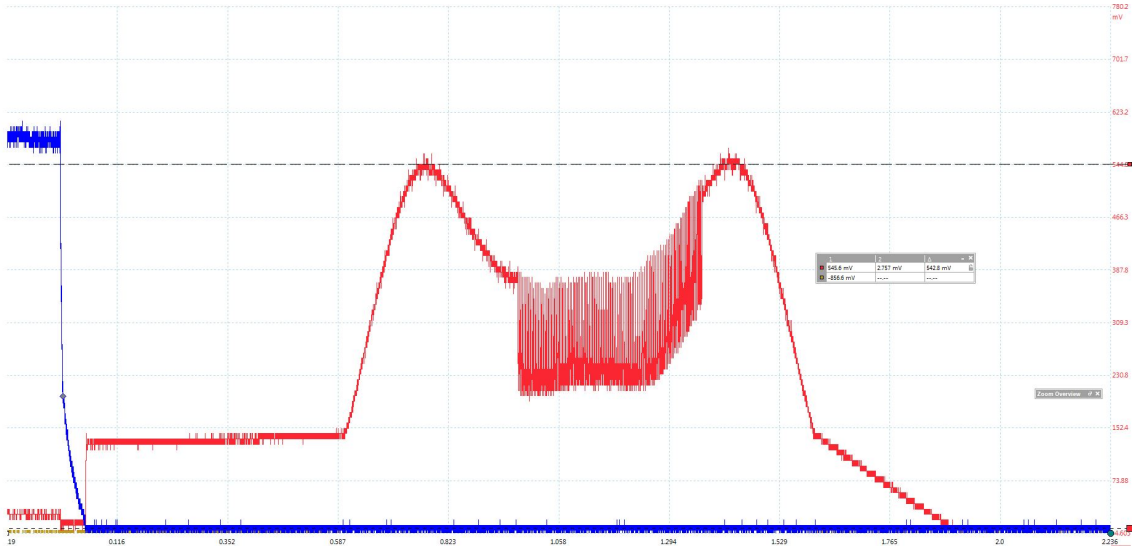

Figure B.3: Trace of noisy transfer signal resulting in significant amount of atom loss during transfer.

3. Compare the maximum voltage value in the transfer current trace to 550 mV, which is the maximum voltage value measured in the diagnostic trace shown in Figure B.2. 550 mV corresponds to an output current of $550\text{mV}/15\Omega = 37\text{mA}$. Therefore the current measured by the current sensor is $0.037\text{A} * 2000 = 74\text{A}$ and the maximum total current during transfer is about 200 A. (If the current measured through the current sensor was actually one-third of the total current, we would calculate the maximum total current to be 222 A, which is greater than the maximum current limit of 200 mA set on the TDK power supply. Therefore, there is some discrepancy between the measured value and known maximum current value. However, 550 mV can still be used as a maximum current diagnostic.) If the maximum voltage shown in the transfer coil trace is much less than 550 mV, which corresponds to a total transfer current of much less than 200 A, the magnetic field gradient will be too small and atoms will be lost during transfer. Usually the cause of lower total transfer currents is a failed MOSFET. When MOSFETs fail in BEC Lab #2, they still output some current but much less than the nominal value at a given gate voltage. In order to determine which MOSFET has failed, use the clamp hall probe to measure the current during transfer through

MOSFETs 3a, 3b, 4a, 4b, 5a, and 5b. The current should be identical in each MOSFET that corresponds to the same coil. When one MOSFET fails, much less current will be measured through it than its pair that corresponds to the same transfer coil.

To replace a failed MOSFET:

- Turn off the TDK power supply, the current sensors' power supply, and the feedback/interlock power supply.
- Take out the failed MOSFET. Make sure the wire that connects to the gate on the MOSFET does not fall underneath the aluminum plate heat sink while taking out the failed MOSFET.
- Put a small layer of thermal paste on the bottom of the new MOSFET. Screw the new MOSFET into the aluminum heat sink and make connections according the diagram on the inside of the MOSFET box lid.

After replacing the failed MOSFET, the hall probe should measure a maximum voltage of 550 mV corresponding to a maximum total transfer current of 200 A.

4. If the shape, amplitude, and noise level of the total transfer current measured by the current sensor matches with Figure B.2, atoms are most likely being transferred from the MOT cell to the BEC cell. At the end of the transfer section of the timing sequence, the transfer coils are linearly ramped down to 0 A, while the BEC quadrupole coils are ramped up to about 3.2 A which corresponds to a gradient of 250 G/cm. If atoms are transferred to the BEC cell but are not imaged, it is possible that the atoms are not being trapped in the BEC quadrupole coils and leave the trapping region before the imaging pulse. Use the clamp hall probe to measure the current through the BEC quadrupole coils at the end of the transfer steps. If current does not ramp up to 3.2 A in the coils, do the following checks to identify the problem:

   - Check to make sure that the Agilent power supply is turned on and that the output is enabled and set to 15 V.
   - Check connections between the Agilent power supply, the quadrupole coils, and the feedback circuit. The cable labeled Quad "−" is connected to the feedback circuit and should be connected to the BEC quadrupole coils through port #2 on the West side of the cell. Quad "+" is connected to the output of the Agilent power supply and should be connected to the BEC quadrupole coils through port #4 on the West side of the cell. If coils are

intact and connections are made correctly, 15 V can be measured at the connection between the power supply and the quadrupole coils and between the quadrupole coils and the feedback circuit at ports 4 and 2 respectively.

B.2.3 Trouble-shooting of RF evaporation in Plugged Quadrupole Trap

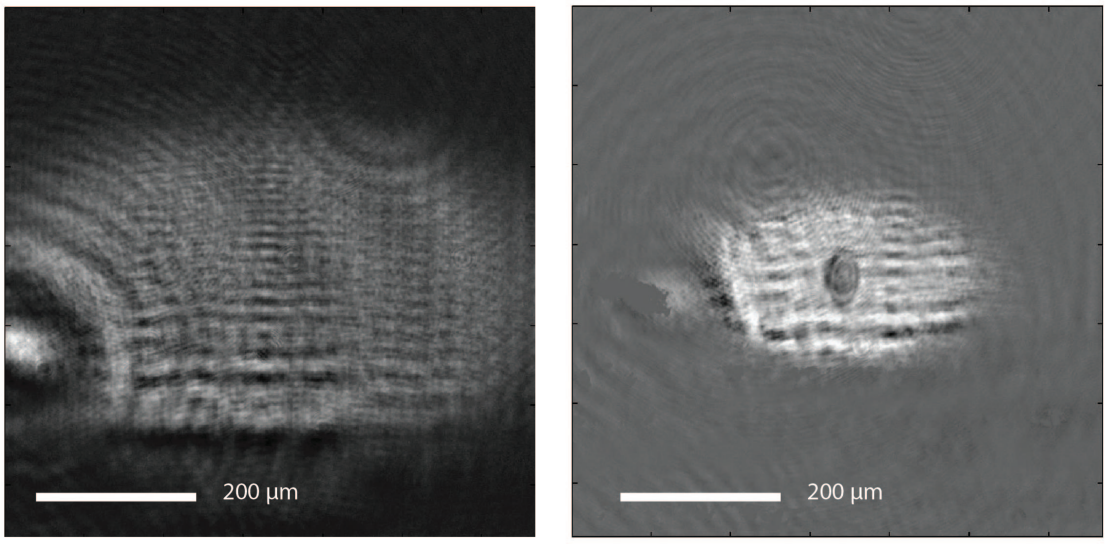

Figure B.4: *In situ* absorption image of atoms in the plugged quadrupole trap after RF evaporation down to **left:** 5 MHz and **right:** 2.75 MHz. The absorption image has been subtracted from the background image so that atoms are seen as a bright spot.

Use the horizontal imaging system to image atoms in the plugged quadrupole trap after RF evaporation down to 5 MHz and 2.75 MHz. Figure B.4 shows what the cloud should look like with absorption imaging from the side at these point in the evaporation sequence. The full width half maximum of the 2D guassian fit to the image taken after RF evaporation down to 5 MHz are $\text{FWHM}_x \sim 640$ μm and $\text{FWHM}_y \sim 250$ μm. After RF evpaoration down to 2.75 MHz, the measured widths are $\text{FWHM}_x \sim 300$ μm and $\text{FWHM}_y \sim 170$ μm. The OD calculated from the fit from the right image 1.6. If everything is working up to that point in the timing sequence, the measured widths of any image taken at this same point in the evaporation sequence should be within 10–15% of the values given above. Use

Figure B.4 and the above values as a diagnostic of RF evaporation in the plugged quadrupole trap.

1. The 532-nm beam is focused close to the center of the quadrupole trap when aligned well and is used as a repulsive barrier to keep atoms from being lost due to spin flips. As seen in Figure B.4, a well aligned plug beam results in a hole at the center of the plugge quadrupole trap. If no clear hole is seen in middle of the atom cloud, the problem is most likely with the plug beam power, alignment or timing of the external shutter. In order to find out the specific problem with the plug beam, use the following procedure:

    - Make sure that the 532-nm laser is on, the internal laser shutter is open, and that the laser outputs 6.5 W when the external shutter is open.
    - Check that external shutter opens during the experiment. When the shutter is open, you will see green scattered light above the experiment.
    - In the past, we have had problems seeing the hole in the atom cloud from the plug due to incorrect timing in turning off the external plug beam shutter. The external shutter was incorrectly pre–triggered to turn off a couple of ms before the imaging pulse instead of immediately before the imaging pulse. This resulted in atoms filling in the "hole" before the image was taken. To check if shutter triggering timing is the cause of the problem, keep the 532-nm laser on during the imaging pulse instead of pre–triggering it to turn on immediately before. If the hole is seen then seen in the image, simply re-measure the turn off time of the external shutter and update the pulse time in the timing sequence to the measured value.
    - Check the alignment of the 532-nm laser. Open the external shutter and look on the Thorlabs alignment camera in real time. During the MOT loading stage, the PZT voltage for the horizontal and vertical control of the 532-nm laser is around $(V_x, V_y) = (1.2V, 4V)$. When aligned, this corresponds to a beam centered at pixels (361,465) on the Thorlabs alignment camera. If the alignment is so bad that the beam is barely seen on the camera, use the horizontal and vertical knobs on the last mirror (not the dichroic mirror) in the 532-nm beam path before the cell. When the alignment is close, simply make slight changes to the voltage sent to the horizontal and vertical PZT controls until the beam is once again centered at (361, 465).

2. If the measured size of atomic cloud after RF evporation down to 2.75 MHz is much larger than $\text{FWHM}_x \sim 300$ μm and $\text{FWHM}_y \sim 170$ μm:

Figure B.5: Picoscope trace of the total transfer coil current (green), the measured current through the BEC quadrupole coils (red) and the photodiode signal proportional to the 1064-nm laser power (yellow) without RF on during the run.

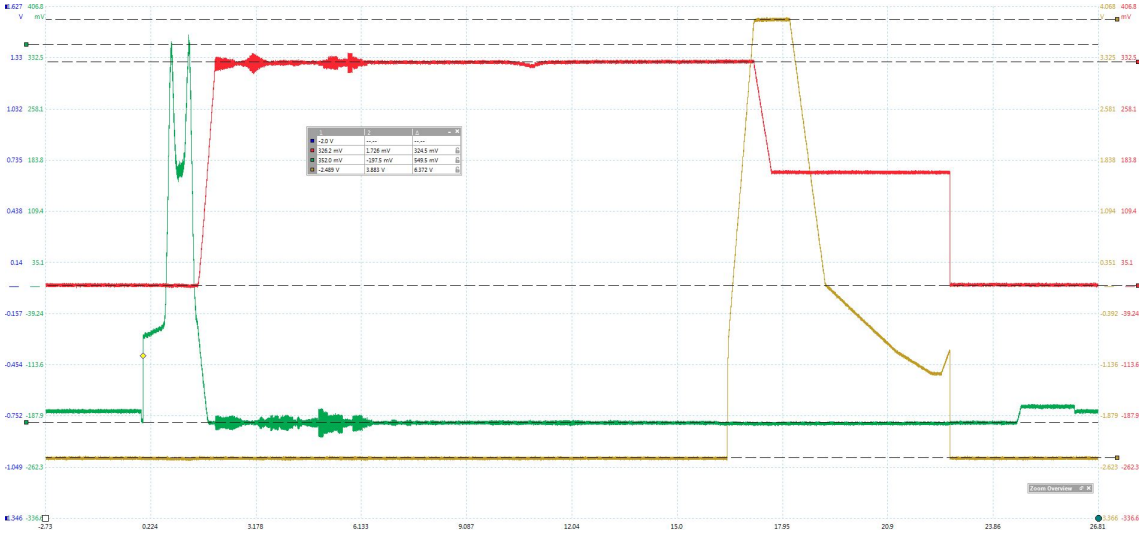

Figure B.6: Picoscope trace of the total transfer coil current (green), the measured current through the BEC quadrupole coils (red) and the photodiode signal proportional to the 1064-nm laser power (yellow) with RF on during the run. This Figure shows a normal amount of RF pickup on the BEC quadrupole coils.

- Check the expansion time. Figure B.4 is an *in situ* image of the atom cloud. The dark background time step should be set to 0.05 ms for *in situ* images. (If this time step is set to a couple of ms instead of 0.05 ms, the atoms will expand a considerable amount and it will seem like there is a problem with the RF evaporation.)
- Check RF pickup on the transfer coils to make sure the RF synthesizer and amplifier are working correctly. Figure B.6 gives a reference for RF pickup on the BEC quadrupole coils during normal operation. Figure B.5 shows what the quadrupole current looks like without any RF pickup. This occurs when the RF switch after the RF amplifier is turned off which results in no amplified RF sweeps. If no RF pickup is seen on the quadrupole coils as in Figure B.5, check to make sure that RF amplifier is turned on, the display indicates "RF on" and "ARMED" on the front panel, and that the RF amplifier power supply is turned on. If there is still no pickup on the quadrupole coils, measure the conductivity of the RF coil. If RF coil is intact, measure output from the RF generator with the high frequency oscilloscope. Note that the Ophir 5303055 Solid State RF Amplifier has a small signal gain of +43dB. Make sure to use enough RF attenuators on the input to the oscilloscope so that the amplified RF signal is at a safe level to input to the oscilloscope. When the RF is working, a sine wave with changing frequency will be seen on the oscilloscope. The frequencies and amplitudes of the sine wave can be compared to the computer programmed values during the sweep.

3. If the atom cloud is about the same size but with an OD much less than 1.6:

   - Relock lasers and make sure this is not an imaging issue.
   - Measure current through the BEC quadrupole coils with the clamp hall probe and compare the amount of RF pickup measured the amount shown in Figure B.6. Too much RF pickup on the quadrupole coils results in unstable quadrupole current and consequently significant atom loss during RF evaporation. Figure B.7 gives an example of RF pickup on quadrupole coils which results in a significant amount of atom loss. We have found that the best way to get rid of excessive RF pickup is to decrease the RF amplitude during the evaporation sequence for specific frequency ranges in which RF pickup causes dips in the quadrupole current.

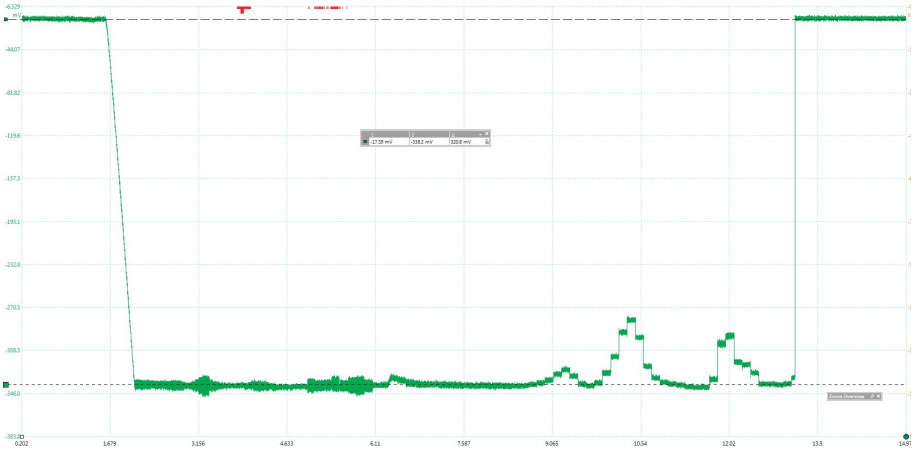

Figure B.7: Picoscope trace of current in the BEC quadrupole coils during RF evaportion measured by the clamp hall probe. The voltage in the trace is negative because the hall probe was oriented in the opposite direction of current flow. The dips in the current are due to too much RF pickup on the quadrupole coils.

B.2.4 Trouble-shooting Optical Evaporation to BEC

Use the horizontal imaging system to image the atom cloud after transferring atoms to the hybrid optical-magnetic trap and after optically evaporating for 2 s. Figure B.8 shows images of the atom cloud at both stages under normal operation.

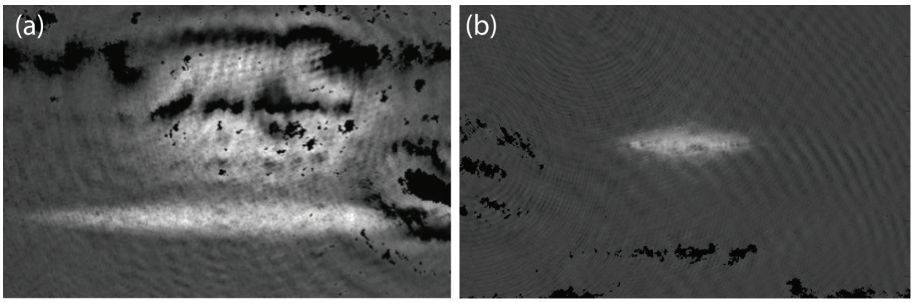

Figure B.8: 670 μm $\times$ 350 μm side view images taken with the horizontal imaging system of atoms in the hybrid trap at different stages of the evaporation sequence. (a) Image of atoms immediately after transfer to hybrid trap. (b) Image of atoms after first two seconds of optical evaporation.

1. If no atoms are imaged at this stage, check that 1064-nm laser is ramping up

to correct value by comparing the yellow photodiode signal on the picoscope in Figure B.6.

- Make sure lock box used for the feedback circuit is powered, the laser power is set to 100% and that the digital enable for 1064-nm laser AOM is on during transfer to the hybrid trap and during optical evaporation. If the digital enable is turned off at some point during transfer and optical evaporation, all the atoms will be lost.
- As the laser power is ramped up up to the maximum power of about 4.8 W to transfer atoms from the plugged quadrupole trap to the hybrid optical–magnetic trap, the corresponding photodiode signal on the picoscope should measure 6.37 V. If the maximum photodiode signal is less than 6.37 V, the fiber coupling efficiency might need to be peaked up to get the maximum power out of the fiber.

2. If the laser is ramping up to the correct power but no atoms are imaged, check 1064-nm laser alignment. There is a flip mirror in between the last mirror in the 1064-nm beam path and the BEC cell. Flip the mirror down and switch the USB connection to the 1064-nm alignment Flycapture camera. Figure B.9 shows what the beam should look like when aligned. The measured beam radii are $\omega_{0z} = 29.5\mu$m and $\omega_{0y} = 273\mu$m which gives an aspect ratio of 9.25:1. When the trapping laser is aligned, it should be centered at pixels (432, 426) on the alignment camera. If the image of the beam is far off on the camera, use horizontal and vertical knobs on the last mirror before the cell to center the focus 1064-nm beam on the correct spot on the camera.

3. If every image looks like it should so far, image the atom cloud at the end of the optical evaporation sequence. If there are still no atoms, increase the final 1064 power level at the end of the optical evaporation sequence by about 0.05 to 0.1 W.

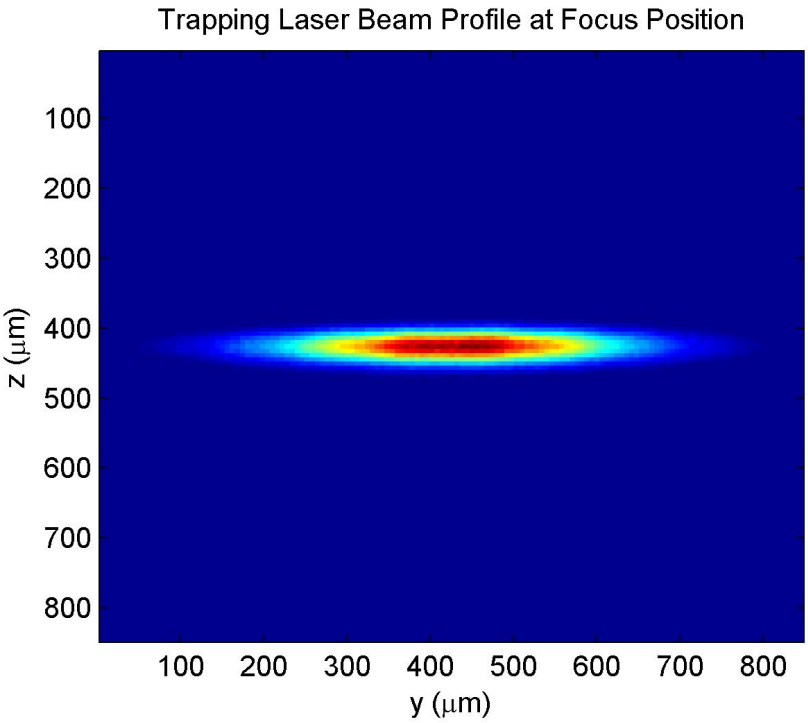

Figure B.9: Trapping laser beam profile at the focus position. The measured beam radii are: $\omega_{0z} = 29.5\mu$m and $\omega_{0y} = 273\mu$m.

REFERENCES

[1] M. Lesieur. *Turbulence in Fluids*. Kluwer Academic Publishers, second edition, 1990.

[2] A. N. Kolmogorov. The Local Structure of Turbulence in Incompressible Viscous Fluid for Very Large Reynolds' Numbers. *Akademiia Nauk SSSR Doklady*, 30:301–305, 1941.

[3] H. L. Grant, R. W. Stewart, and A. Moilliet. Turbulence Spectra from a Tidal Channel. *Journal of Fluid Mechanics*, 12(2):241–268, 1962.

[4] B. K. Martin, X. L. Wu, and W. I. Goldburg. Spectra of Decaying Turbulence in a Soap Film. *Physical Review Letters*, 80(18):3964–3967, 1998.

[5] C. E. Leith. Diffusion approximation for two-dimensional tubulence. *Physics of Fluids*, 11:671–673, 1968.

[6] J. Sommeria, S. D. Meyers, and H. L. Swinney. Laboratory simulation of Jupiter's Great Red Spot. *Nature*, 331:689–693, 1988.

[7] J. Miller, P. B. Weichman, and M. C. Cross. Statistical Mechanics, Euler's equation, and Jupiter's Red Spot. *Physical Review A*, 45(4):2328–2359, 1992.

[8] R. H. Kraichnan. Inertial Ranges in Two-Dimensional Turbulence. *Physics of Fluids*, 10(7):1417–1423, 1967.

[9] W. F. Vinen and J. J. Niemela. Quantum Turbulence. *Journal of Low Temperature Physics*, 128(516):167–231, 2002.

[10] R. P. Feynman. *Progress in Low Temperature Physics, Vol. 1.* North-Holland Publishing Company, Amsterdam, 1955.

[11] A. J. Allen, N. G. Parker, N. P. Proukakis, and C. F. Barenghi. Quantum turbulence in atomic Bose-Einstein condensates. *Journal of Physics: Conference Series*, 544(012023), 2014.

[12] K. E. Wilson, E. C. Samson, Z. L. Newman, T. W. Neely, and B. P. Anderson. *Annual Review of Cold Atoms and Molecules, Vol.1.* World Scientific Publishing, 2013.

[13] T. W. Neely, E. C. Samson, A. S. Bradley, M. J. Davis, and B. P. Anderson. Observation of vortex dipoles in an oblate Bose-Einstein condensate. *Physical Review Letters*, 104(16):0–5, 2010.

[14] L.D. Landau. *Fluid Mechanics*. Pergamon Press, Oxford, UK, 1987.

[15] W. F. Vinen. The Physics of Superfluid Helium. In S. Russenschuck and G. Vandoni, editors, *CAS - CERN Accelerator School on Superconductivity and Cryogenics for Accelerators and Detectors*, Geneva, 2002.

[16] W. Guo, M. La Mantia, D. P. Lathrop, and S. W. Van Sciver. Visualization of two-fluid flows of superfluid helium-4. *Proceedings of the National Academy of Sciences*, 111(Supplement 1):4653–4658, 2014.

[17] Z. L. Newman. *A New Apparatus for Studies of Quantized Vortex Dynamics in Dilute Gas Bose Einstein Condensates*. PhD thesis, University of Arizona, 2016.

[18] C. J. Pethick and H. Smith. *Bose-Einstein Condensation in Dilute Gases*. Cambridge University Press, Cambridge, second edition, 2008.

[19] W. D. Phillips, J. V. Prodan, and H. J. Metcalf. Laser cooling and electromagnetic trapping of neutral atoms. *Journal of the Optical Society of America B*, 2(11):1751–1767, 1985.

[20] P. D. Lett, R. N. Watts, C. I. Westbrook, W. D. Phillips, P. L. Gould, and H. J. Metcalf. Observation of atoms laser cooled below the doppler limit. *Physical Review Letters*, 61(2):169–172, 1988.

[21] T. W. Hänsch and A. L. Schawlow. Cooling of gases by laser radiation. *Optics Communications*, 13(1):68–69, 1975.

[22] C. Wieman and T. W. Hänsch. Doppler-free laser polarization spectroscopy. *Physical Review Letters*, 36(20):1170–1173, 1976.

[23] T. Petelski, M. Fattori, G. Lamporesi, J. Stuhler, and G.M. Tino. Doppler-free spectroscopy using magnetically induced dichroism of atomic vapor: a new scheme for laser frequency locking. *The European Physical Journal D*, 22(2):279–283, 2003.

[24] C. P. Pearman, C. S. Adams, S. G. Cox, P. F. Griffin, D. A. Smith, and I. G. Hughes. Polarization spectroscopy of a closed atomic transition: applications to laser frequency locking. *Journal of Physics B: Atomic, Molecular and Optical Physics*, 35(24):5141–5151, 2002.

[25] B. DeMarco. *Quantum Behavior of an Atomic Fermi Gas*. PhD thesis, University of Colorado, 2001.

[26] W. Petrich, M. H. Anderson, J. R. Ensher, and E. A. Cornell. Stable, Tightly Confining Magnetic Trap for Evaporative Cooling of Neutral Atoms. *Physical Review Letters*, 74(17):3352–3355, 1995.

[27] D. E. Pritchard. Cooling Neutral Atoms in a Magnetic Trap for Precision Spectroscopy. *Physical Review Letters*, 51(15):1336–1339, 1983.

[28] U. Ernst, A. Marte, and F. Schreck. Bose-Einstein condensation in a pure Ioffe-Pritchard field configuration. *Europhysics Letters*, 41(1):1–6, 1998.

[29] T. Esslinger, I. Bloch, and T. W. Hänsch. Bose-Einstein condensation in a quadrupole-Ioffe-configuration trap. *Physical Review A*, 58(4):2664–2667, 1998.

[30] K. B. Davis, M. Mewes, M. A. Joffe, M. R. Andrews, and W. Ketterle. Evaporative Cooling of Sodium Atoms. *Physical Review Letters*, 74(26):5202–5205, 1995.

[31] R. Grimm and M. Weidem. Optical dipole traps for neutral atoms. In Ennio Arimondo, Chun C. Lin, and Susanne F. Yelin, editors, *Advances In Atomic, Molecular, and Optical Physics*. Elsevier Inc., 1987.

[32] D. A. Steck. Rubidium 87 D Line Data, 2003.

[33] L. P. Maguire, S. Szilagyi, and R. E. Scholten. High performance laser shutter using a hard disk drive voice-coil actuator. *Review of Scientific Instruments*, 75(9):3077–3079, 2004.

[34] W. Ketterle, D. S. Durfee, and D. M. Stamper-Kurn. Making, probing and understanding Bose-Einstein condensates. In *Proceedings of the International School of Physics "Enrico Fermi" Vol. CXL*. IOS Press, 1999.

[35] K. E. Wilson. *Developing a Toolkit for Experimental Studies of Two-Dimensional Quantum Turbulence in Bose-Einstein Condensates*. PhD thesis, University of Arizona, 2015.

[36] J. Weiner, V. S. Bagnato, S. Zilio, and P. S. Julienne. Experiments and theory in cold and ultracold collisions. *Reviews of Modern Physics*, 71(1):1–85, 1999.

[37] W. Ketterle and N.J. Van Druten. Evaporative Cooling of Trapped Atoms. *Advances In Atomic, Molecular, and Optical Physics*, 37:181–236, 1996.

[38] N. R. Thomas, N. Kjærgaard, P. S. Julienne, and A. C. Wilson. Imaging of s and d Partial-Wave Interference in Quantum Scattering of Identical Bosonic Atoms. *Physical Review Letters*, 93(17):173201–1 – 173201–4, 2004.

[39] K. M. R. Van Der Stam, R. Meppelink, J. M. Vogels, and P. Van Der Straten. Reaching the hydrodynamic regime in a Bose-Einstein condensate by suppression of avalanches. *Physical Review A*, 75(3):1–4, 2007.